Title
Mixed-linker Approach toward the Structural Design of Metal-Organic Frameworks

Author
Yang, Jingjing

Publication Date
2018

Peer reviewed|Thesis/dissertation

Mixed-linker Approach toward the Structural Design of Metal-Organic Frameworks

By

Jingjing Yang

A dissertation submitted in partial satisfaction of the

requirements for the degree of

Doctor of Philosophy

in

Chemistry

in the

Graduate Division

of the

University of California, Berkeley

Committee in charge:

Professor Omar M. Yaghi, Chair
Professor Jeffrey R. Long
Professor Kenneth N. Raymond
Professor Jeffrey A. Reimer

Spring 2018

Abstract

Mixed-linker Approach toward the Structural Design of Metal-Organic Frameworks

by

Jingjing Yang

Doctor of Philosophy in Chemistry

University of California, Berkeley

Professor Omar M. Yaghi, Chair

Metal-organic frameworks (MOFs) are porous, crystalline, extended structures made by linking inorganic and organic molecular building blocks together through strong coordination bonds. Due to their high surface areas, pore volumes, and the possibility of decorating them with a great variety of chemical functionalities through the judicious choice and design of their inorganic joints and organic struts, MOFs have been studied extensively and found useful in widespread industrial applications, such as gas storage, separation, and catalysis.

The design and synthesis of new MOFs with desirable properties and functions is a central theme in MOF chemistry. Generally, the structural design of MOFs is realized by a reticular synthesis approach, whereby the metal-based nodes and rigid organic linkers have predetermined geometries. However, when it comes to MOFs with flexible coordination geometries, it can become challenging to successfully guide the synthesis.

The work herein describes my Ph.D. research, dealing with the structural design of two important subclasses of MOFs, zeolitic imidazolate frameworks (ZIFs) and calcium-based environmentally friendly MOFs. Due to the structural unpredictability arising from the flexible coordinative behavior of the metal centers and organic linkers, the development of both classes of materials has so far relied heavily on synthetic “trial and error”, which has greatly limited their structural diversities. The work presented here shows that such challenges can be addressed by the synergistic assembly of linkers with different functionalities (mixed-linker approach). Following this strategy, fifteen new porous ZIF structures (amongst which structures presenting the largest cage and aperture reported for ZIFs), and two new porous calcium lactate frameworks were created. Furthermore, this work allowed the identification and establishment of three general principles for the guided structural design of ZIFs.

Chapter 1 introduces the concept, synthesis, characterization, and classification of MOFs. Then the importance and existing approaches for structural design are summarized. Finaly, the structure-function relationship is discussed to address the potentials of MOF materials in practical industrial applications.

Chapter 2 reports the synthesis and characterization of a series of ZIFs with ultra-large pores and aperture sizes via the mixed-linker approach. The synthesis of fifteen new ZIFs (ZIF-303, -360, -365, -376, -386, -408, -410, -486, -412, -413, -414, -516, -586, -615, and -725) is presented. Members of this list represent ZIFs with the largest pore sizes and

aperture sizes (ZIF-412 and ZIF-516, -586, -615, -725) reported so far. Morevoer, a tertiary combination of linkers with different functionalities is reported for the first time in these new structures.

Chapter 3 builds upon the work of Chapter 3 and addresses the desire to uncover general synthetic principles to guide the synthesis of ZIFs. It begins with the analysis of relationship between the imidazolate starting material and framework structure based on the fifteen new ZIFs presented in Chapter 2. The ring in the ZIF structure is identified as the bridge, and the mixed imidazolate approach is the key to tune the ring size and composition. Based on these analyses, three general principles are identified which are applicable to the whole class of ZIF materials.

Chapter 4 switches focus from the previous chapters, and explores the use of a mixed-linker approach in another subfield of MOFs: calcium-based MOFs. The successful implementation of the mixed-linker approach in the ZIF synthesis encouraged us to explore similar synthetic challenges in other fields. In this chapter, the environmentally-friendly calcium-based MOFs are selected as topic of investigation. Using a combination of naturally existing lactate and acetate linkers, the first two examples of porous of calcium lactate frameworks are synthesized and presented. I demonstrate that both of these linkers are essential to the successful formation of the final structure.

Chapter 5 presents potential applications of the newly-made MOFs described in the previous chapters. A particular attention is paid to environmental applications benefiting from the structural and componential characters of the MOFs. The hydrophobic large-pore ZIF is demonstrated to be highly efficient for air purification through the removal of volatile organic compounds, and the calcium-based MOF, exhibiting an environmentally-friendly composition, is shown to be an effective pesticide carrier for agriculture purposes.

Chapter 6 is the final chapter of my thesis, in which I provide my humble thoughts and perspectives of the future development of the structural design of MOFs. MOFs are highly potential in real world applications, and the rational design of their structures and compositions, in order to meet the requirements for targeted applications, is the key to success.

To my parents Dengjun and Qingxia, my wife Yukai, and my parents-in-law, thank you for believing in and supporting me.

Table of Contents

List of Figures

Chapter 1

Chapter 2

Chapter 3

Chapter 4

Chapter 5

List of Tables

Chapter 2

Chapter 3

Chapter 4

Acknowledgements

I would have never completed this five-year's work without the firm support from my family, teachers, colleagues, and friends who cared and helped me. To all of you, I want to say thank you. Your patience, supports, encouragements, and advices are all priceless treasures to make who I am today. My gratitude is more than what can be expressed by words.

Thank you Mom and Dad for bringing me to this world, and thank you my wife Yukai Huang for accompanying me. I would also like to thank my parents-in-law and Yuhui, my sister-in-law. You love me and always give me the best; you respect me and always allow me to pursue my interest. I am really grateful to you, and I shall say my happy engagement with chemistry is the outcome of your kindness. I feel so lucky that I have you.

Thank you all my teachers (Houman Zhou, Jiazhu Wang, Genzhu Li, Yinglin Li, Jeffrey R. Long, Kenneth N. Raymond, and many many of you). You spent much time on me teaching me knowledge without asking for return. Thank you my tutors Prof. Shuhong Yu and Prof. Omar M. Yaghi, you introduced me to research and allowed me to explore freely. You are real scientists with inspiration and enthusiasm. You mentored me and made me falling in love with research. Special thanks for your faith in my abilities. I would also like to extend my appreciation to my committee members (Prof. Jeffrey R. Long, Prof. Kenneth N. Raymond, Prof. Jeffrey A. Reimer, and Prof. Felix Fisher), thank you for providing me suggestions and the knowledge to be a qualified researcher. All of you were very patient with me even though I am not smart (Special thanks to my respectable professor Omar M. Yaghi), and it is your encouragements and kindness allowing me to make progresses slowly but steadily.

Thank you all my colleagues and collaborators. It is really my great pleasure to work with you and thank you for making research shining. Without you, it would be very hard and boring (Prof. Peidong Yang, Prof. Yuebiao Zhang, Prof. Hexiang Deng, Prof. Osamu Tereasaki, Prof. Michael O'Keeffe, Prof. Hans-Beat Bürgi, Prof. Enrique G. Puebla, Prof. Angeles M. Bravo, Dr. Hiroyasu Furukawa, Dr. Simon, J. Teat, Dr. Kevin, J. Gagnon, Dr. Juncong Jiang, Dr. Ping Chen, Tianyuan Xiao, Dr. Qi Liu, Dr. Christopher Trickett, Dr. Mathieu Prevot, Dr. Chenfei Zhao, Dr. Yong Liu, Chritian Diercks, Robinson Flaig, Eugene Kapustin, Yuzhong Liu, Hao Lyu, Xiaokun Pei, Haoze Wang, Wentao Xu, Dr. Zheng Liu, Chenlu Xie, and many many more). Your strong expertise and insights benefitted and inspired me a lot. Special thanks to Dr. Mathieu Prevot, Christian Diercks, Yuzhong Liu, Robinson Flaig for their helps to improve the language of this thesis. Some of you are famous professors who have been working on fantastic research for many years, some of you have started your indepedant academic career, some of you work in companies, and some of you are on the way to these just like me. Though we are at different stages, we are bonded together to share knowledge and funny life moments. We are, and will continue to be the best colleagues. I hope you all enjoy your lives, and I am looking forward to having more chances to collaborate with you in the future.

Thank you all my friends. Without you, my life would be lonely (Yude Su, Dandan Zhang, Zeming Wang, Jianwei Xiao, Zhongyuan Lu, Huayong Zhi, Xiang Gao, Kyle Cordova, Dr. Mathieu Prevot, Dr. Chenfei Zhao, Chritian Diercks, Robinson Flaig, Philjun Kang, Seungkyu Lee, Bunyarat Rungtaweevoranit, Yingbo Zhao, Fan Cui, Qizhi Xu, Wenchi Liu, Rapeepat Sangsuwan, and many many more). I must say that going out with you, having food with you, playing games with you, and chatting with you really made my life fun. Special thanks to those of you who I met in U.S. for teaching me to look beyond the

laboratory and enjoy lives in the Bay Area. Most of you have graduated and started your new jobs, but we were, are, and will still be best friends. Keep in touch my friends, and I am looking forward to see you again.

I would also like to acknowledge my graduate research group. The lovely Yaghilab is a group fulfilled with brilliant minds and crazy ideas. All of you had a substantial impact on my development by providing me suggestions on research, and maintaining a friendly lab environment. I am also grateful to Salman Alahmadi, an undergraduate researcher who worked for me, for his diligence and dedication.

I would never be a chemist without these amazing people around me. There are a lot of failures depressing me both in and out of the laboratories. But it is because of you who made me thinking positively and finally turning those failures into the cornerstones to success. You are the people who I will treasure throughout my life.

Chapter 1: Structural Design in Metal-Organic Frameworks

1.1 Introduction to Metal-Organic Frameworks

Metal-Organic Frameworks (MOFs) are porous, crystalline, extended structures made by linking inorganic and organic molecular building blocks together through strong bonds.[1] These inorganic building blocks are metal clusters, while the organic building blocks are mono or polytopic organic ligands exhibiting coordinative groups such as carboxylate, catecholate, imidazolate, and pyrazolate groups. Compared to traditional porous materials such as zeolites, mesoporous silicas or carbons, MOFs possess extremely high surface areas (1000 to 10,000 m^2/g), large void spaces (typically greater than 50% of the MOF crystal volume), and a variety of chemical functionalities that can be achieved via the judicious design of inorganic joints and organic struts. MOFs have been studied extensively and found useful in widespread industrial applications, such as gas storage, separation, and catalysis.[2]

One famous example of MOFs is MOF-5, a three-dimensionally extended framework built by linking six-connected inorganic Zn_4O clusters (joints) with ditopic terephthalate linkers (struts) (Figure 1.1).[3] The directionality of the inorganic metal clusters and the organic linkers support a network with high structural rigidity, leaving large empty spaces between the joints and struts, which are occupied by solvent molecules during the synthesis. This high structural rigidity allows the subsequent removal of guest molecules in the pores under vacuum or heat without triggering the collapse of the framework, resulting in high permanent porosity.

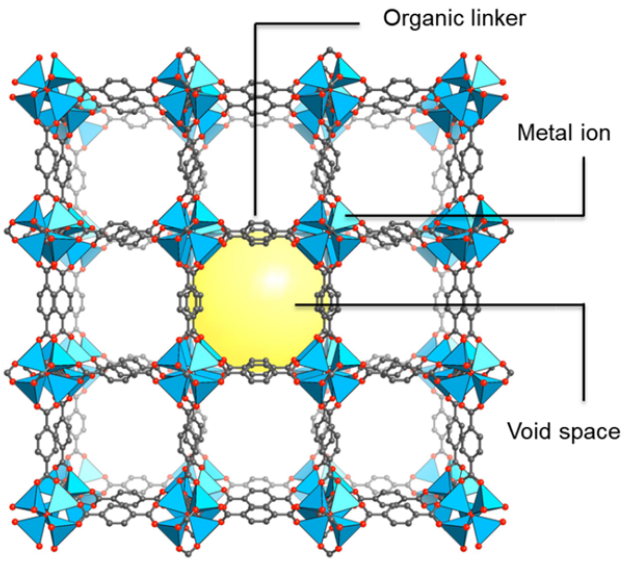

Figure 1.1 Structure of MOF-5, with red, and gray spheres representing O, and C atoms, respectively. Zn_4O clusters are shown in blue tetrahedra. Pores are illustrated as yellow sphere.

A typical synthesis of MOF begins with the mixing of a metal salt (*e.g.* zinc nitrate) and an organic linker (*e.g.* terephthalic acid) in a solvent (*e.g. N*,*N*-dimethylformamide).The solution (or mixture) is then sealed in a glass vial or an autoclave and heated at a specific temperature for a desired period of time. Upon the reaction, the organic linker is gradually deprotonated, and co-assembles with the metal ion to form the structure through coordination

bonds.

MOF crystals with sizes ranging from nanometer to millimeter regimes can then be harvested at the end of the synthetic process, and their structure is subsequently characterized by diffraction techniques (X-ray crystallography, neutron and electron diffraction, *etc.*).

The as-synthesized MOF crystals still contains solvent molecules inside its pores, which need to be removed to achieve permanent porosity. This is typically done by exchanging the solvent from the synthesis with a low boiling point solvent (acetone, methanol, chloroform, *etc.*), which can then easily be removed under dynamic vacuum or heat. The resulting activated MOFs are 'porous' with a large portion of empty pore space.

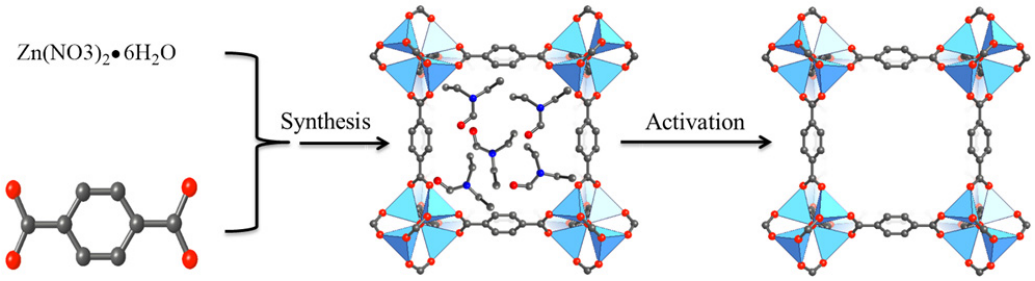

Figure 1.2 Schematic illustration of the synthesis and activation of MOF-5, red, blue, and gray spheres representing O, N, and C atoms, respectively. Zn_4O clusters are shown in blue tetrahedra. The solvent trapped in the pores is *N*,*N*-diethylformamide.

Isothermal gas adsorption measurement (*e.g.* N_2 adsorption at 77 K) is used to probe the pore structure: pore volume, surface area, and pore size distribution. The bulk material can be examined by thermogravimetric analysis or variable temperature powder X-ray diffraction to determine its the thermal stability; by solvent and acid/base test to reveal its chemical stability; by elemental analysis and ^{1}H digest NMR to identify its chemical composition; by infrared spectroscopy and solid state NMR to gain information on the nature of the chemical bonds information, by powder X-ray diffraction to confirm phase purity, *etc.*

There are currently more than 20,000 reported MOFs.They can be classified based on the metal ions (main group IA-IIIA metal ions; transition metal ions, lanthanide and actinides), or the coordinative groups of linkers (carboxylate, catecholate, imidazolate, pyrazolate, azolates, *etc*) they involve.[4] Each class of MOFs has its specific structure and composition characteristics, resulting in a family of materials with more extensive variety and multiplicity than any other porous materials. These aspects makeMOFs ideal candidates for various industrial applications, such as gas storage andseparation, catalysis, and clean environmental applications.[5]

1.2 Structural Design in Metal-Organic Frameworks

The success of MOFs relies on the rational synthesis of frameworks with desired structures, compositions, and properties, which has long been a central theme in this field of chemistry.

'Reticular synthesis' has been recognized as a key strategy for MOF design.[1] It refers to the process of assembling judiciously chosen rigid molecular building blocks into predetermined networks. The logical synthesis of the MOF is therefore achieved with the knowledge of the targeted network, the identification of the required building blocks, and the synthesis conditions that can reproducibly produce these building blocks. Here, MOF-5 is used to demonstrate how the reticular synthesis is employed (Figure 1.3). MOF-5 exhibits a **pcu** topological net,[1,3] in which each joint connects to six other adjacent joints (Figure 1.3a).

This connectivity is achieved by using $Zn_4O(CO_2)_6$ units made from four ZnO_4 tetrahedra sharing a common vertex and linked by six carboxylate groups, defining an octahedral "secondary building unit" (SBU). These SBU are then linked together by linear terephthalate linkers. Because the SBU and benzene links are rigid entities with specific directionality, a cubic network is formed. The octahedral SBUs act as joints connected by terephthalate struts. In practice, this compound can be prepared from Zn(II) salt and terephthalic acid under conditions pre-determined to yield the octahedral SBU *in situ*. This ability to direct the framework assembly in a predetermined way offers great perspectives to construct desirable structures, and this principle has successfully led to the explosive discovery and development of new MOF materials.

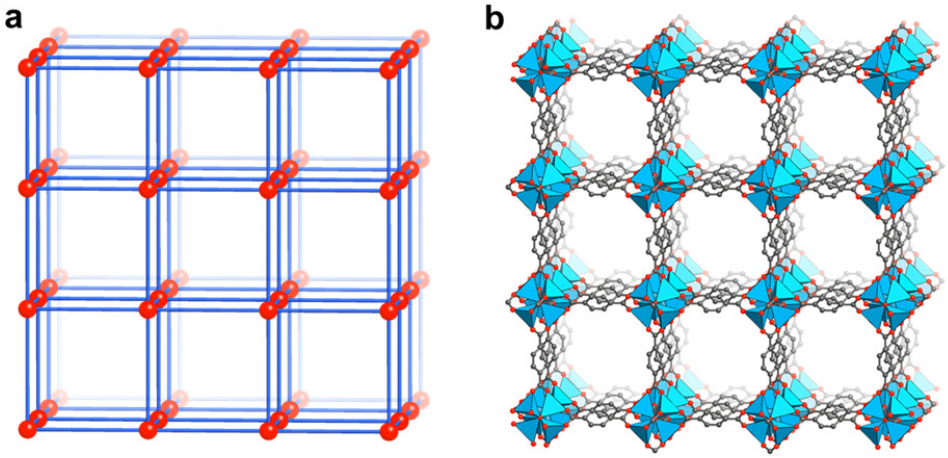

Figure 1.3 Reticular synthesis of MOF-5. (a) The **pcu** net of MOF-5 containing joints and struts. (b) Structure of MOF-5 where the joints are $Zn_4O(CO_2)_6$ units and struts are terephthalate linker. Red, blue, and gray spheres representing O, N, and C atoms, respectively. Zn_4O clusters are shown in blue tetrahedra.

However, MOFs can also be constructed from single metal ions instead of SBUs and more flexible organic linkers. This applies to a large portion of the reported MOFs, and for these materials it is difficult to design *a priori* synthesis, due to the high flexibility around the metal ions and/or the linkers, which can lead to a multiplicity of, sometimes unexpected, possible structures. This flexibility not only results in a wide range of potential strucutres, but also complicates structural control over the framework. Examples of MOFs suffering from this lack of predictability are zeolitic imidazolate frameworks (build around single metal ion nodes) (Figure 1.4),[6] and MOFs exhibiting environmentally-friendly naturally-occuring flexible linkers[7,8] A lot of efforts have been devoted to identify structural design principles for these MOFs, in order to rationally expand their families, as well as due to gain a better control over their unique pore structures and chemical compositions which are interesting for applications, but, so far, only with limited success.

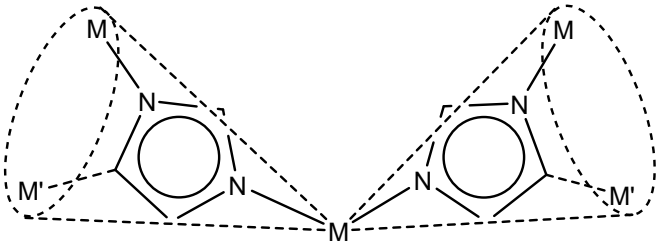

Figure 1.4 Schematic illustration of the flexible metal-imidazolate-metal connection in zeolitic imidazolate frameworks. The imidazolate can flip along the M-N bond to create numerous possible locations for the adjacent metal ions as shown by the dashed the cones.

1.3 Structure-Function Relationship for Applications

The successful implementation of MOFs in established and emerging industrial applications, such as molecular adsorption, separation, catalysis, clean energy and environment,[10-15] requires the capability to control their structure and to further understand structure-function relationship at the atomic level. The high crystallinity of MOFs makes this generally easy to study and successful design rules have been identified.[9] Herein, several examples are presented to show how a MOF can be designed for applications with the understanding of structure-function relationships (Figure 1.5).

Ultrahigh Porosity for Gas Storage. A lot of attention has been paid to increase the storage capacity of gaseous fuel gases (H_2, CH_4, *etc*) in porous materials, including MOFs. The total gas uptake of a MOF is generally directly related to the surface area and volume of its pores. Therefore, it is desirable to produce MOFs with high internal surface area and pore volume. One simple way to do it is to use longer organic linkers to provide larger pore space exemplified by MOF-177 and MOF-200 in Figure 1.5a and b. By using the longer 4,4′,4″-[benzene-1,3,5-triyl-tris(benzene-4,1-diyl)]tribenzoate (BBC) instead of 4,4′,4″-benzene-1,3,5-triyl-tribenzoate (BTB) present in MOF-177, the authors produced MOF-200,an expanded version of MOF-177 with the same topology. The Langmuir surface area and pore volume increased from 5340 m^2/g and 1.89 cm^3/g to 10400 m^2/g and 3.59 cm^3/g respectively, and thereby, the hydrogen uptake at 77 K and 80 bar increases from 6.9 wt% to 14.0 wt%.[10]

Open Metal Sites for Separation. Adsorbents and membranes represent two major approaches toward energy-efficient separation processes. MOFs are highly promising in this area due to their structural designability. For example, the creation of open metal sites within MOFs can be used to separate alkenes and alkanes, exemplified by an iron MOF, Fe_2(dobdc) (dobdc: 2,5-dioxido-1,4-benzenedicarboxylate) with open iron(II) sites that can selectively bind the unsaturated π bond (Figure 1.5c).[11] It is also possible to design MOFs with sharp pore shapes to discriminate between gas molecules simply based on their shape and size difference, as illustrated by another iron-based MOF, $Fe_2(BDP)_3$ (BDP: 1,4-benzenedipyrazolate), which is capable to separate hexane isomers based on their degrees of branching (Figure 1.5d).[12]

Creating Sites for Catalysis. Creating new catalytic sites within MOFs provides new opportunities for catalysis because of the unique combination of precise coordination geometries of metal ions and confined pore space found in MOFs. Metzger *et al.* installed isolated Ni atoms by cation exchange at the nodes of a MOF MFU-4*l* (MFU-4*l*= $Zn_5Cl_4(BTDD)_3$, H_2BTDD = bis(1*H*-1,2,3-triazolo[4,5-*b*],[4′,5′-i])dibenzo[1,4]dioxin), to create a site-isolated Ni(II) active site bearing close structureal homology to molecular tris-pyrazolylborate complexes due to the nickel-triazolate coordination environment. This MOF

turned out to be catalytically active for the dimerization of ethylene to 1-butene with a combination of selectivity (96.2%) and activity (41,500 mol per mole of Ni per hour) that is premier among all heterogeneous catalysts attributing to the isolated Ni catalytic center in a confined space (Figure 1.5e,f).[13]

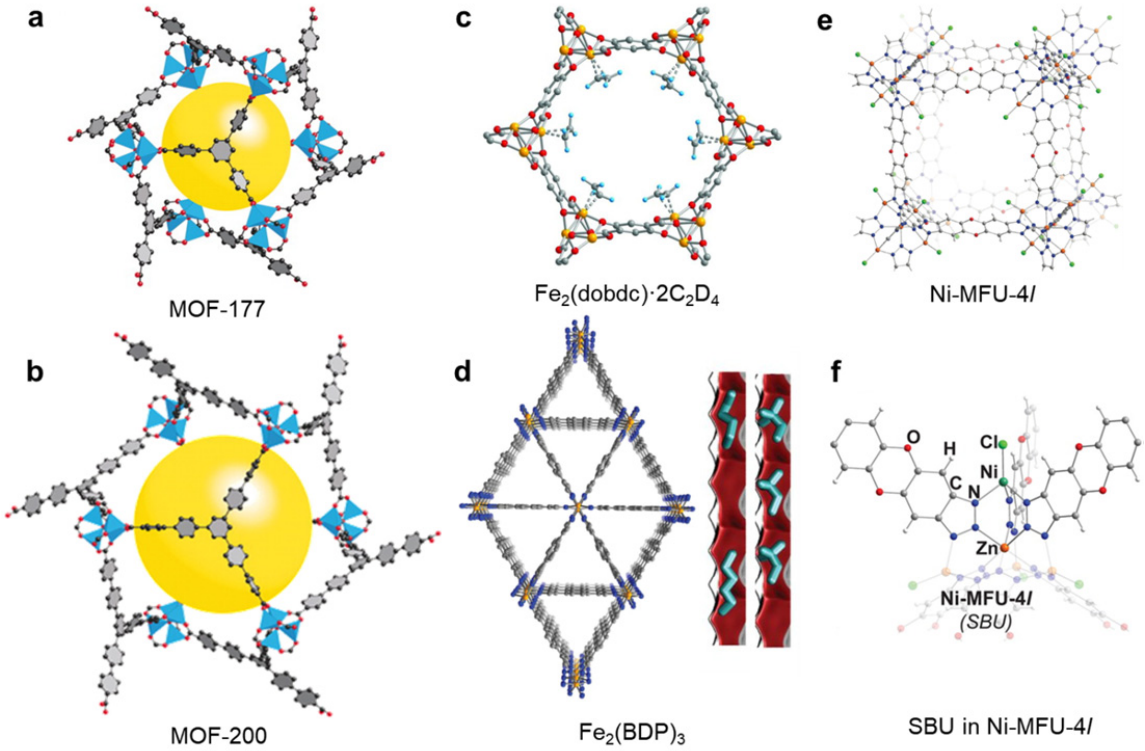

Figure 1.5 Structural design of MOFs for industrial applications. (a,b) Reticular expansion of MOF-177 to MOF-200 with ultrahigh porosity for hydrogen storage. Adapted with permission from ref 10. Copyright 2010 The American Association for the Advancement of Science (c) open metal sites in MOFs for ethylene/ethane separation. Adapted with permission from ref 11. Copyright 2012 The American Association for the Advancement of Science (d) triangular shaped channels in MOFs for hexanes separation. Adapted with permission from ref 12. Copyright 2013 The American Association for the Advancement of Science (e,f) Structure of Ni-MFU-4*l* highlighting the exposure of the catalytic Ni center to the pores. Adapted with permission from ref 13. Copyright 2016 American Chemical Society.

1.4 Conclusions

MOFs have progressed substantially since their original inception two decades ago. The easy structural designability provided by the principals of reticular synthesis has boosted the discovery of numerous MOF structures as well as the expansion of their potential uses in industrial applications. However, there are still many important MOFs with unique structural characters whose synthesis remains hard to consistently guide (see section 1.2). Identifiying rational rules of reticular synthesis for these MOFs would lead not only to a rapid expansion of their diversity, but also greatly improve chances to design and optimize properties specific to these classes of materials.

1.5 References

[1] Yaghi, O. M.; O'Keeffe, M.; Ockwig, N. W.; Chae, H. K.; Eddaoudi, M.; Kim, J. *Nature* **2003**, *423*, 705.
[2] Furukawa, H.; Cordova, K. E.; O'Keeffe, M.; Yaghi, O. M. *Science*, **2013**, *341*, 1230444.
[3] Li, H.; Eddaoudi, M.; O'Keeffe, M.; Yaghi, O. M. *Nature* **1999**, *402*, 276.
[4] Kaskel, S. *The Chemistry of Metal-Organic Frameworks: Synthesis, Characterization, and Applications*; Wiley-VCH: Weinheim, 2016.
[5] Schröder, M. *Functional Metal-Organic Frameworks: Gas Storage, Separation and Catalysis;* Springer: Berlin, 2010.
[6] Park, K. S.; Ni, Z.; Côté, A. P.; Choi, J. Y.; Huang, R. D.; Uribe-Romo, F. J.; Chae, H. K.; O'Keeffe, M.; Yaghi, O. M. *Proc. Natl. Acad. Sci. U.S.A.* **2006**, *103*, 10186.
[7] Forgan, R.S. Metal-Organic Frameworks: Edible Frameworks. *Encyclopedia of Inorganic and Bioinorganic Chemistry*; John Wiley & Sons: New York, 2014.
[8] Imaz, I.; Rubio-Martínez, M.; An, J.; Solé-Font, I.; Rosi, N. L.; Maspoch, D. *Chem. Comm.* **2011**, *47*, 7287.
[9] Slate, A. G.; Cooper, A. I. *Science* **2015,** *348*, 988.
[10] Furukawa, H.; Ko, N.; Go, Y. B.; Aratani, N.; Choi, S. B.; Choi, E.; Yazaydin, A. O.; Snurr, R. Q.; O'Keeffe, M.; Kim, J.; Yaghi, O. M. *Science* **2010**, *239*, 424.
[11] Bloch, E. D.; Queen, W. L.; Krishna, R.; Zadrozny, J. M.; Brown, C. M.; Long, J. R. *Science* **2012**, *335*, 1606.
[12] Herm, Z. R.; Wiers, B. M.; Mason, J. A.; van Baten, J. M.; Hudson, M. R.; Zajdel, P.; Brown, C. M.; Masciocchi, N.; Krishna, R.; Long, J. R. *Science* **2013**, *340*, 960.
[13] Metzger, E. D.; Brozek, C. K.; Comito, R. J.; Dincă, M. *ACS Cent. Sci.* **2016**, *2*, 148.
[14] Schoedel, A.; Ji, Z.; Yaghi, O. M. *Nature Energy* **2016**, *1*, 16034.
[15] Zhang, H.; Nai, J.; Yu, L.; Lou, X. W. *Joule* **2017**, *1*, 77.

Chapter 2: A Mixed-linker Approach toward Zeolitic Imidazolate Frameworks with Large Pores and Apertures

2.1 Introduction

Zeolitic imidazolate frameworks (ZIFs) are an important category of metal-organic frameworks (MOFs). ZIFs are constructed by linking tetrahedrally-coordinated metal ions with organic imiadzolate (Im) linkers[1], the presence of which distinguishes ZIFs from the inorganic zeolites. In particular, the similar angle of the Metal-Im-Metal linkage in ZIFs as the Si-O-Si angle in zeolites endows ZIFs with zeolitic structures[2] (Figure 2.1). Their characteristic pore geometries, functionalities, as well as exceptional thermal and chemical stabilities provide them with unique advantages with respect to gas storage, separations, and catalysis.[2-4]

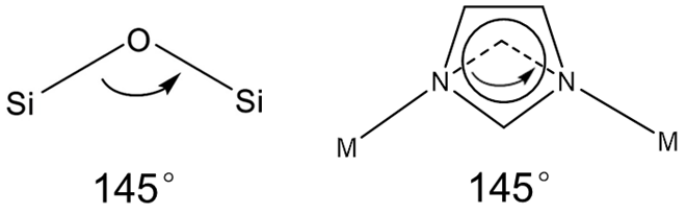

Figure 2.1 Similar 145° angle between Si-O-Si and Metal-Im-Metal linkage.

The designed synthesis of ZIFs remains as a challenge. Unlike the metal cluster-based synthetic strategy to make MOFs, where the directionality and rigidity of molecular building blocks allow for the reticular synthesis approach, the rotational flexibility of the metal-linker-metal connections in ZIFs rules out such possibility. This has led to the lack of structural diversity which impeded the development of the field. Indeed, there are less than 50 topologies that have been discovered in ZIFs, while there are more than 200 topologies known in zeolites,[5] thousands in MOFs,[6] while more than 5 million hypothetical tetrahedral networks awaits for exploration.[7]

Few ZIFs discovered possess large pores and apertures, while these two structural characters are increasely in demand for applications in storage, separation, and catalysis, as bigger pores and apertures allow the entry of large guest molecules.[8] So far, only 9 ZIFs with **moz**,[3] **poz**,[3] LTA,[9] RHO,[10] **zea**,[11] GME,[10] CHA,[12] MER,[10] and AFI[13] topologies have a cage size above 2 nm (diameter of the largest fitting sphere in the cage without considering the size of imidazolate linkers).

My initial interest is to create ZIFs with large pores and apertures. For the first time, three types of imidazolate with different sizes were introduced and assembled into an ordered framework in a one-pot reaction, which demonstrated to be essential for the construction of ZIFs with large pores and apertures. The rationale of the mixed-linker apporach as well as the refinement and generalization of the design principles for ZIFs will be discussed in Chapter 3. In this Chapter, I will focus on the synthesis and structures of the new fifteen ZIFs made by the mixed-linker approach.

2.2 Materials and Methods

General synthetic procedure and characterization of ZIFs. The ZIFs reported in

this study[14] were synthesized by mixing two or three Im linkers chosen from the series IM (imidazole), nIM (2-nitroimidazole), mIM (2-methylimidazole), aIM (imidazole-2-carboxaldehyde), 4-nIM (4-nitroimidazole), bIM (benzimidazole), 2-mbIM (2-methylbenzimdazole), cbIM (5-chlorobenzimidazole), mbIM (5-methylbenzimidazole), bbIM (5-bromobenzimidazole), and nbIM (5-nitrobenzimidazole) with a zinc(II) salt (nitrate and trifluorosulfate) in *N*,*N*-dimethylformamide or *N*,*N*-diethylformamide. Crystals of each of the ZIFs, suitable for single crystal X-ray diffraction analysis, were obtained after heating the solution within the temperatures range of 65 to 130 °C and for a period of 3 to 30 days. Varying the combination and stoichiometry of Im linkers led to the discovery of fifteen new ZIFs with their structures identified by using either synchrotron or laboratory based X-ray diffraction techniques. The exact molar ratio of the Im linkers in each ZIF was further confirmed by ^{1}H-NMR spectroscopy and elemental microanalyses of the guest-free samples. All the synthetic procedures were conducted in open air. The ZIFs were activated by the following procedure: firstly, the as-synthesized crystalline material was immersed in anhydrous DMF for three days, exchanged with fresh DMF three times per day; then the crystals are immersed in anhydrous acetone for three days, exchanged with fresh acetone three times per day. After that, the ZIFs were fully exchanged with liquid CO_2 for six times, and further kept under supercritical CO_2 atmosphere for 1 h before being bled using a Tousimis Samdri PVT-3D critical point dryer. The samples were finally evacuated to remove guest molecules under vacuum (0.01 Torr) at ambient temperature for 4 h, then at elaborated temperature of 50 °C for 4 h, 100 °C for 4 h, 150 °C for 4 h and finally 180 °C for 12 h to give the activated samples. The following measurements were conducted using the activated samples for each ZIF unless otherwise noted. Elemental analysis (EA) of activated ZIFs were measured using a Perkin Elmer 2400 Series II CHNS elemental analyzer; attenuated-total-reflectance Fourier-transform infrared (ATR-FTIR) spectra of neat ZIFs were recorded on a Bruker ALPHA Platinum ATR-FTIR Spectrometer.

ZIF-303 (CHA), **$Zn(cbIM)_{0.70}(nIM)_{0.30}(IM)_{1.00}$.** A mixture of $Zn(NO_3)_2{\cdot}4H_2O$ (0.1 mmol, 0.5 mL of 0.2 M stock solution in DMF), HnIM (0.1 mmol, 0.5 mL of 0.2 M stock solution in DMF), HIM (0.2 mmol, 1.0 mL of 0.2 M stock solution in DMF), and HcbIM (0.1 mmol, 0.5 mL of 0.2 M stock solution in DMF) was sealed in a 4-mL glass vial and heated at 120 °C for 72 h. Yellow hexagonal plate crystals were collected and washed with anhydrous DMF (3 × 4 ml). (Yield: 49% based on Zn). EA: Calcd. for $Zn(C_3H_2N_3O_2)_{0.30}(C_3H_3N_2)(C_7H_4N_2Cl)_{0.70}$: C, 38.83; H, 2.37; N, 22.13%. Found: C, 37.86; H, 2.25; N, 23.11%. ATR-FTIR (4000-400 cm^{-1}): 1608(w), 1574(w), 1539(w), 1494(s), 1472(s), 1435(m), 1365(s), 1341(m), 1321(w), 1288(m), 1238(m), 1192(m), 1171(s), 1126(w), 1088(s), 1062(m), 1013(w), 978(w), 953(s), 928(m), 832(m), 801(s), 756(s), 723(m), 669(s), 649(m), 598(m), 571(w), 482(m), 425(m).

ZIF-360 (KFI), $Zn(bIM)_{1.00}(nIM)_{0.70}(IM)_{0.30}$. A mixture of $Zn(NO_3)_2{\cdot}4H_2O$ (0.1 mmol, 0.5 mL of 0.2 M stock solution in DEF), HnIM (0.3 mmol, 1.5 mL of 0.2 M stock solution in DEF), HIM (0.1 mmol, 0.5 mL of 0.2 M stock solution in DEF), and HbIM (0.2 mmol, 1.0 mL of 0.2 M stock solution in DEF) was sealed in a 4-mL glass vial and heated at 100 °C for 72 h. Transparent trigonal prism crystals were collected from the wall and washed with anhydrous DEF (3 × 4 ml). (Yield: 38% based on Zn). EA: Calcd. for $Zn(C_3H_2N_3O_2)_{0.70}(C_3H_3N_2)_{0.30}(C_7H_5N_2)$: C, 42.73; H, 2.62; N, 23.42%. Found: C, 39.39; H, 2.48; N, 22.72%. ATR-FTIR (4000-400 cm^{-1}): 1611(m), 1539(m), 1476(s), 1364(s), 1301(m), 1278(m), 1244(s), 1198(w), 1173(s), 1118(w), 1091(s), 1005(w), 952(s), 908(s), 831(s), 793(m), 775(m), 740(s), 668(w), 651(s), 572(m), 552(m), 464(s), 427(s).

ZIF-365 (KFI), $Zn(cbIM)_{0.95}(nIM)_{0.60}(IM)_{0.45}$. A mixture of $Zn(NO_3)_2{\cdot}4H_2O$ (0.1 mmol, 0.5 mL of 0.2 M stock solution in DEF), HnIM (0.22 mmol, 1.1 mL of 0.2 M stock solution in DEF), HIM (0.1 mmol, 0.5 mL of 0.2 M stock solution in DEF), and HcbIM (0.2 mmol, 1.0 mL of 0.2 M stock solution in DEF) was sealed in a 4-mL glass vial and heated at

100 °C for 72 h. Transparent trigonal prism crystals were collected from the wall and washed with anhydrous DEF (3 × 4 ml). (Yield: 34% based on Zn). EA: Calcd. for $Zn(C_3H_2N_3O_2)_{0.60}(C_3H_3N_2)_{0.45}(C_7H_4N_2Cl)_{0.95}$: C, 38.36; H, 2.09; N, 21.00%. Found: C, 35.90; H, 2.01; N, 20.67%. ATR-FTIR (4000-400 cm^{-1}): 1644(w), 1610(w), 1537(w), 1471(s), 1360(s), 1287(m), 1253(w), 1238(m), 1192(w), 1172(s), 1125(w), 1090(s), 1063(m), 951(s), 927(s), 852(w), 831(s), 800(s), 757(m), 723(s), 668(w), 650(s), 598(s), 571(m), 512(w), 481(s), 459(w), 425(s).

ZIF-376 (LTA), $Zn(nbIM)_{0.83}(mIM)_{0.25}(IM)_{0.92}$. A mixture of $Zn(NO_3)_2{\cdot}4H_2O$ (0.14 mmol, 0.7 mL of 0.2 M stock solution in DMF), HmIM (0.3 mmol, 1.5 mL of 0.2 M stock solution in DMF), HIM (0.1 mmol, 0.5 mL of 0.2 M stock solution in DMF), and HnbIM (0.2 mmol, 1.0 mL of 0.2 M stock solution in DMF) was sealed in a 4-mL glass vial and heated at 130 °C for 72 h, then cool down to room temperature. Transparent octahedral crystals (**ucb ZIF-414**) and brown cubic crystals were found on the wall, the cubic crystals were collected and analyzed by Single-crystal X-ray diffraction as **ZIF-376**. This ZIF was not purified or activated, a few crops of crystals were picked up manually for powder X-ray and digested ^{1}H-NMR studies.

ZIF-386 (AFX), $Zn(nbIM)_{0.85}(nIM)_{0.70}(IM)_{0.45}$. A mixture of $Zn(NO_3)_2{\cdot}4H_2O$ (0.1 mmol, 0.5 mL of 0.2 M stock solution in DMF), HnIM (0.3 mmol, 1.5 mL of 0.2 M stock solution in DMF), HIM (0.1 mmol, 0.5 mL of 0.2 M stock solution in DMF), and HnbIM (0.2 mmol, 1.0 mL of 0.2 M stock solution in DMF) was sealed in a 4-mL glass vial and heated at 120 °C for 72 h. Yellow hexagonal plate crystals were collected and washed with anhydrous DMF (3 × 4 ml). (Yield: 38% based on Zn). EA: Calcd. for $Zn_2(C_3H_2N_3O_2)_{1.40}(C_3H_3N_2)_{0.90}(C_7H_4N_3O_2)_{1.70}$: C, 36.21; H, 1.99; N, 24.93%. Found: C, 35.33; H, 2.02; N, 24.37%. ATR-FTIR (4000-400 cm^{-1}): 1649(m), 1615(m), 1591(w), 1518(s), 1496(s), 1475(s), 1412(w), 1364(s), 1343(s), 1305(s), 1290(s), 1258(w), 1235(m), 1196(m), 1171(s), 1126(m), 1091(s), 1068(m), 1012(m), 981(w), 950(s), 885(m), 831(s), 795(s), 763(m), 736(s), 709(m), 668(m), 654(m), 623(w), 595(m), 573(m), 543(m), 503(w), 467(w), 450(m), 424(m).

ZIF-408, $Zn(cbIM)_{1.87}(mIM)_{0.08}(OH)_{0.05}$. A mixture of $Zn(NO_3)_2{\cdot}4H_2O$ (0.04 mmol, 0.2 mL of 0.2 M stock solution in DMF), HmIM (0.02 mmol, 0.1 mL of 0.2 M stock solution in DMF), and HcbIM (0.2 mmol, 1 mL of 0.2 M stock solution in DMF), and 0.6 mL DMF were sealed in a 4-mL glass vial and heated at 65 °C for 28 days, large cubic crystals were collected and washed with anhydrous DMF (3 × 4 ml). This ZIF was not activated, a few crops of crystals were picked up for powder X-ray and digested ^{1}H-NMR studies.

ZIF-410 (GME), $Zn(cbIM)_{1.10}(aIM)_{0.90}$. A mixture of $Zn(CF_3SO_3)_2$ (0.2 mmol, 1 mL of 0.2 M stock solution in DMF), HaIm (0.2 mmol, 1 mL of 0.2 M stock solution in DMF), and HcbIm (0.3 mmol, 1.5 mL of 0.2 M stock solution in DMF) was sealed in a 4-mL glass vial and heated at 85 °C for 96 h. Transparent hexagonal plate crystals were collected and washed with anhydrous DMF (3 × 4 ml). (Yield: 15% based on Zn).EA: Calcd. for $Zn(C_4H_3N_2O)_{0.90}(C_7H_4N_2Cl)_{1.10}$: C, 42.72; H, 2.25; N, 17.64%. Found: C, 41.92; H, 2.15; N, 17.60%. ATR-FTIR (4000-400 cm^{-1}): 1680(br), 1609(w), 1574(w), 1460(br), 1415(s), 1360(m), 1340(w), 1323(w), 1287(w), 1238(m), 1190(s), 1169(s), 1128(w), 1063(m), 953(m), 928(m), 852(w), 789(br), 758(w), 723(s), 700(w), 648(w), 598(s), 533(w), 481(s), 425(s). I chose the non-oxidative metal source–$Zn(CF_3SO_3)_2$ as well as relatively low reaction temperature (85 °C) to avoid the potential oxidation of the carboxaldehyde group in 2-Imidazolecarboxaldehyde.

ZIF-486 (GME), $Zn(nbIM)_{0.20}(mIM)_{0.65}(IM)_{1.15}$. A mixture of $Zn(NO_3)_2{\cdot}4H_2O$ (0.12 mmol, 0.6 mL of 0.2 M stock solution in DMF), HmIM (0.3 mmol, 1.5 mL of 0.2 M stock solution in DMF), HIM (0.24 mmol, 1.2 mL of 0.2 M stock solution in DMF), and HnbIM (0.06 mmol, 0.3 mL of 0.2 M stock solution in DMF) was sealed in a 4-mL glass vial and heated at 130 °C for 48 h. Transparent hexagonal crystals were collected by sonication

and washed with anhydrous DMF (3 × 4 ml). (Yield: 38% based on Zn). EA: Calcd. for $Zn(C_4H_5N_2)_{0.65}(C_3H_3N_2)_{1.15}(C_7H_4N_3O_2)_{0.20}$: C, 39.30; H, 3.32; N, 25.84%. Found: C, 39.32; H, 3.09; N, 25.68%. ATR-FTIR (4000-400 cm^{-1}): 1614(w), 1591_w), 1514(w), 1500(w), 1476(m), 1462(w), 1422(w), 1379(w), 1346(m), 1307(w), 1292(w), 1243(m), 1198(w), 1173(m), 1144(m), 1088(s), 993(w), 954(s), 840(w), 797(w), 753(s), 737(m), 709(w), 691(w), 670(s), 594(w), 544(w), 484(w), 451(w), 422(s).

ZIF-412 (ucb), $Zn(bIM)_{1.13}(nIM)_{0.62}(IM)_{0.25}$. A mixture of $Zn(NO_3)_2{\cdot}4H_2O$ (0.1 mmol, 0.5 mL of 0.2 M stock solution in DMF), HnIM (0.3 mmol, 1.5 mL of 0.2 M stock solution in DMF), IM (0.1 mmol, 0.5 mL of 0.2 M stock solution in DMF), HbIM (0.2 mmol, 1.0 mL of 0.2 M stock solution in DMF) and 0.5 mL more DMF was sealed in a 4-mL glass vial and heated at 120 °C for 4 days, then cooled down at 1 °C/min. Polyhedral shaped crystals were collected from the wall (few impure large orange crystals at the bottom were removed) and washed with anhydrous DMF (3 × 4 mL) (Yield: 46% based on Zn). Single crystal suitable for single-crystal X-ray diffraction studies were grown in similar condition but with 1 mL DMF in 20-mL glass vial. EA: Calcd. for $Zn_3(C_3H_2N_3O_2)_{1.85}(C_3H_3N_2)_{0.75}(C_7H_5N_2)_{3.40}$: C, 44.55; H, 2.71; N, 22.77%. Found: C, 43.30; H, 2.62; N, 22.76%. ATR-FTIR (4000-400 cm^{-1}): 1612(w), 1541(w), 1476(s), 1367(s), 1301(m), 1278(m), 1244(s), 1198(s), 1175(w), 1119(m), 1092(w), 1005(m), 952(m), 909(m), 831(w), 794(w), 776(m), 740(s), 670(w), 650(m), 573(w), 552(w), 464(m), 425(m).

ZIF-413 (ucb), $Zn(mbIM)_{1.03}(nIM)_{0.64}(IM)_{0.33}$. A mixture of $Zn(NO_3)_2{\cdot}4H_2O$ (0.1 mmol, 0.5 mL of 0.2 M stock solution in DMF), HnIM (0.3 mmol, 1.5 mL of 0.2 M stock solution in DMF), HIM (0.1 mmol, 0.5 mL of 0.2 M stock solution in DMF), and HmbIM (0.2 mmol, 1.0 mL of 0.2 M stock solution in DMF) was sealed in a 4 mL glass vial and heated at 120 °C for 4 days, then cooled down at 1°C/min. Polyhedral shaped crystals were collected and washed with anhydrous DMF (3 × 4 mL). (Yield: 43% based on Zn). EA: Calcd. for $Zn_3(C_3H_2N_3O_2)_{1.90}(C_3H_3N_2)(C_8H_7N_2)_{3.10}$: C, 45.58; H, 3.25; N, 22.06%. Found: C, 44.83; H, 3.16; N, 21.80%. ATR-FTIR (4000-400 cm^{-1}): 1620(w), 1539(m), 1473(s), 1366(s), 1290(s), 1243(s), 1205(s), 1173(s), 1143(w), 1131(m), 1091(s), 1021(w), 950(s), 830(s), 824(s), 799(s), 761(s), 668(m), 652(s), 625(m), 604(m), 572(m), 495(m), 468(s), 427(s).

ZIF-414 (ucb), $Zn(nbIM)_{0.91}(mIM)_{0.62}(IM)_{0.47}$. A mixture of $Zn(NO_3)_2{\cdot}4H_2O$ (0.1 mmol, 0.5 mL of 0.2 M stock solution in DMF), HmIM (0.3 mmol, 1.5 mL of 0.2 M stock solution in DMF), HIM (0.075 mmol, 0.375 mL of 0.2 M stock solution in DMF), and HnbIM (0.225 mmol, 1.125 mL of 0.2 M stock solution in DMF) was sealed in a 4-mL glass vial and heated at 130 °C for 48 h, then cool down to room temperature at 0.1 °C/min . Transparent octahedral crystals were collected and washed with anhydrous DMF (3 × 4 ml). (Yield: 50% based on Zn). EA: Calcd. for $Zn_3(C_4H_5N_2)_{1.85}(C_3H_3N_2)_{1.40}(C_7H_4N_3O_2)_{2.75}$: C, 41.82; H, 2.78; N, 23.32%. Found: C, 40.98; H, 2.44; N, 22.91%. ATR-FTIR (4000-400 cm^{-1}): 1615(w), 1591(w), 1518(m), 1463(m), 1443(w), 1425(w), 1378(w), 1343(s), 1289(s), 1257(w), 1234(m), 1196(w), 1182(w), 1146(w), 1127(w), 1069(s), 994(w), 949(m), 886(w), .823(w), 796(s), 757(m), 736(s), 709(m), 689(w), 670(m), 648(w), 594(w), 544(w), 424(s).

ZIF-516 (ykh), $Zn(bbIM)_{0.77}(mbIM)_{1.23}(DMF)_{0.05}$. A mixture of $Zn(NO_3)_2{\cdot}4H_2O$ (0.04 mmol, 0.2 mL of 0.2 M stock solution in DMF), HmbIM (0.2 mmol, 1 mL of 0.2 M stock solution in DMF), HbbIM (0.2 mmol, 1 mL of 0.2 M stock solution in DMF) and 70 μL water was sealed in a 4-mL glass vial and heated at 130 °C for 4 days. Transparent crystals were collected and washed with anhydrous DMF (3 × 4 ml). (Yield: 72% based on Zn). EA: Calcd. for $Zn(C_8H_7N_2)_{1.23}(C_7H_4N_2Br)_{0.77}(C_3H_7NO)_{0.05}$: C, 48.45; H, 3.18; N, 14.88%. Found: C, 48.37; H, 3.20; N, 14.76%. ATR-FTIR (4000-400 cm^{-1}): 1603(w), 1469(s, br), 1340(m), 1286(m), 1240(s), 1203(m), 1180(m), 1141(w), 1130(m), 1052(w), 1017(w), 944(w), 917(m), 857(w), .822(w), 798(s), 760(m), 703(m), 648(s), 585(m), 468(s), 423(s).

ZIF-586 (ykh), $Zn(mbIM)_{1.72}(2\text{-}mbIM)_{0.28}$. A mixture of $Zn(NO_3)_2{\cdot}4H_2O$ (0.04

mmol, 0.2 mL of 0.2 M stock solution in DMF), 2-HmbIM (0.12 mmol, 0.6 mL of 0.2 M stock solution in DMF), and HmbIM (0.13 mmol, 0.65 mL of 0.2 M stock solution in DMF) was sealed in a 4-mL glass vial and heated at 130 °C for 3 days. Plate crystals were found along with powders. and washed with anhydrous DMF (3 × 4 ml). This ZIF was not activated, a few crops of crystals were picked up for powder X-ray and digested ^{1}H-NMR studies.

ZIF-615 (gcc), Zn(cbIM)$_{1.05}$(4-nIM)$_{0.95}$. A mixture of $Zn(NO_3)_2{\cdot}4H_2O$ (0.08 mmol, 0.4 mL of 0.2 M stock solution in DMF), 4-HnIM (0.12 mmol, 0.6 mL of 0.2 M stock solution in DMF), and HcbIM (0.08 mmol, 0.4 mL of 0.2 M stock solution in DMF) was sealed in a 4-mL glass vial and heated at 130 °C for 96 h. needle crystals were collected and washed with anhydrous DMF (3 × 4 ml). (Yield: 38% based on Zn). EA: Calcd. for $Zn(C_3H_2N_3O_2)_{0.95}$ $(C_7H_4N_2Cl)_{1.05}$: C, 37.01; H, 1.86; N, 20.95%. Found: C, 34.85; H, 1.97; N, 19.58%. ATR-FTIR (4000-400 cm^{-1}): 1610(w), 1575(w), 1534(m), 1513(m), 1470(s), 1381(s), 1368(s), 1340(m), 1287(m), 1245(s), 1219(w), 1191(m), 1107(s), 1064(m), 1036(m), 974(w), .928(m), 852(s), 824(s), 800(s), 752(m), 724(m), 665(s), 648(m), 598(m), 482(m), 424(m).

ZIF-725 (bam), Zn(bbIM)$_{1.35}$(nIM)$_{0.40}$(IM)$_{0.25}$. A mixture of $Zn(NO_3)_2{\cdot}4H_2O$ (0.1 mmol, 0.5 mL of 0.2 M stock solution in DMF), HnIM (0.085 mmol, 0.425 mL of 0.2 M stock solution in DMF), IM (0.1 mmol, 0.5 mL of 0.2 M stock solution in DMF), and HbbIM (0.4 mmol, 2.0 mL of 0.2 M stock solution in DMF) was sealed in a 4-mL glass vial and heated at 65 °C for 12 days. Colorless rod-shaped crystals were collected and washed with anhydrous DMF (3 × 4 ml). (Yield: 19% based on Zn). EA: Calcd. for $Zn_2(C_3H_2N_3O_2)_{0.80}(C_3H_3N_2)_{0.50}(C_7H_4N_2Br)_{2.70}$: C, 34.96; H, 1.79; N, 15.74%. Found C, 34.80; H, 1.57; N, 15.35%. ATR-FTIR (4000-400 cm-1): 1604(m), 1572(w), 1537(w), 1494(s), 1471(s), 1431(m), 1365(s), 1339(s), 1287(s), 1250(s), 1238(s), 1187(s), 1135(s), 1129(m), 1092(s), 1052(s), 1013(w), 952(m), 918(s), 852(m), 831(m), 793(s), 757(m), 705(s), 669(m), 648(s), 586(s), 478(s), 423(s).

^{1}H-NMR spectroscopy. ^{1}H NMR spectra of digested ZIFs were acquired on a Bruker AVB-400 NMR spectrometer, with chemcial shifts of imidazoles identified by comparing with spectra for each pure linker, samples (*ca.* 10 mg for each) were dissolved in DMSO-d_6 (deuterated dimethyl sulfoxide, 580 μL) and 20% DCl in D_2O (20 μL) with sonication.

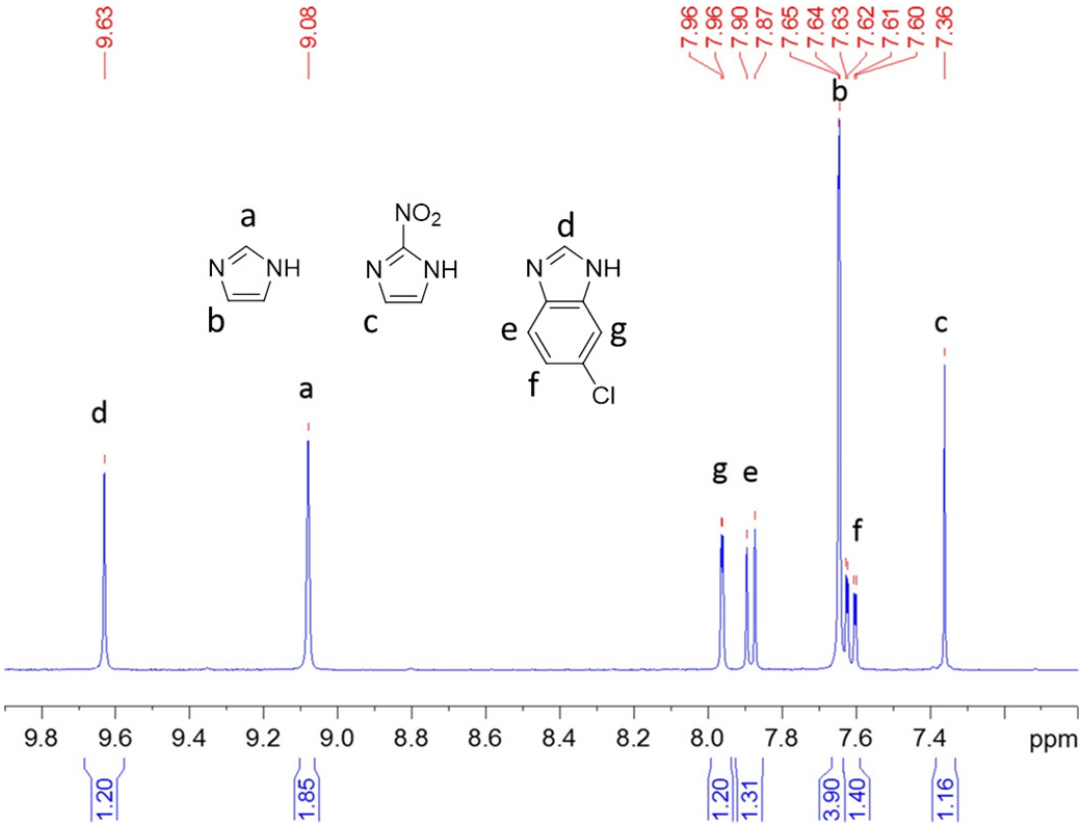

Figure 2.2 ^{1}H-NMR spectrum of digested ZIF-303.

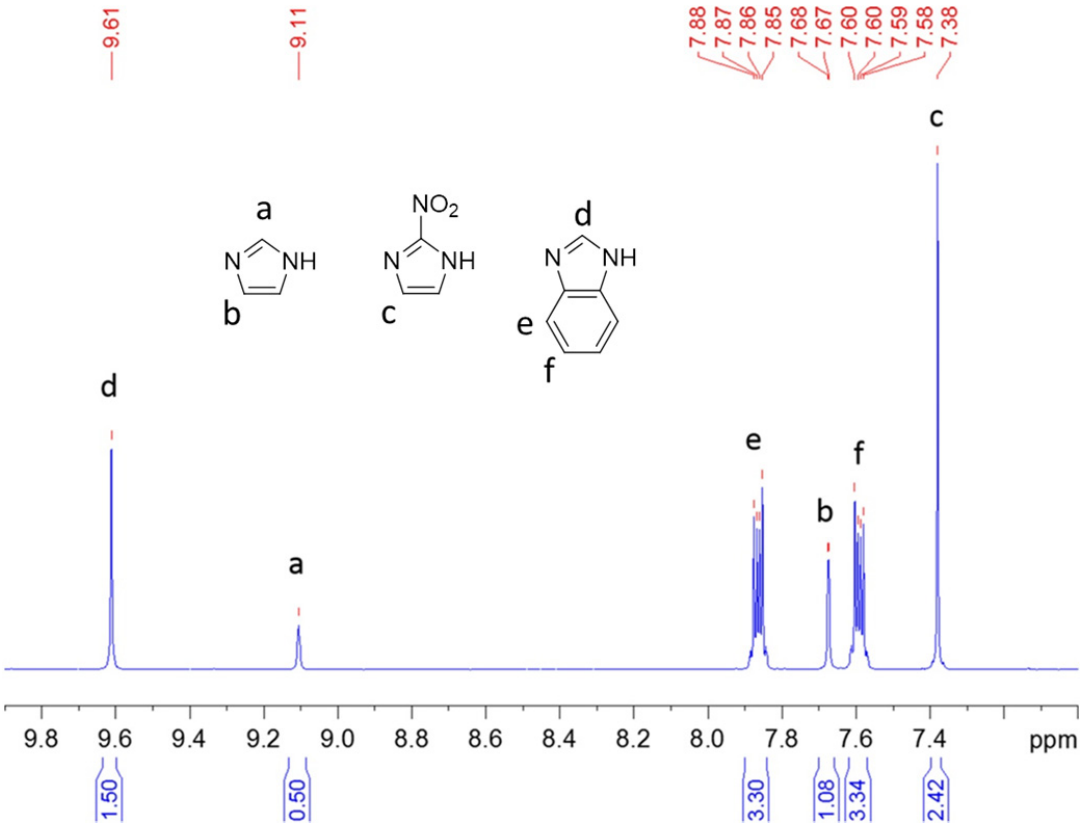

Figure 2.3 ^{1}H-NMR spectrum of digested ZIF-360.

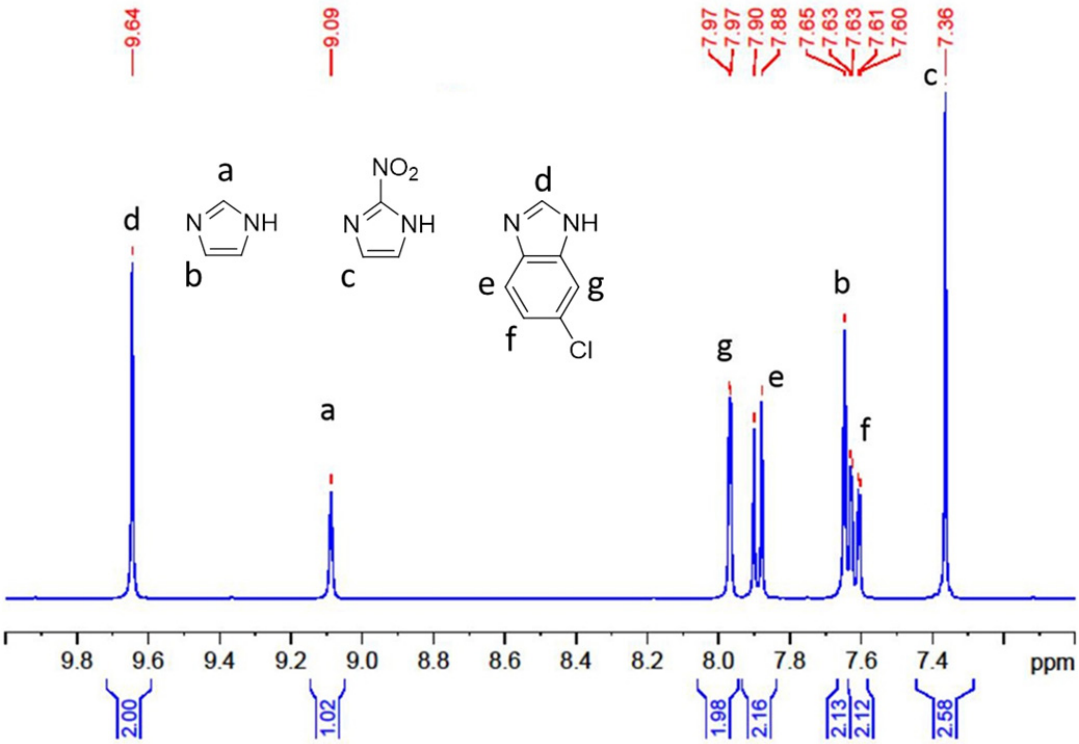

Figure 2.4 ^{1}H-NMR spectrum of digested ZIF-365.

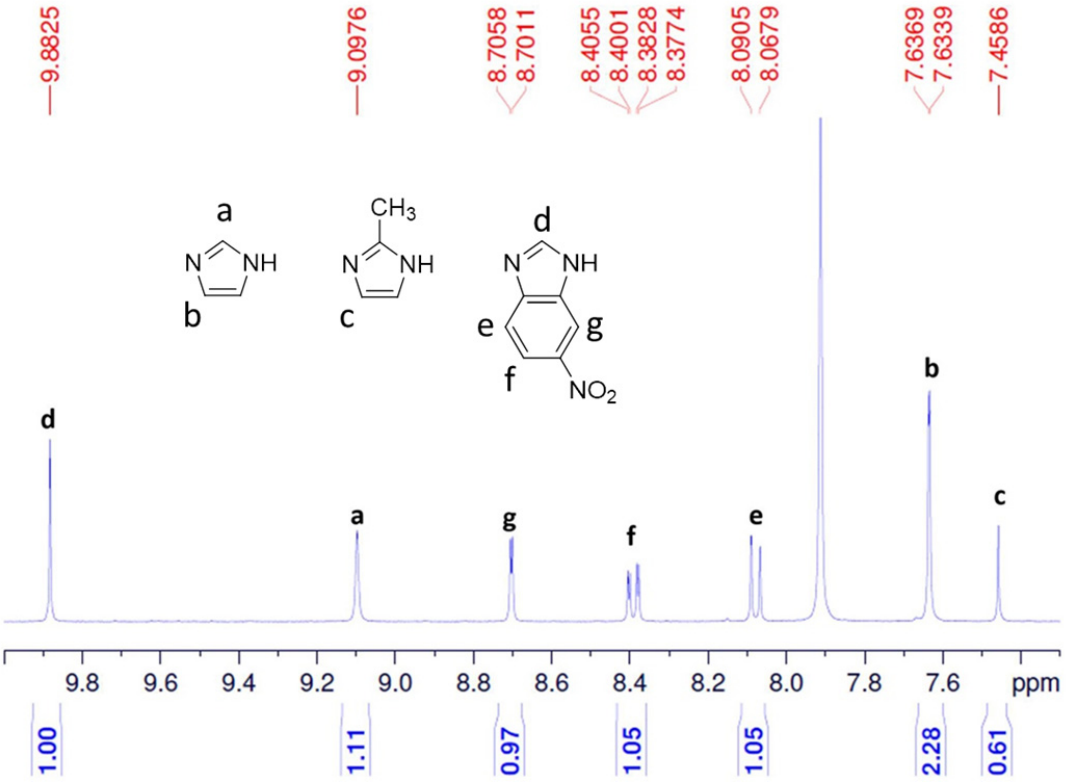

Figure 2.5 ^{1}H-NMR spectrum of digested ZIF-376.

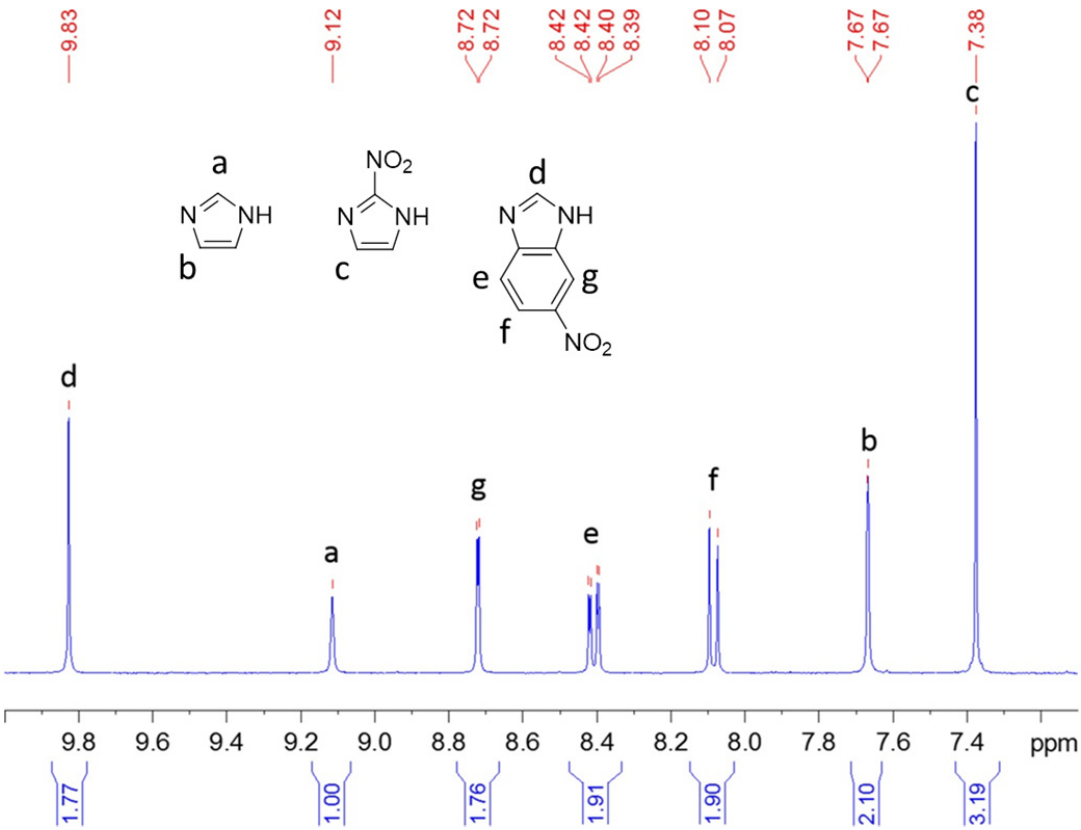

Figure 2.6 ^{1}H-NMR spectrum of digested ZIF-386.

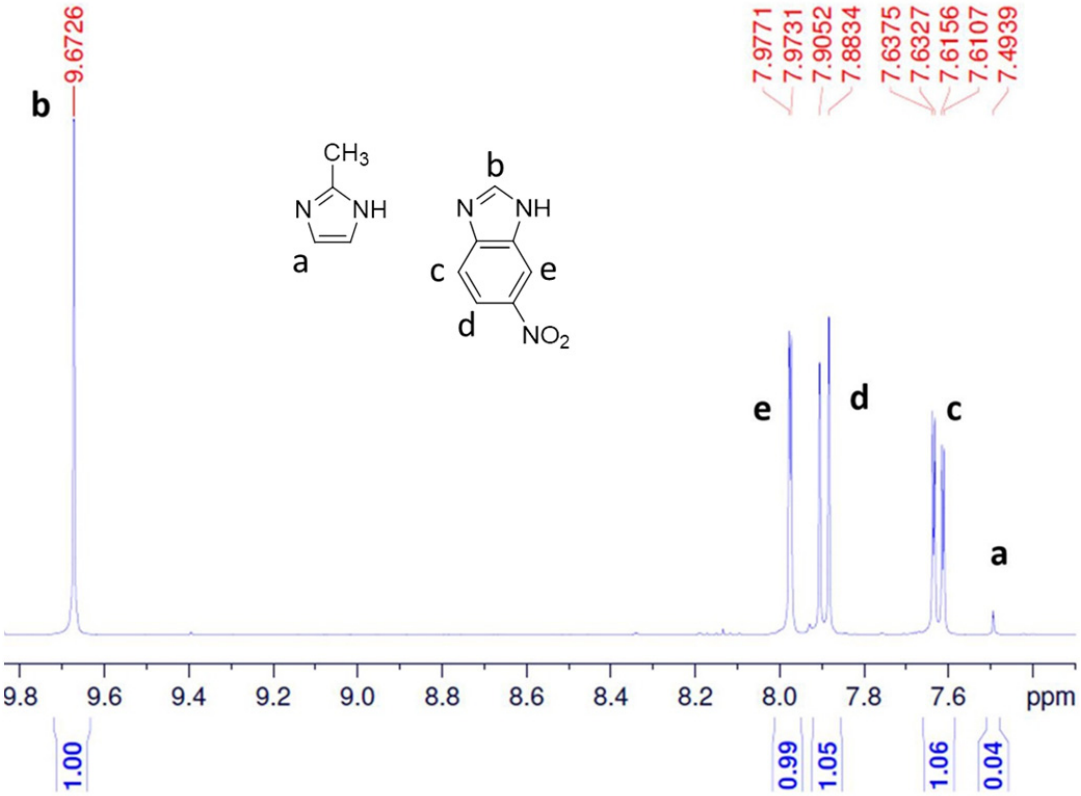

Figure 2.7 ^{1}H-NMR spectrum of digested ZIF-408.

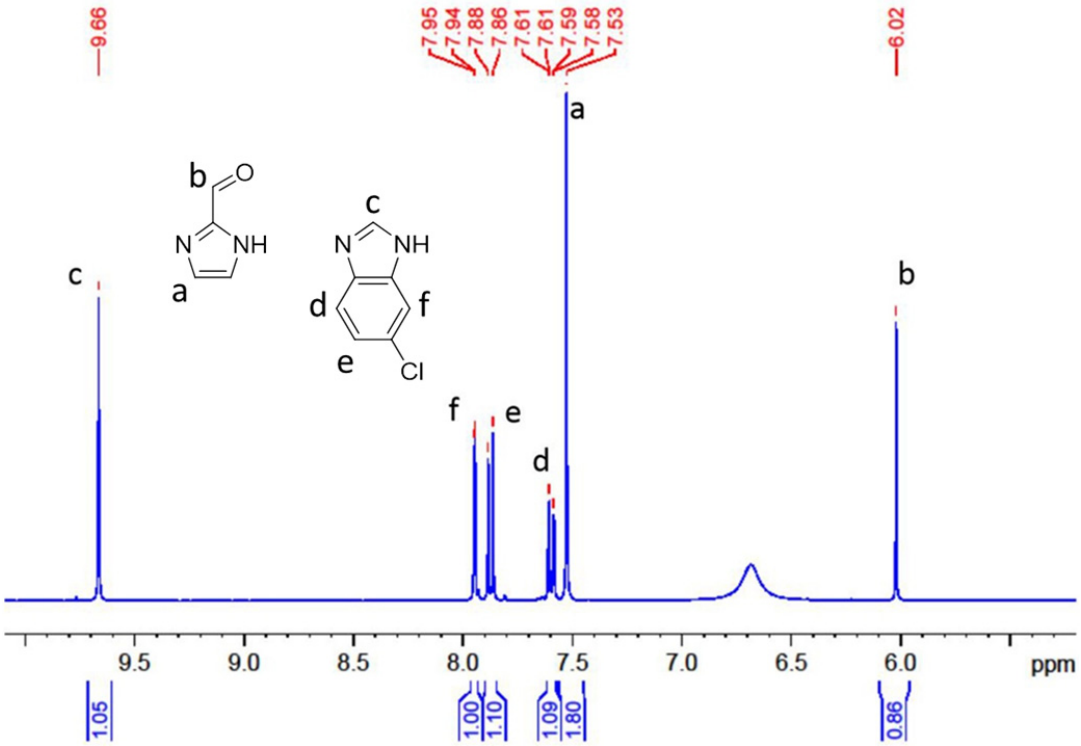

Figure 2.8 ^{1}H-NMR spectrum of digested ZIF-410.

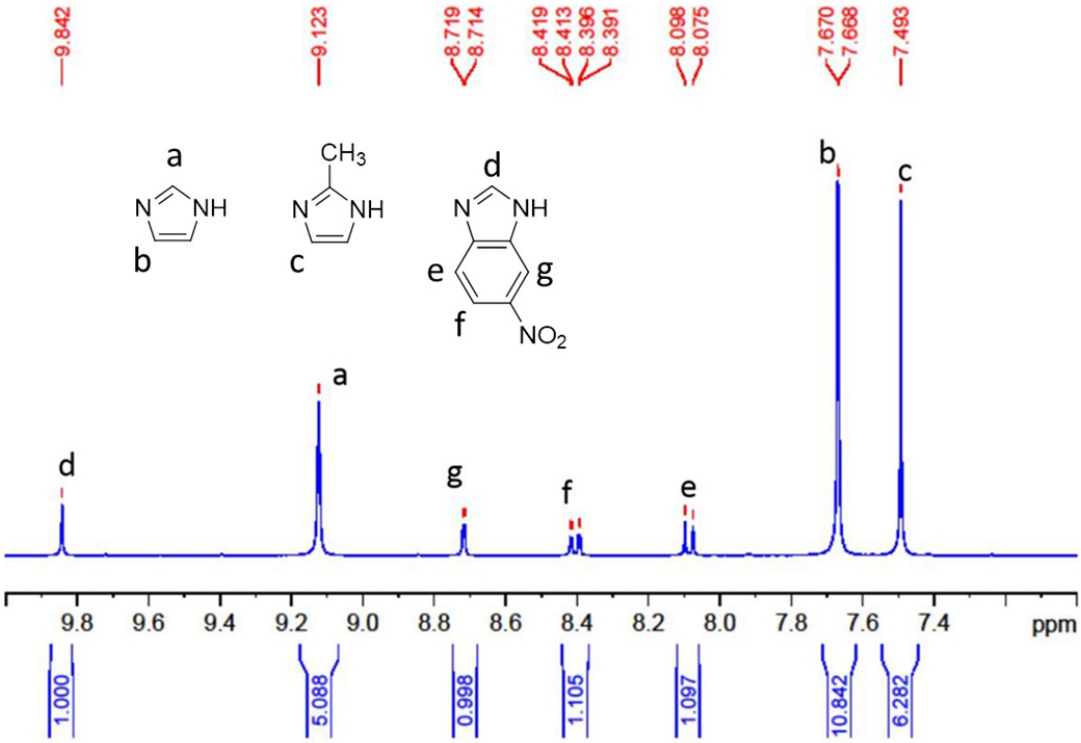

Figure 2.9 ^{1}H-NMR spectrum of digested ZIF-486.

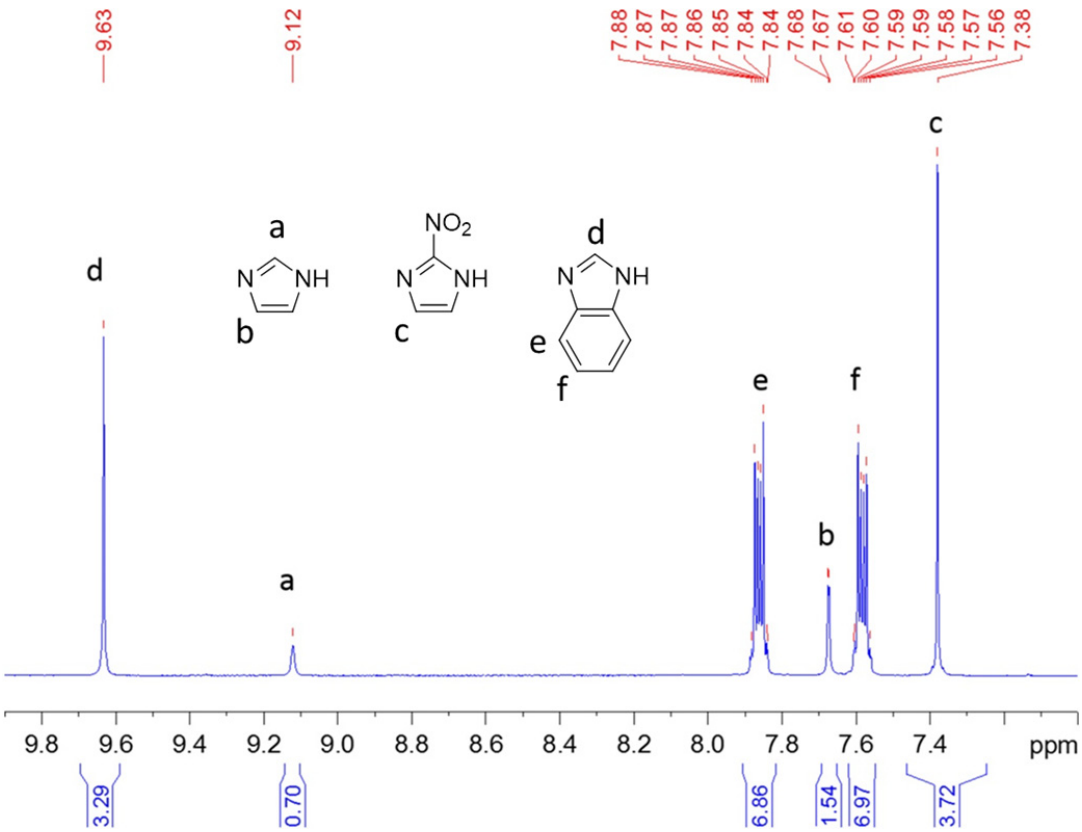

Figure 2.10 ^{1}H-NMR spectrum of digested ZIF-412.

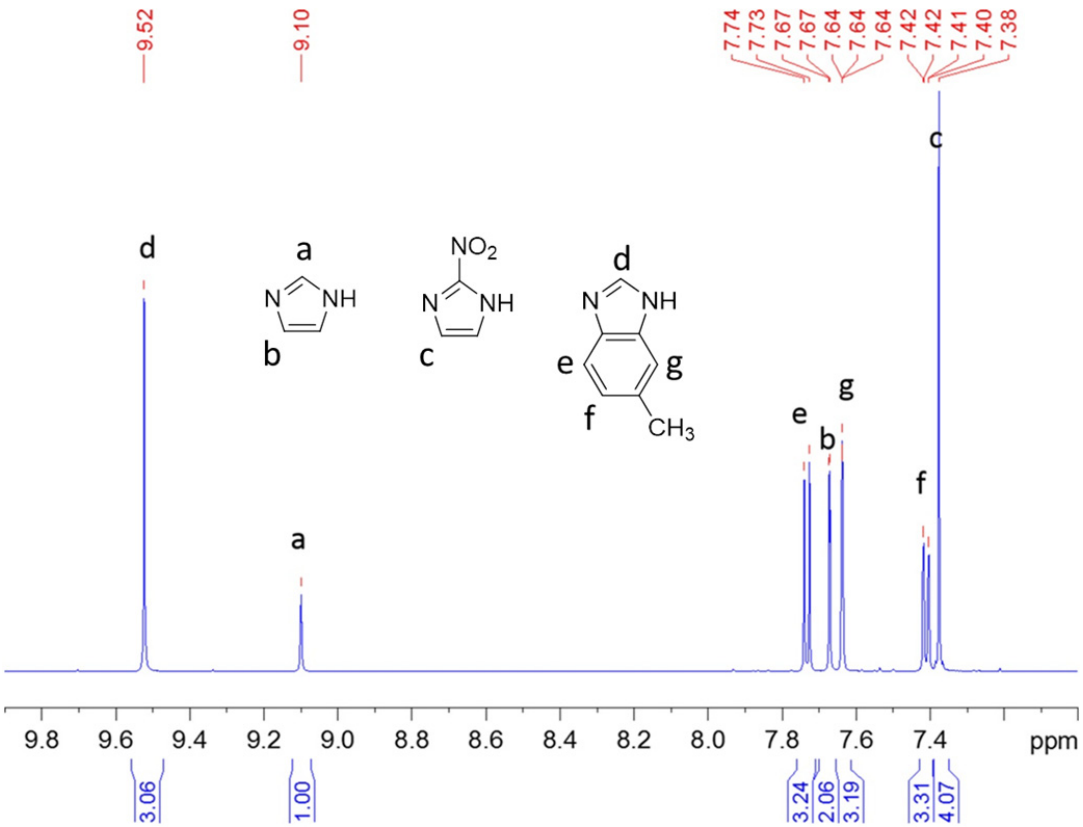

Figure 2.11 ^{1}H-NMR spectrum of digested ZIF-413.

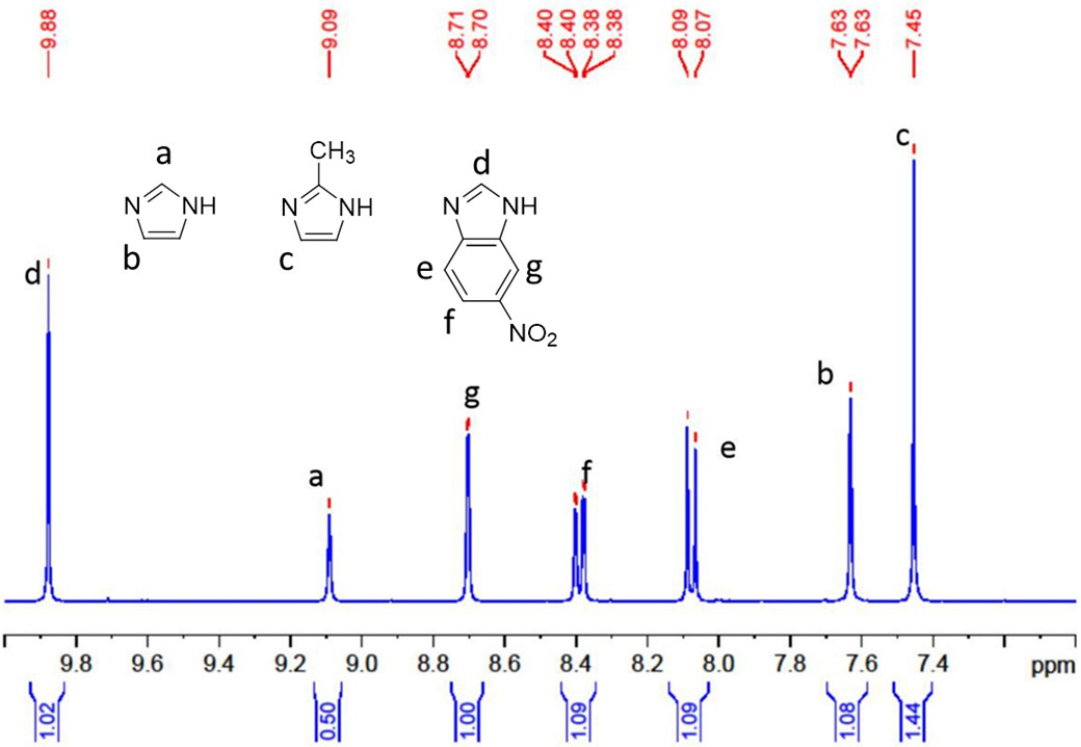

Figure 2.12 ^{1}H-NMR spectrum of digested ZIF-414.

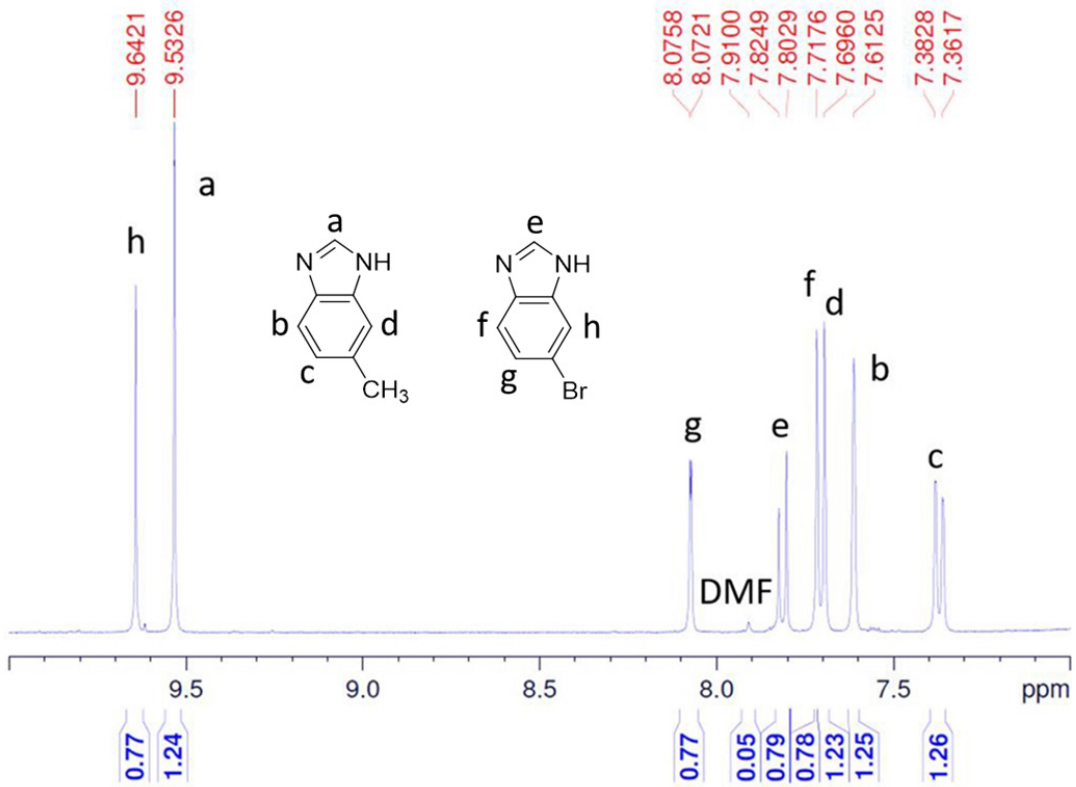

Figure 2.13 ^{1}H-NMR spectrum of digested ZIF-516.

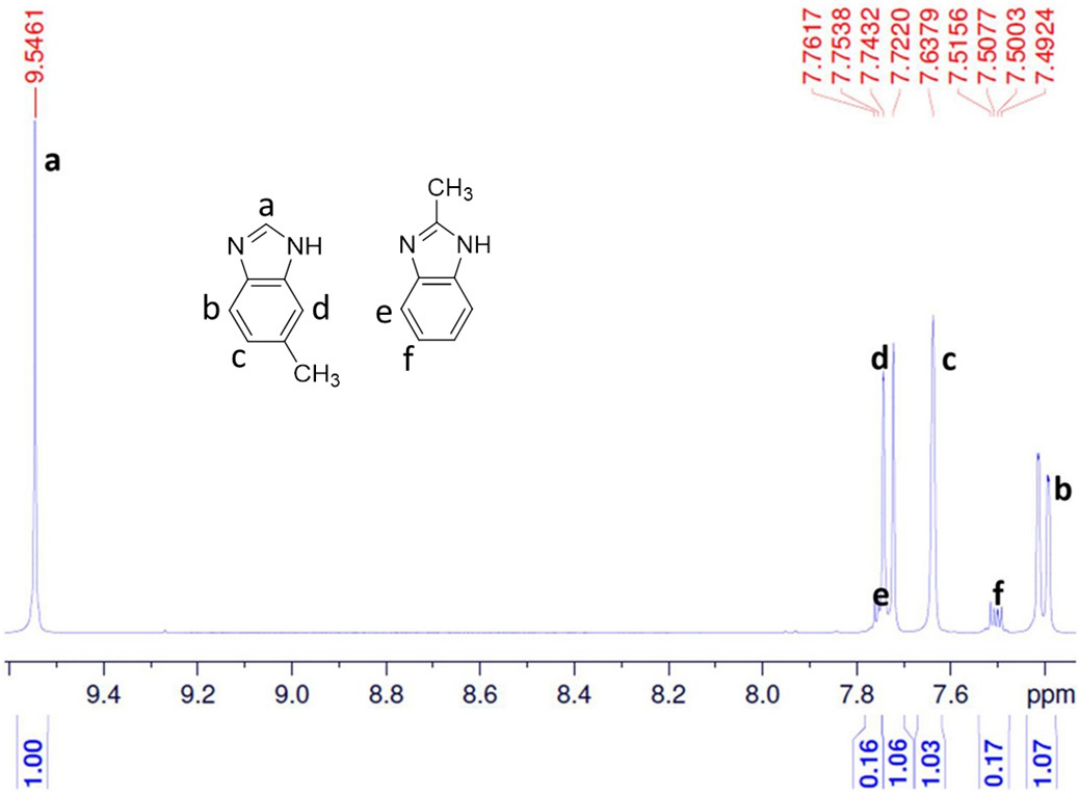

Figure 2.14 ^{1}H-NMR spectrum of digested ZIF-586.

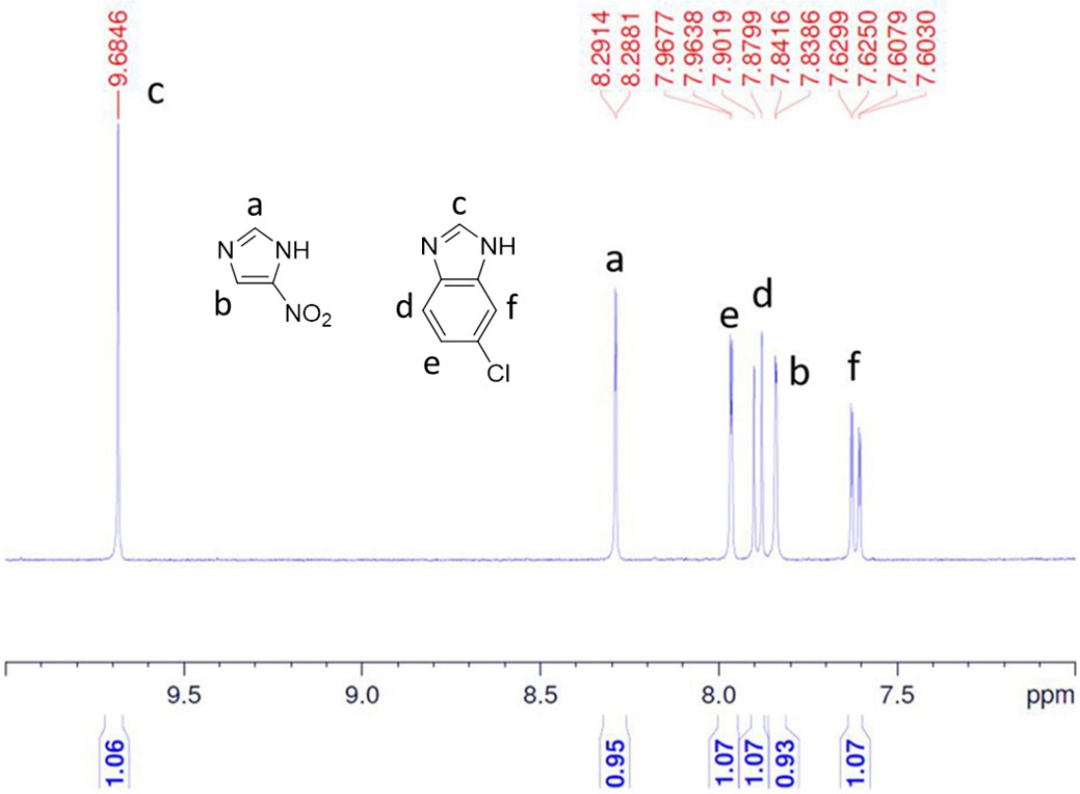

Figure 2.15 ^{1}H-NMR spectrum of digested ZIF-615.

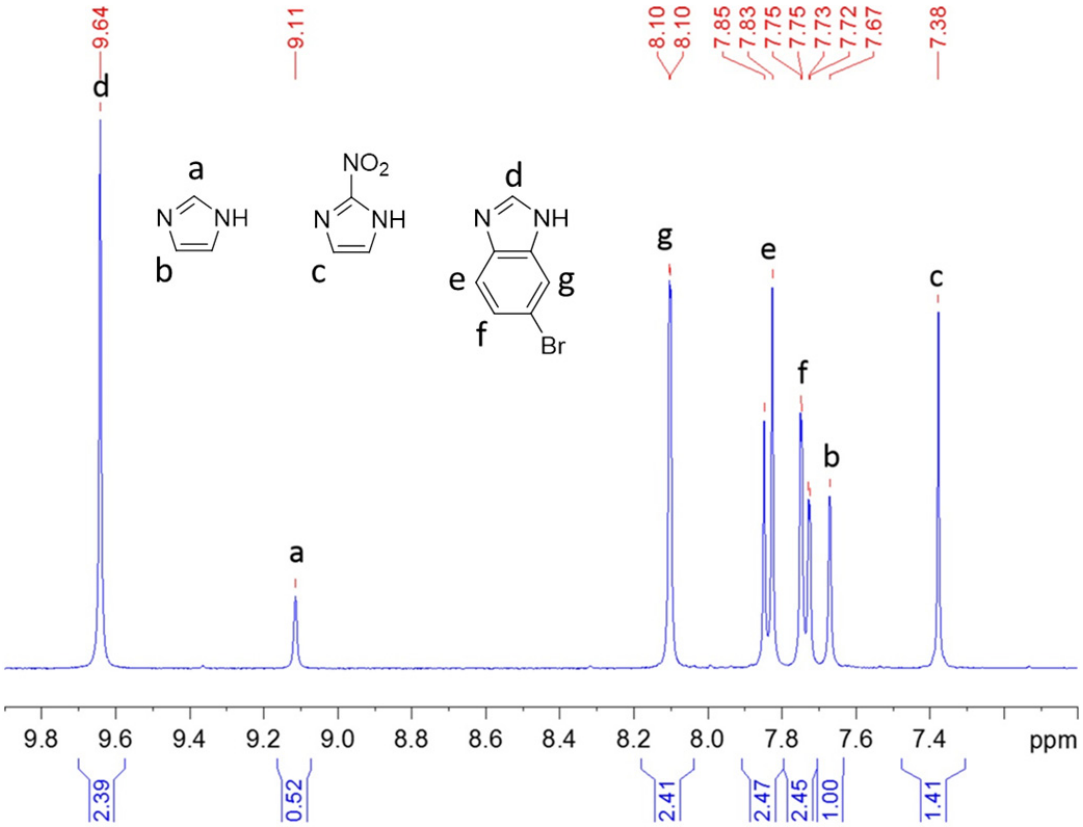

Figure 2.16 ^{1}H-NMR spectrum of digested ZIF-725.

Single-crystal X-ray diffraction. Single crystal X-ray diffraction data was collected using a combination of synchrotron radiation on beamline 11.3.1 and beamline 5.0.2 at the Advanced Light Source (ALS) at Lawrence Berkeley National Lab (LBNL), beamline 17U1 at Synchrotron Radiation Facility (SSRF) in Shanghai, China, a Bruker D8-Venture diffractometer and a Bruker MicroSTAR-H APEX II diffractometer in College of Chemistry, UC Berkeley (CheXray). Single crystal X-ray diffraction (SXRD) data for all ZIFs were obtained on as-synthesized crystals. Data for **ZIF-303**, **360**, **365**, **486**, **412**, **413**, **414**, **516**, and **725** were collected at beamline 11.3.1 of the ALS at LBNL, equipped with a Bruker Photon 100 CMOS area detector using synchrotron radiation (10-17 KeV); data for **ZIF-615** was collected at beamline 5.0.2 of the ALS at LBNL with a PILATUS3 S 6M detector at 0.89990 Å; data for **ZIF-408** and **586** were collected at beamline BL17U1 at SSRF, data for **ZIF-386** and **410** were collected on a Bruker MicroStart diffractometer equipped with a CCD area detector using rotating-anode Cu Kα radiation (λ = 1.54184 Å); data for **ZIF-376** was collected on a Bruker D8 Venture diffractometer equipped with a CMOS area detector using micro-focus Cu Kα radiation (λ = 1.54184 Å).

The resolution obtained for all samples was limited to varying degrees due to inherent disorder in the crystals. Data from NMR and elemental analysis were used as a starting point for the occupancies of functionalized imidazolates. For all structures except for **ZIF-516** and **-615**, all non-hydrogen atoms, in particular, the positions of functional groups on the imidazole rings, were located using the difference map during refinement. Typically, the restraints and constraints used on the refined model include rigid group restraints such as restraining phenyl and imidazolate rings to be planar with the appropriate distances applied from other known structure models, and rigid-bond restraints which are derived from a sound

chemical basis.[15] In the case of the two exceptions, the coordinates of the zinc atoms were first located, then rigid body refinements of unfunctionalized imidazoles were first performed to improve phasing. The functional group positions were located using the difference map before being incorporated into the imidazolate rigid body. This process was iterated several times to ensure all functional groups were correctly located. See the individual description for each ZIF and their corresponding CIFs for further details. Samples were mounted on MiTeGen® kapton loops and placed in a 100(2) K nitrogen cold stream unless otherwise specified.

In all cases except ZIF-615, the data were processed with the Bruker APEX2 software package,[16-17] integrated using SAINT v8.34A and corrected for the absorption by SADABS 2014/4 routines (no correction was made for extinction or decay). **ZIF-303** was processed as a two-domain twin using TWINABS. The structures were solved by intrinsic phasing (SHELXT) and refined by full-matrix least squares on F^2 (SHELXL-2014). Data reduction for **ZIF-615** was performed using the CrysAlisPro program[18] with a multiscan absorption correction using the ABSSCALE program incorporated in the software, and treated as a two-domain twin. All non-hydrogen atoms were refined anisotropically except for **ZIF-516** and **-615**, for which the low resolution precluded such treatment for non-zinc atoms. Hydrogen atoms were geometrically calculated and refined as riding atoms. In all structures, highly disordered guest molecules occupying the cavities of the structure, which could not be modeled and so were accounted for using solvent masking using the Olex2 software package,[19-20] except for **ZIF-303** and **ZIF-615** where SQUEEZE in PLATON's software package was used.[21]

Table 2.1 Crystal data and structure determination for **ZIF-303** (**CHA**)

Compound	**ZIF-303**
Chemical formula	$C_{7.50}H_4Cl_{0.50}N_{4.25}O_{0.50}Zn$
Formula mass	244.74
Crystal system	trigonal
Space group	$R\bar{3}$
λ (Å)	0.7749(1)
a (Å)	26.9457(15)
c (Å)	26.763(2)
Z	36
V (Å^3)	16828(2)
Temperature (K)	298(2)
Size /mm^3	0.150 × 0.100 × 0.100
Density (g/cm^{-3})	0.869
Measured reflections	2560
Unique reflections	2560
Parameters	284
Restraints	283
R_{int}	0.1093
θ range (°)	2.08-18.34
R_1, wR_2	0.1247, 0.4031
S (GOF)	1.189
Max/min res. dens. (e/Å^3)	0.85/-0.62

$^aR_1 = \Sigma||F_o| - |F_c||/\Sigma|F_o|$; $^bwR_2 = [\Sigma w(F_o^2 - F_c^2)^2/\Sigma w(F_o^2)^2]^{1/2}$; $^cS = [\Sigma w(F_o^2 - F_c^2)^2/(N_{ref} - N_{par})]^{1/2}$.

Table 2.2 Crystal data and structure determination for **ZIF-360** (**KFI**)

Compound	**ZIF-360**
Chemical formula	$C_{18}H_{13}N_{10}O_4Zn_2$
Formula mass	1217.24
Crystal system	cubic
Space group	$Im\bar{3}m$
λ (Å)	1.2399(1)
a (Å)	35.943(3)
Z	48
V (Å^3)	46436(13)
Temperature (K)	100(2)
Size /mm^3	0.150 × 0.130 × 0.120
Density (g/cm^{-3})	0.968
Measured reflections	64698
Unique reflections	1409
Parameters	199
Restraints	75
R_{int}	0.0919
θ range (°)	2.42-31.20
R_1, wR_2	0.0597, 0.1875
S (GOF)	1.095
Max/min res. dens. (e/Å^3)	1.37/-0.31

$^aR_1 = \Sigma||F_o| - |F_c||/\Sigma|F_o|$; $^bwR_2 = [\Sigma w(F_o^2 - F_c^2)^2/\Sigma w(F_o^2)^2]^{1/2}$; $^cS = [\Sigma w(F_o^2 - F_c^2)^2/(N_{ref} - N_{par})]^{1/2}$.

Table 2.3 Crystal data and structure determination for **ZIF-365** (**KFI**)

Compound	**ZIF-365**
Chemical formula	$C_{20}H_{12}Cl_2N_9O_2Zn_2$
Formula mass	612.054
Crystal system	cubic
Space group	$Im\bar{3}m$
λ (Å)	1.2399(1)
a (Å)	35.763(4)
Z	48
V (Å^3)	45739(13)
Temperature (K)	100(2)
Size /mm^3	0.140 × 0.130 × 0.110
Density (g/cm^{-3})	1.067
Measured reflections	61149
Unique reflections	1297
Parameters	203
Restraints	51
R_{int}	0.0688
θ range (°)	2.43-30.36
R_1, wR_2	0.0624, 0.2004
S (GOF)	1.110
Max/min res. dens. (e/Å^3)	0.54/-0.29

$^a R_1 = \Sigma||F_o| - |F_c||/\Sigma|F_o|$; $^b wR_2 = [\Sigma w(F_o^2 - F_c^2)^2/\Sigma w(F_o^2)^2]^{1/2}$; $^c S = [\Sigma w(F_o^2 - F_c^2)^2/(N_{ref} - N_{par})]^{1/2}$.

Table 2.4 Crystal data and structure determination for **ZIF-376** (**LTA**)

Compound	**ZIF-376**
Chemical formula	$C_{3.625}H_{2.875}N_{2.125}O_{0.25}Zn$
Formula mass	225.78
Crystal system	cubic
Space group	$Pm\bar{3}m$
λ (Å)	1.54178
a (Å)	22.688(3)
Z	24
V (Å^3)	11679(4)
Temperature (K)	100(2)
Size /mm^3	0.100 × 0.100 × 0.100
Density (g/cm^{-3})	0.770
Measured reflections	7779
Unique reflections	765
Parameters	132
Restraints	148
R_{int}	0.0634
θ range (°)	3.37-39.94
R_1, wR_2	0.1189, 0.3415
S (GOF)	1.092
Max/min res. dens. (e/Å^3)	0.64/-0.38

$^a R_1 = \Sigma||F_o| - |F_c||/\Sigma|F_o|$; $^b wR_2 = [\Sigma w(F_o^2 - F_c^2)^2/\Sigma w(F_o^2)^2]^{1/2}$; $^c S = [\Sigma w(F_o^2 - F_c^2)^2/(N_{ref} - N_{par})]^{1/2}$.

Table 2.5 Crystal data and structure determination for **ZIF-386** (**AFX**)

Compound	**ZIF-386**
Chemical formula	$C_{36}H_{23}N_{22}O_{12}Zn_4$
Formula mass	1217.24
Crystal system	hexagonal
Space group	$P6_3/mmc$
λ (Å)	1.54178
a (Å)	27.1315(7)
c (Å)	34.4505(12)
Z	12
V (Å^3)	21962.1(14)
Temperature (K)	100(2)
Size /mm^3	0.200 × 0.200 × 0.080
Density (g/cm^{-3})	1.104
Measured reflections	78188
Unique reflections	2908
Parameters	380
Restraints	95
R_{int}	0.0505
θ range (°)	1.88-43.00
R_1, wR_2	0.0792, 0.2850
S (GOF)	1.143
Max/min res. dens. (e/Å^3)	0.79/-0.39

[a] $R_1 = \Sigma||F_o| - |F_c||/\Sigma|F_o|$; [b] $wR_2 = [\Sigma w(F_o^2 - F_c^2)^2/\Sigma w(F_o^2)^2]^{1/2}$; [c] $S = [\Sigma w(F_o^2 - F_c^2)^2/(N_{ref} - N_{par})]^{1/2}$.

Table 2.6 Crystal data and structure determination for **ZIF-408** (**moz**)

Compound	**ZIF-408**
Chemical formula	$C_{273}H_{149}Cl_{39}N_{78}O_2Zn_{20}$
Formula mass	7243
Crystal system	Cubic
Space group	$Im\bar{3}$
λ (Å)	0.72929(1)
a (Å)	70.593(8)
Z	24
V (Å^3)	351791(122)
Temperature (K)	100(2)
Size /mm^3	0.04 × 0.06 × 0.08
Density (g/cm^{-3})	0.821
Measured reflections	26180
Unique reflections	14490
Parameters	453
Restraints	87
R_{int}	0.0141
θ range (°)	0.7-16.3
R_1, wR_2	0.1863, 0.5573
S (GOF)	1.697
Max/min res. dens. (e/Å^3)	0.99/-0.70

$^a R_1 = \Sigma||F_o| - |F_c||/\Sigma|F_o|$; $^b wR_2 = [\Sigma w(F_o^2 - F_c^2)^2/\Sigma w(F_o^2)^2]^{1/2}$; $^c S = [\Sigma w(F_o^2 - F_c^2)^2/(N_{ref} - N_{par})]^{1/2}$.

Table 2.7 Crystal data and structure determination for **ZIF-410** (**GME**)

Compound	**ZIF-410**
Chemical formula	$C_{11}H_7ClN_4OZn_3$
Formula mass	312.03
Crystal system	hexagonal
Space group	$P6_3/mmc$
λ (Å)	1.54178
a (Å)	25.9453(6)
c (Å)	19.5015(6)
Z	24
V (Å^3)	11368.8(6)
Temperature (K)	100(2)
Size /mm^3	0.120 × 0.085 × 0.080
Density (g/cm^{-3})	1.094
Measured reflections	19478
Unique reflections	1335
Parameters	189
Restraints	35
R_{int}	0.0502
θ range (°)	1.97-40.06
R_1, wR_2	0.0692, 0.2506
S (GOF)	1.138
Max/min res. dens. (e/Å^3)	0.63/-0.28

$^a R_1 = \Sigma||F_o| - |F_c||/\Sigma|F_o|$; $^b wR_2 = [\Sigma w(F_o^2 - F_c^2)^2/\Sigma w(F_o^2)^2]^{1/2}$; $^c S = [\Sigma w(F_o^2 - F_c^2)^2/(N_{ref} - N_{par})]^{1/2}$.

Table 2.8 Crystal data and structure determination for **ZIF-486** (**GME**)

Compound	**ZIF-486**
Chemical formula	$C_{7.50}H_{7.40}N_{4.20}O_{0.40}Zn$
Formula mass	228.15
Crystal system	hexagonal
Space group	*P6₃/mmc*
λ (Å)	0.7749(1)
a (Å)	27.0807(16)
c (Å)	16.7619(16)
Z	24
V (Å^3)	10645.7(16)
Temperature (K)	100(2)
Size /mm^3	0.200 × 0.200 × 0.100
Density (g/cm^{-3})	0.854
Measured reflections	15269
Unique reflections	1469
Parameters	132
Restraints	136
R_{int}	0.0534
θ range (°)	2.31-20.04
R_1, wR_2	0.1153, 0.3525
S (GOF)	1.020
Max/min res. dens. (e/Å^3)	1.09/-0.52

[a] $R_1 = \Sigma||F_o| - |F_c||/\Sigma|F_o|$; [b] $wR_2 = [\Sigma w(F_o^2 - F_c^2)^2/\Sigma w(F_o^2)^2]^{1/2}$; [c] $S = [\Sigma w(F_o^2 - F_c^2)^2/(N_{ref} - N_{par})]^{1/2}$.

Table 2.9 Crystal data and structure determination for **ZIF-412** (**ucb**)

Compound	**ZIF-412**
Chemical formula	$C_{31.6}H_{22.95}N_{13.85}O_{3.7}Zn_3$
Formula mass	852.03
Crystal system	cubic
Space group	$Fm\bar{3}m$
λ (Å)	0.8265(1)
a (Å)	72.205(2)
Z	192
V (Å^3)	376445(31)
Temperature (K)	100(2)
Size /mm^3	0.100 × 0.120 × 0.130
Density (g/cm^{-3})	0.722
Measured reflections	270972
Unique reflections	4845
Parameters	516
Restraints	137
R_{int}	0.1418
θ range (°)	1.70-19.30
R_1, wR_2	0.0434, 0.1503
S (GOF)	1.081
Max/min res. dens. (e/Å^3)	0.32/-0.29

$^aR_1 = \Sigma||F_o| - |F_c||/\Sigma|F_o|$; $^bwR_2 = [\Sigma w(F_o^2 - F_c^2)^2/\Sigma w(F_o^2)^2]^{1/2}$; $^cS = [\Sigma w(F_o^2 - F_c^2)^2/(N_{ref} - N_{par})]^{1/2}$.

Table 2.10 Crystal data and structure determination for **ZIF-413** (**ucb**)

Compound	**ZIF-413**
Chemical formula	$C_{33.5}H_{26.49}N_{13.81}O_{3.63}Zn_3$
Formula mass	876.74
Crystal system	cubic
Space group	$Fm\bar{3}m$
λ (Å)	1.2399(1)
a (Å)	72.3673(14)
Z	192
V (Å^3)	378989(22)
Temperature (K)	100(2)
Size /mm^3	0.100 × 0.100 × 0.100
Density (g/cm^{-3})	0.737
Measured reflections	168049
Unique reflections	5478
Parameters	561
Restraints	362
R_{int}	0.0295
θ range (°)	1.96-31.06
R_1, wR_2	0.1032, 0.3434
S (GOF)	1.050
Max/min res. dens. (e/Å^3)	1.11/-0.32

$^a R_1 = \Sigma||F_o| - |F_c||/\Sigma|F_o|$; $^b wR_2 = [\Sigma w(F_o^2 - F_c^2)^2/\Sigma w(F_o^2)^2]^{1/2}$; $^c S = [\Sigma w(F_o^2 - F_c^2)^2/(N_{ref} - N_{par})]^{1/2}$.

Table 2.11 Crystal data and structure determination for **ZIF-414** (**ucb**)

Compound	**ZIF-414**
Chemical formula	$C_{29.08}H_{24.45}N_{14.30}O_{4.60}Zn_3$
Formula mass	843.95
Crystal system	cubic
Space group	$Fm\bar{3}m$
λ (Å)	0.7749(1)
a (Å)	72.2609(18)
Z	192
V (Å^3)	377320(28)
Temperature (K)	100(2)
Size /mm^3	0.090 × 0.090 × 0.090
Density (g/cm^{-3})	0.713
Measured reflections	285177
Unique reflections	4062
Parameters	600
Restraints	500
R_{int}	0.0928
θ range (°)	2.04-16.93
R_1, wR_2	0.0932, 0.2491
S (GOF)	1.157
Max/min res. dens. (e/Å^3)	0.37/-0.29

$^a R_1 = \Sigma||F_o| - |F_c||/\Sigma|F_o|$; $^b wR_2 = [\Sigma w(F_o^2 - F_c^2)^2/\Sigma w(F_o^2)^2]^{1/2}$; $^c S = [\Sigma w(F_o^2 - F_c^2)^2/(N_{ref} - N_{par})]^{1/2}$.

Table 2.12 Crystal data and structure determination for **ZIF-516**

Compound	**ZIF-516**
Chemical formula	$C_{195}H_{77}Br_{13}N_{52}Zn_{13}$
Formula mass	5036.72
Crystal system	tetragonal
Space group	$P4_32_12$
λ (Å)	0.7749(1)
a (Å)	29.157(3)
c (Å)	69.955(9)
Z	8
V (Å^3)	59470(15)
Temperature (K)	100(2)
Size /mm^3	0.080 × 0.040 × 0.040
Density (g/cm^{-3})	1.125
Measured reflections	94423
Unique reflections	13193
Parameters	609
Restraints	271
R_{int}	0.1308
θ range (°)	1.95-16.95
R_1, wR_2	0.0972, 0.2730
S (GOF)	1.047
Flack parameter	0.498(6)*
Max/min res. dens. (e/Å^3)	0.61/-0.65

$^aR_1 = \Sigma||F_o| - |F_c||/\Sigma|F_o|$; $^bwR_2 = [\Sigma w(F_o^2 - F_c^2)^2/\Sigma w(F_o^2)^2]^{1/2}$; $^cS = [\Sigma w(F_o^2 - F_c^2)^2/(N_{ref} - N_{par})]^{1/2}$.

*Note that the low resolution precludes determining the framework chirality.

Table 2.13 Crystal data and structure determination for **ZIF-586** (**ykh**)

Compound	**ZIF-586**
Chemical formula	C_{304} N_{104} Zn_{26}
Formula mass	6807.70
Crystal system	tetragonal
Space group	*P4₂/ncm*
λ (Å)	0.72929(1)
a (Å)	29.744(4)
c (Å)	34.550(7)
Z	4
V (Å^3)	30567(11)
Temperature (K)	100(2)
Size /mm^3	0. 03 × 0. 03 × 0. 01
Density (g/cm^{-3})	0.846
Measured reflections	2255
Unique reflections	2255
Parameters	161
Restraints	185
R_{int}	0.0496
θ range (°)	1.399-13.605
R_1, wR_2	0.2256, 0.5573
S (GOF)	1.021
Max/min res. dens. (e/Å^3)	0.56/-0.40

$^a R_1 = \Sigma||F_o| - |F_c||/\Sigma|F_o|$; $^b wR_2 = [\Sigma w(F_o^2 - F_c^2)^2/\Sigma w(F_o^2)^2]^{1/2}$; $^c S = [\Sigma w(F_o^2 - F_c^2)^2/(N_{ref} - N_{par})]^{1/2}$.

Table 2.14 Crystal data and structure determination for **ZIF-615** (**gcc**)

Compound	**ZIF-615**
Chemical formula	$C_{20}H_{11}Cl_2N_{10}O_4Zn_2$
Formula mass	657.03
Crystal system	hexagonal
Space group	*P6₃/mmc*
λ (Å)	0.8999(1)
a (Å)	31.731(6)
c (Å)	28.412(6)
Z	12
V (Å^3)	24774(11)
Temperature (K)	100(2)
Size /mm^3	0.050 × 0.015 × 0.015
Density (g/cm^{-3})	1.058
Measured reflections	15250
Unique reflections	4924
Parameters	95
Restraints	28
R_{int}	0.208
θ range (°)	1.63-18.74
R_1, wR_2	0.1933, 0.5500
S (GOF)	1.084
Max/min res. dens. (e/Å^3)	0.47/-0.57

$^aR_1 = \Sigma||F_o| - |F_c||/\Sigma|F_o|$; $^bwR_2 = [\Sigma w(F_o^2 - F_c^2)^2/\Sigma w(F_o^2)^2]^{1/2}$; $^cS = [\Sigma w(F_o^2 - F_c^2)^2/(N_{ref} - N_{par})]^{1/2}$.

Table 2.15 Crystal data and structure determination for **ZIF-725** (**bam**)

Compound	**ZIF-725**
Chemical formula	$C_{22}H_{13.50}Br_{2.50}N_9O_2Zn_2$
Formula mass	766.43
Crystal system	hexagonal
Space group	*P*6/*mmm*
λ (Å)	1.0332(1)
a (Å)	42.586(3)
c (Å)	19.8692(13)
Z	24
V (Å^3)	31206(4)
Temperature (K)	100(2)
Size /mm^3	0.100 × 0.100 × 0.080
Density (g/cm^{-3})	0.979
Measured reflections	90065
Unique reflections	2411
Parameters	348
Restraints	473
R_{int}	0.2655
θ range (°)	2.12-21.97
R_1, wR_2	0.1621, 0.4377
S (GOF)	1.152
Max/min res. dens. (e/Å^3)	0.72/-0.57

$^a R_1 = \Sigma||F_o| - |F_c||/\Sigma|F_o|$; $^b wR_2 = [\Sigma w(F_o^2 - F_c^2)^2/\Sigma w(F_o^2)^2]^{1/2}$; $^c S = [\Sigma w(F_o^2 - F_c^2)^2/(N_{ref} - N_{par})]^{1/2}$.

Powder X-ray diffraction. Powder X-ray diffraction (PXRD) analysis were conducted on a Bruker D8 Advance diffractometer with Cu Kα radiation (λ = 1.54056 Å).

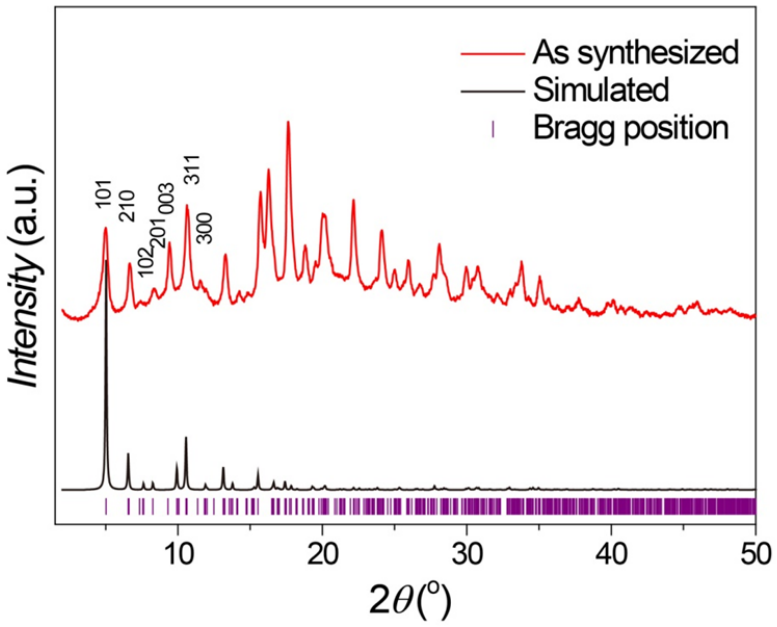

Figure 2.17 Comparison of the experimental PXRD patterns of ZIF-303: as-synthesized (red) and simulated pattern (black) from single crystal X-ray data. This sample is not activated, thus pattern for as-synthesized sample is provided here. The intensity difference and hump over a wide range of two-theta compared to simulated pattern is due to the inclusion of large amount of disordered solvent molecules.

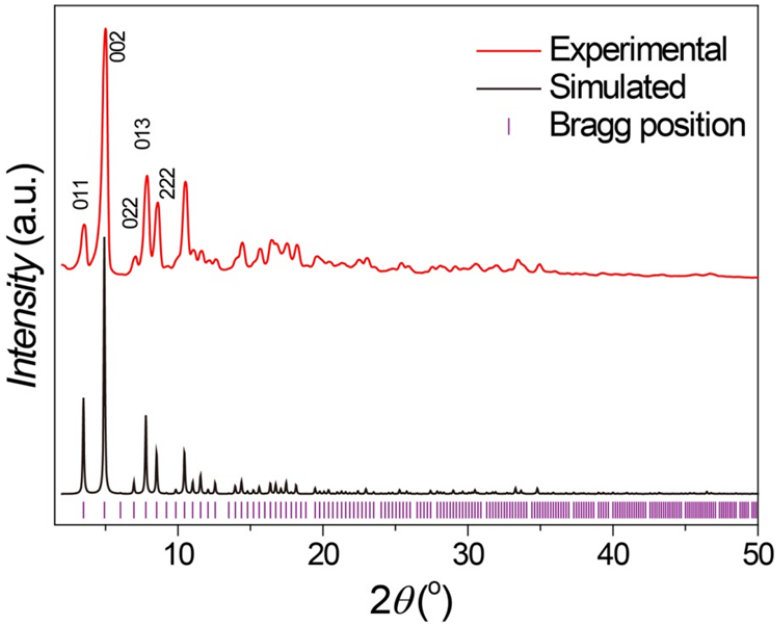

Figure 2.18 Comparison of the experimental PXRD patterns of ZIF-360: activated (red) and simulated pattern (black) from single crystal X-ray data.

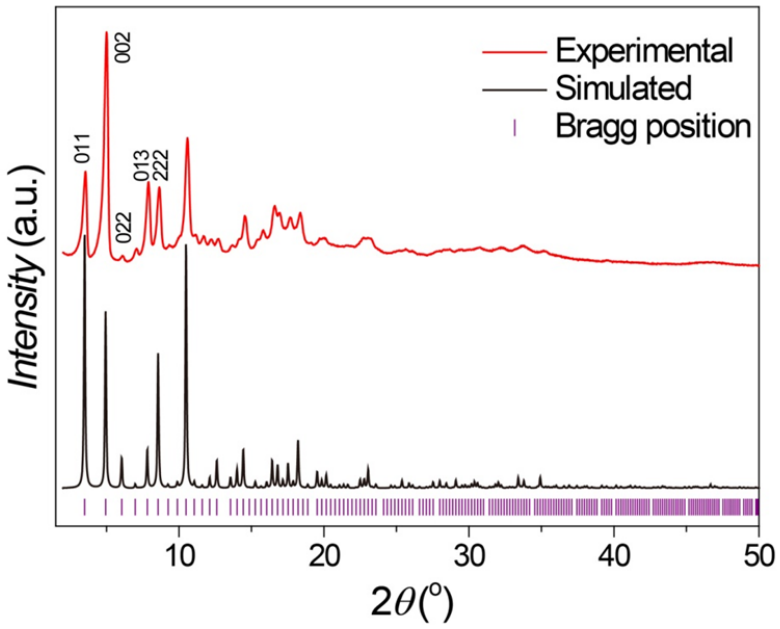

Figure 2.19 Comparison of the experimental PXRD patterns of ZIF-365: activated (red) and simulated pattern (black) from single crystal X-ray data.

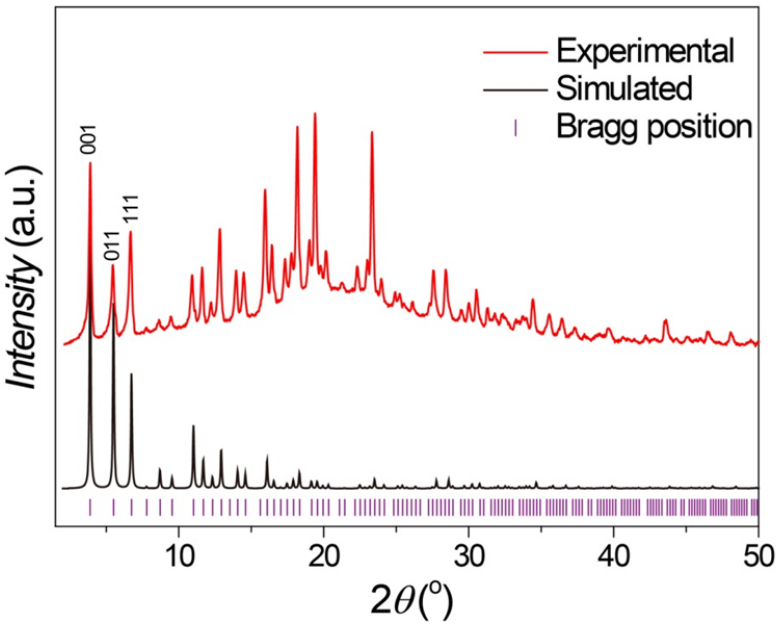

Figure 2.20 Comparison of the experimental PXRD patterns of ZIF-376: as-synthesized (red) and simulated pattern (black) from single crystal X-ray data. This sample is not activated, thus pattern for as-synthesized sample is provided here. The intensity difference and hump over a wide range of two-theta compared to simulated pattern is due to the inclusion of large amount of disordered solvent molecules.

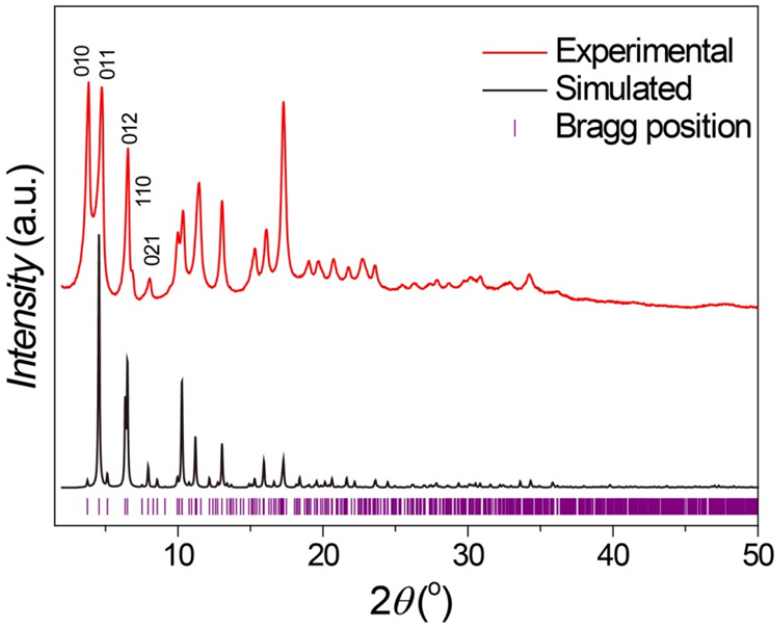

Figure 2.21 Comparison of the experimental PXRD patterns of ZIF-386: activated (red) and simulated pattern (black) from single crystal X-ray data.

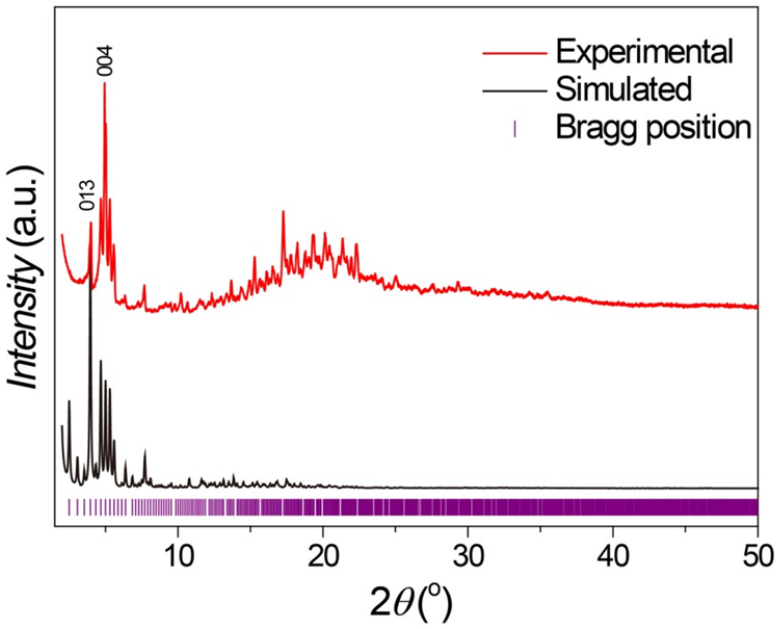

Figure 2.22 Comparison of the experimental PXRD patterns of ZIF-408: as-synthesized (red) and simulated pattern (black) from single crystal X-ray data. This sample is not activated, thus pattern for as-synthesized sample is provided here. The intensity difference and hump over a wide range of two-theta compared to simulated pattern is due to the inclusion of large amount of disordered solvent molecules.

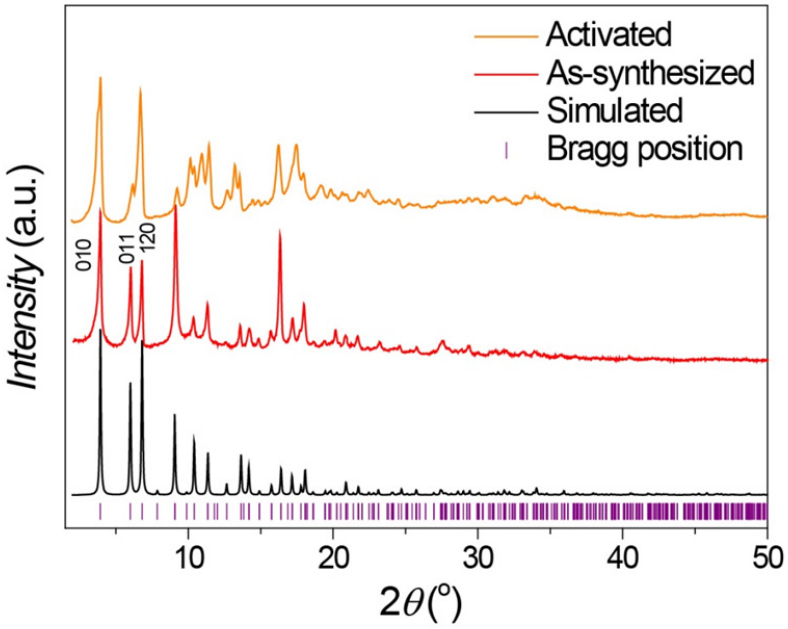

Figure 2.23 Comparison of the experimental PXRD patterns of ZIF-410: as-synthesized (red), activated (orange), and simulated pattern (black) from single crystal X-ray data. Activated pattern shows certain peak shift which might be attribute the slight rotation of the IM linkers along the axis between two Zn metals due to the large cavity available.

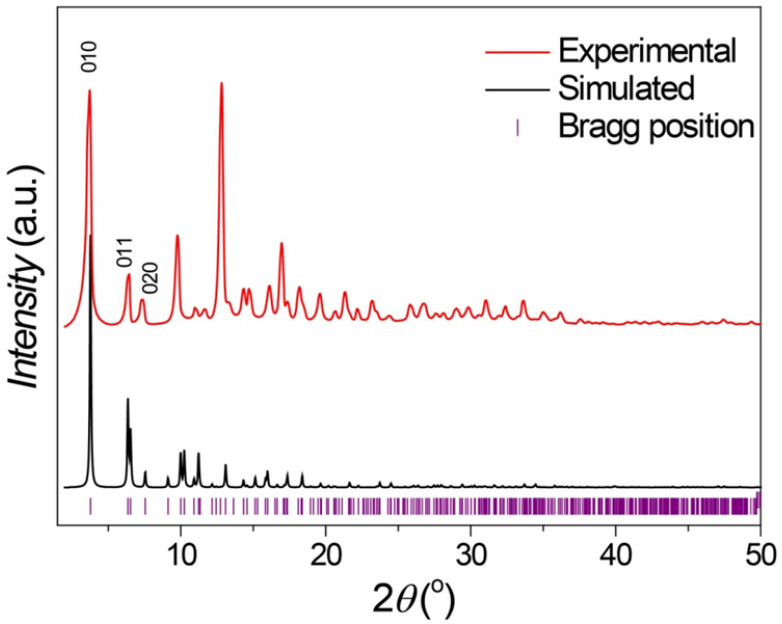

Figure 2.24 Comparison of the experimental PXRD patterns of ZIF-486: activated (red) and simulated pattern (black) from single crystal X-ray data.

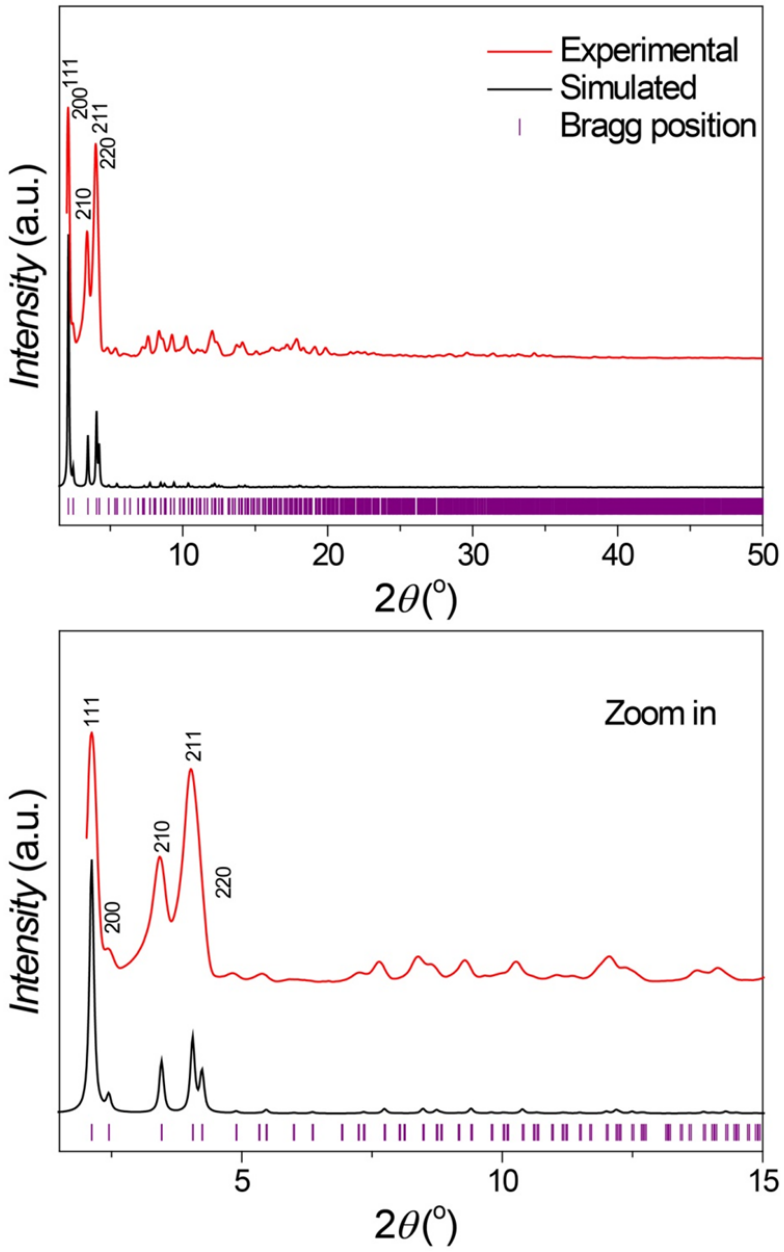

Figure 2.25 Comparison of the experimental PXRD patterns of ZIF-412: activated (red) and simulated pattern (black) from single crystal X-ray data (Full scale 1.5-50° and zoom in 1.5-15°).

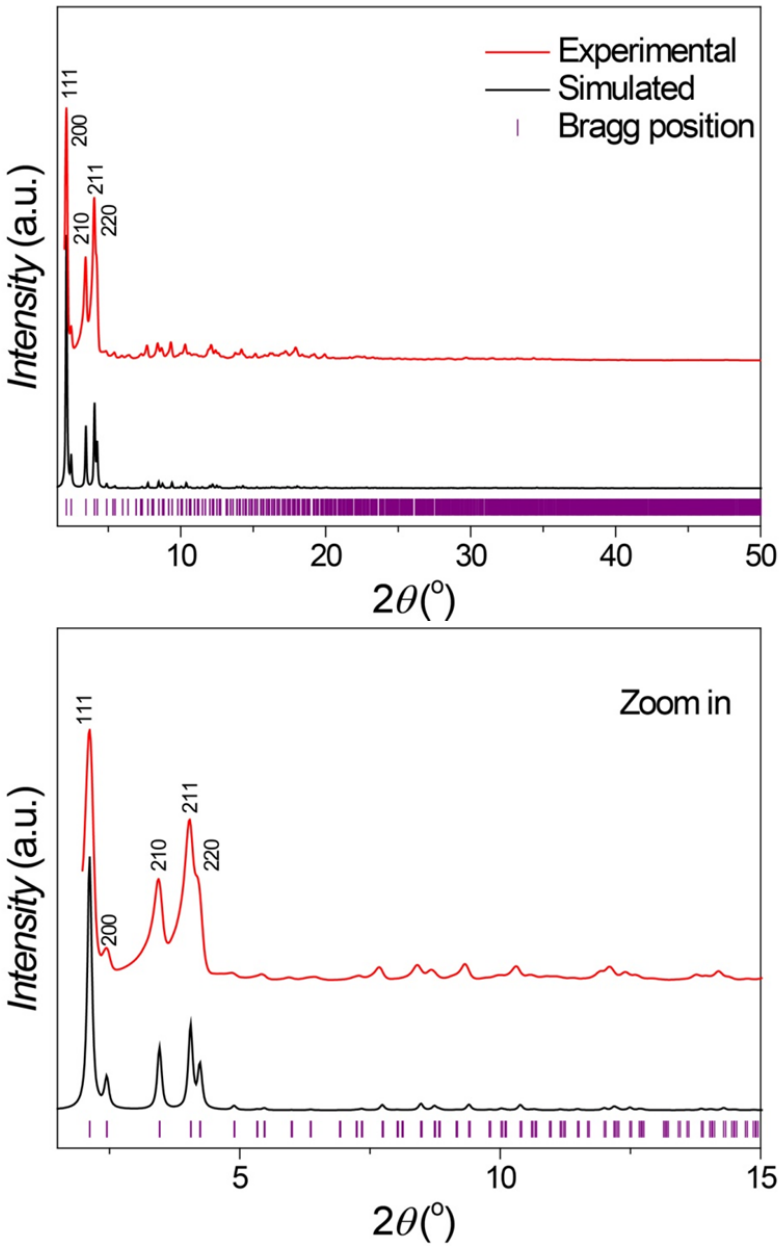

Figure 2.26 Comparison of the experimental PXRD patterns of ZIF-413: activated (red) and simulated pattern (black) from single crystal X-ray data (Full scale 1.5-50° and zoom in 1.5-15°).

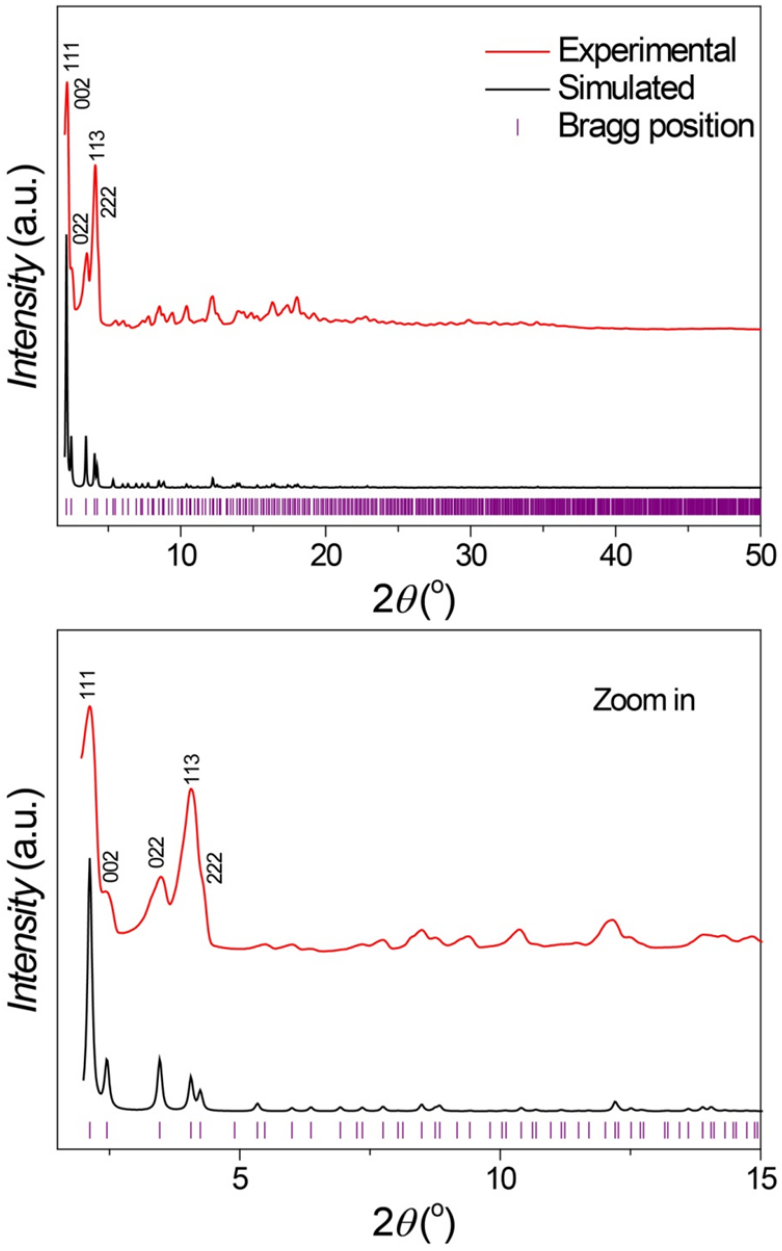

Figure 2.27 Comparison of the experimental PXRD patterns of ZIF-414: activated (red) and simulated pattern (black) from single crystal X-ray data (Full scale 1.5-50° and zoom in 1.5-15°).

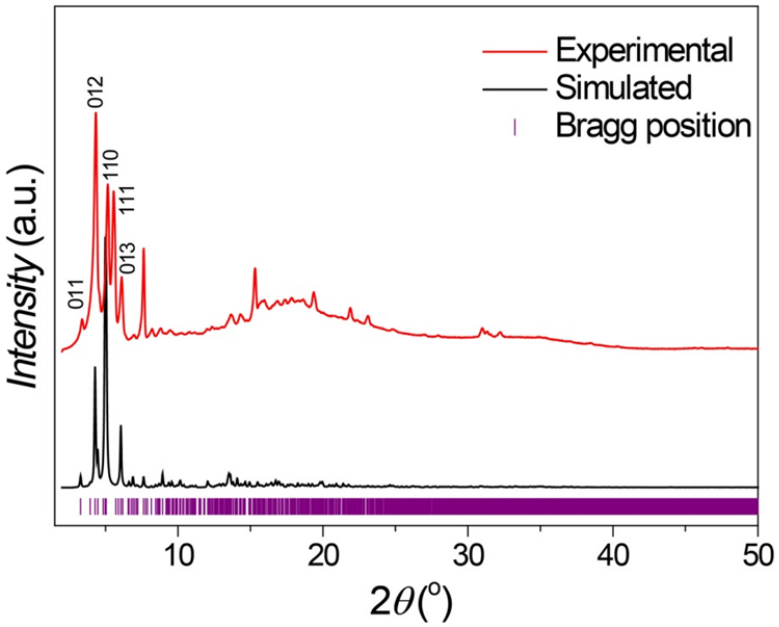

Figure 2.28 Comparison of the experimental PXRD patterns of ZIF-516: activated (red) and simulated pattern (black) from single crystal X-ray data. This ZIF still contains certain amount of solvent after activation as illustrated by its formula $Zn(bbIM)_{0.77}(mbIM)_{1.23}(DMF)_{0.05}$, leading to some intensity difference and hump over a range of two-theta.

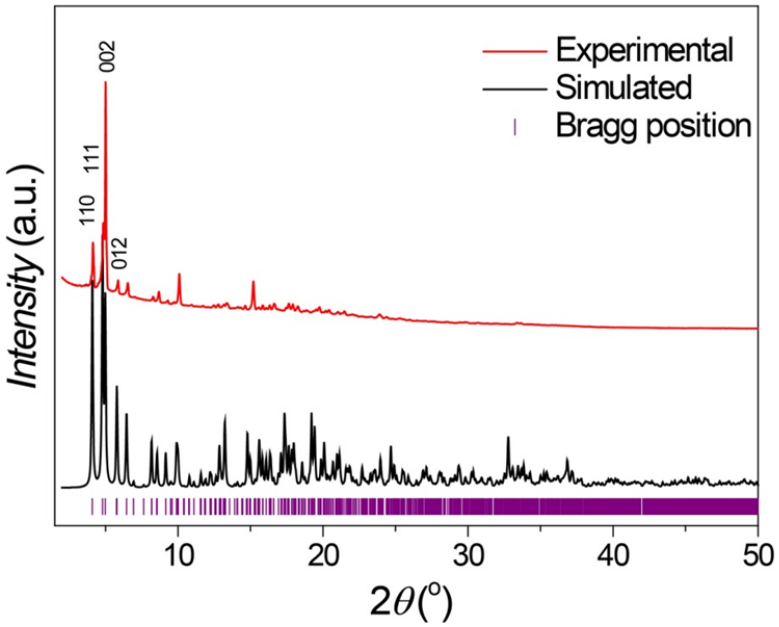

Figure 2.29 Comparison of the experimental PXRD patterns of ZIF-586: activated (red) and simulated pattern (black) from single crystal X-ray data.

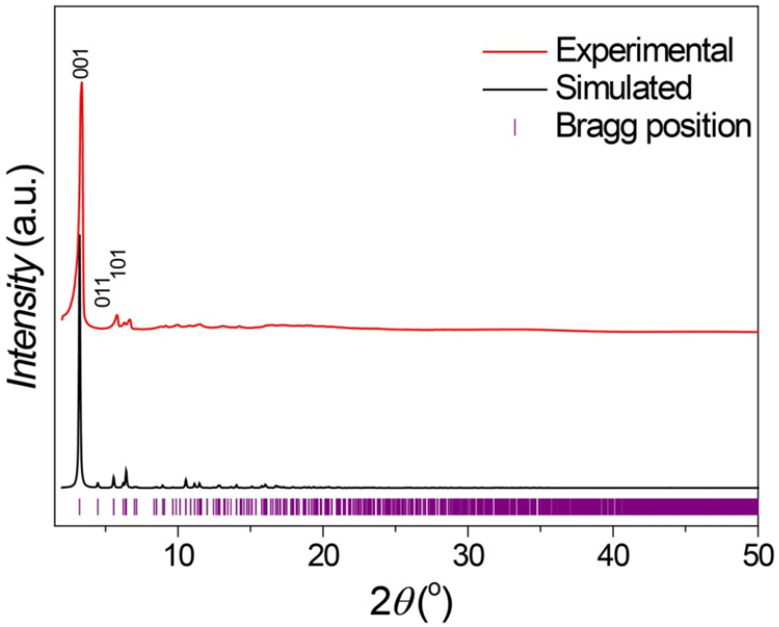

Figure 2.30 Comparison of the experimental PXRD patterns of ZIF-615: activated (red) and simulated pattern (black) from single crystal X-ray data.

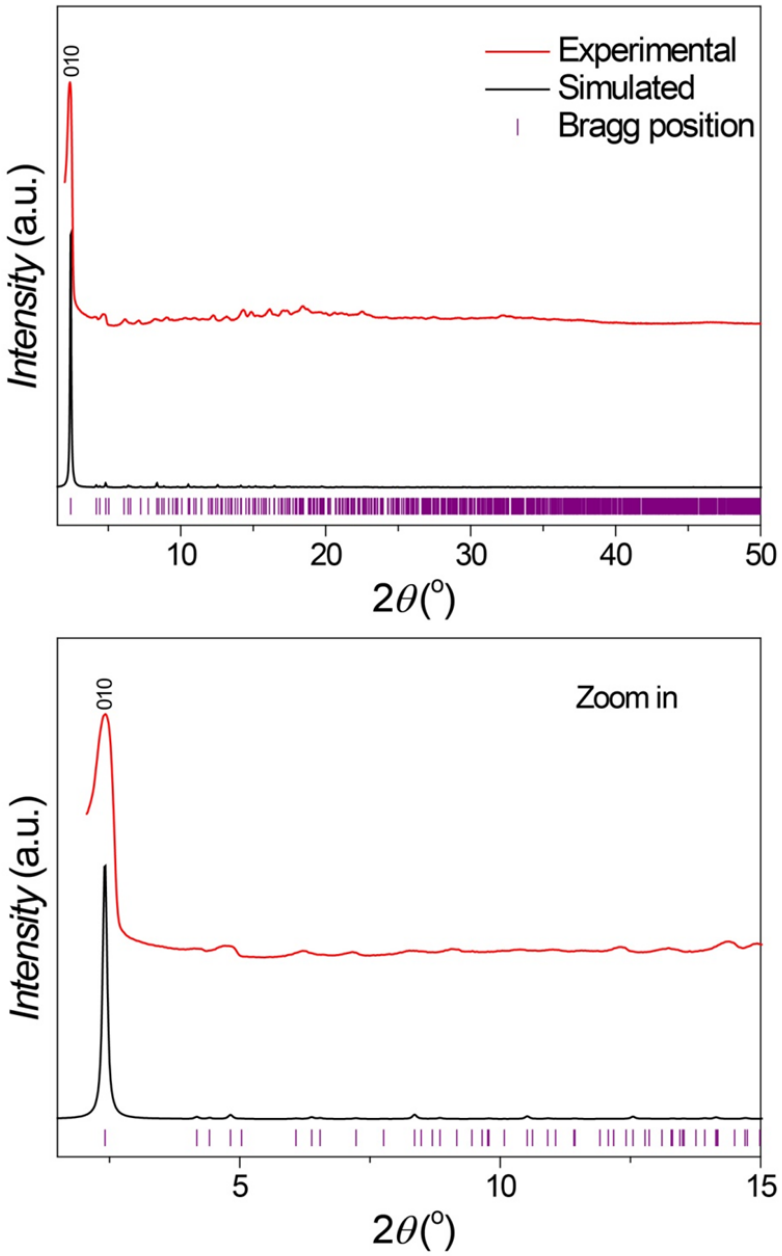

Figure 2.31 Comparison of the experimental PXRD patterns of ZIF-725: activated (red) and simulated pattern (black) from single crystal X-ray data (Full scale 1.5-50 ° and zoom in 1.5-15 °).

Thermal gravimetric analysis. Thermal gravimetric analysis (TGA) curves were recorded on a TA Q500 thermal analysis system under air flow. All ZIFs show high thermal stability and decompose in air up to 300 °C.

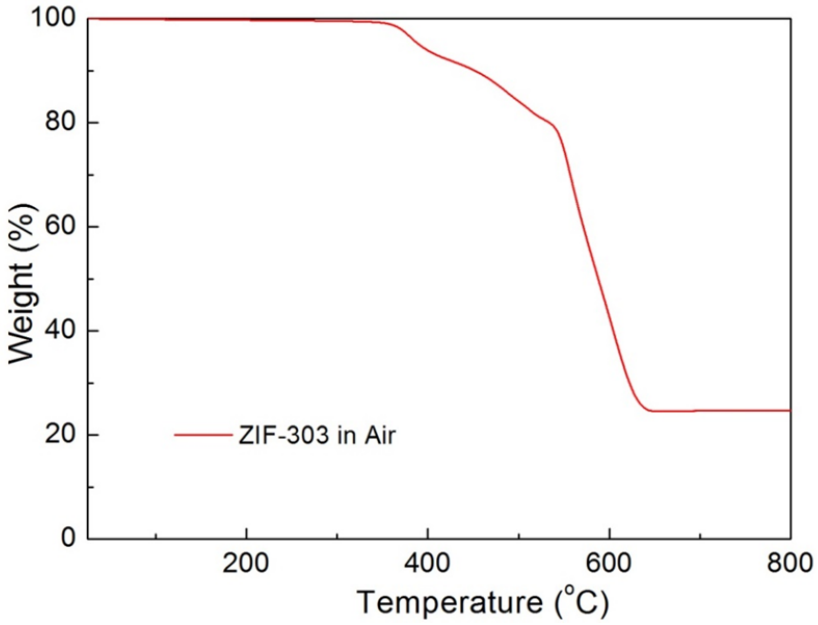

Figure 2.32 TGA trace for the activated sample of ZIF-303.

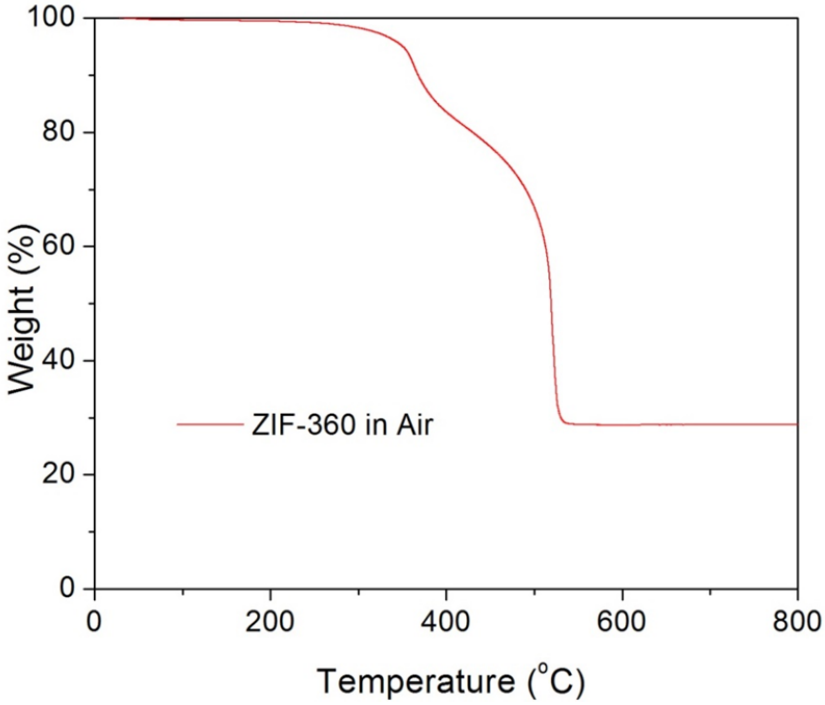

Figure 2.33 TGA trace for the activated sample of ZIF-360.

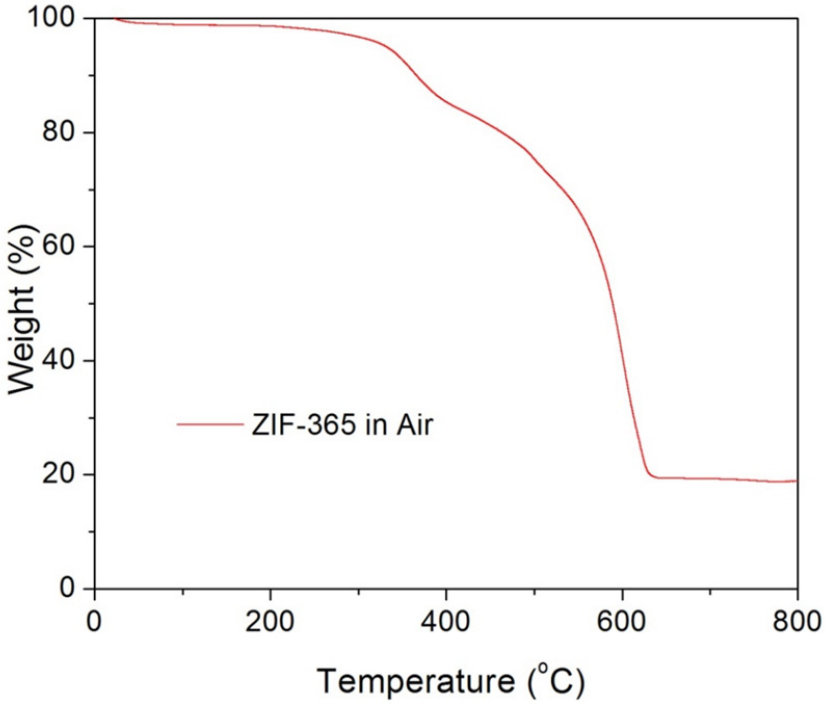

Figure 2.34 TGA trace for the activated sample of ZIF-365.

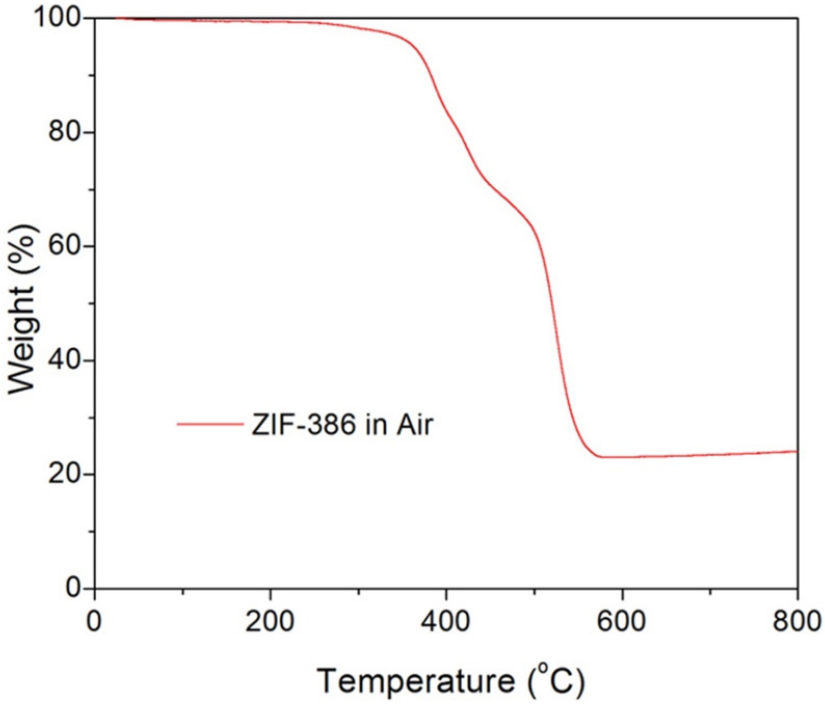

Figure 2.35 TGA trace for the activated sample of ZIF-386.

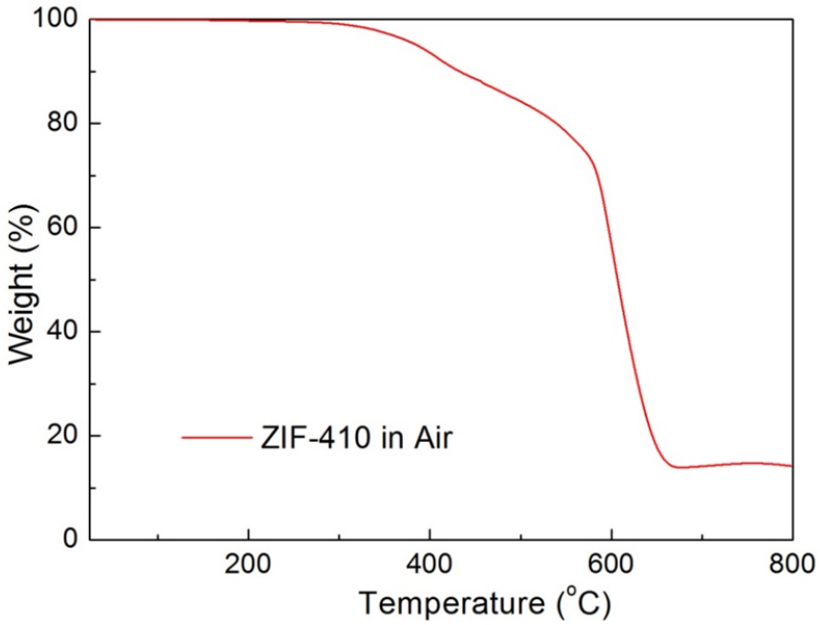

Figure 2.36 TGA trace for the activated sample of ZIF-410.

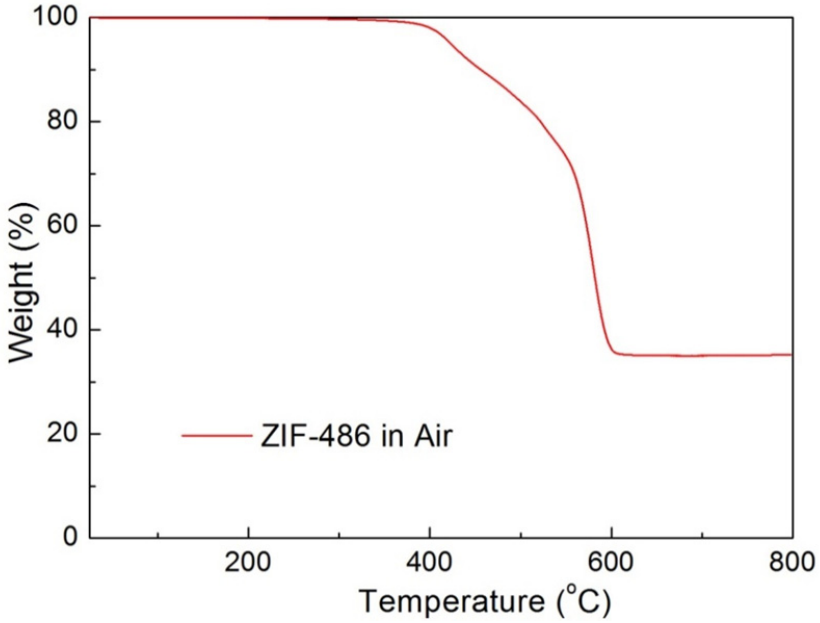

Figure 2.37 TGA trace for the activated sample of ZIF-486.

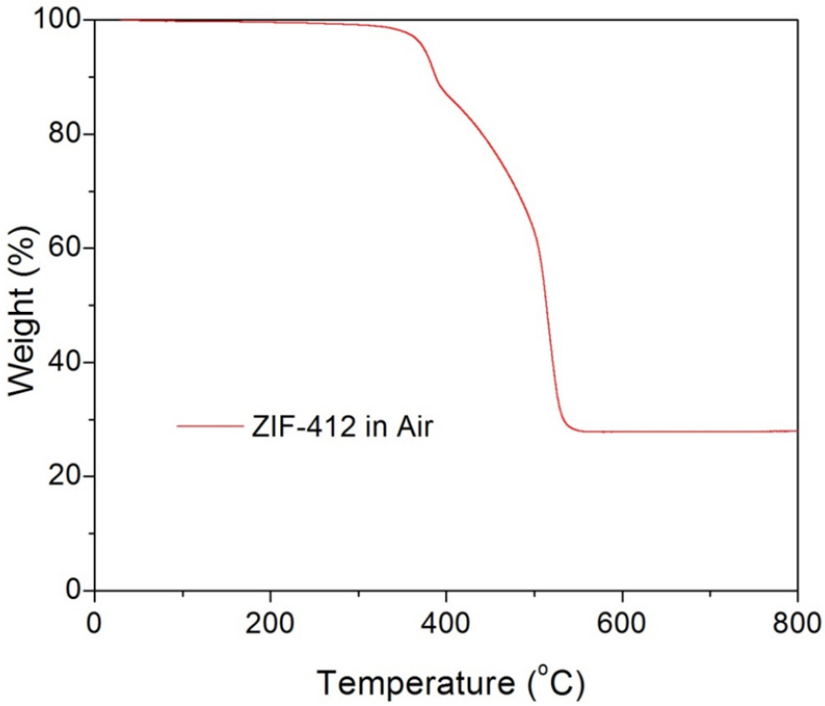

Figure 2.38 TGA trace for the activated sample of ZIF-412.

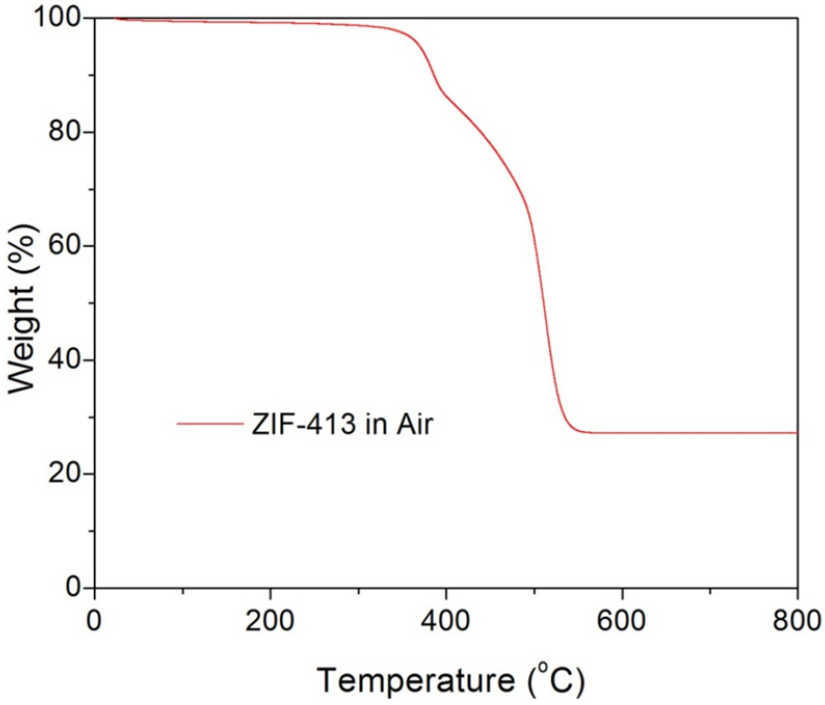

Figure 2.39 TGA trace for the activated sample of ZIF-413.

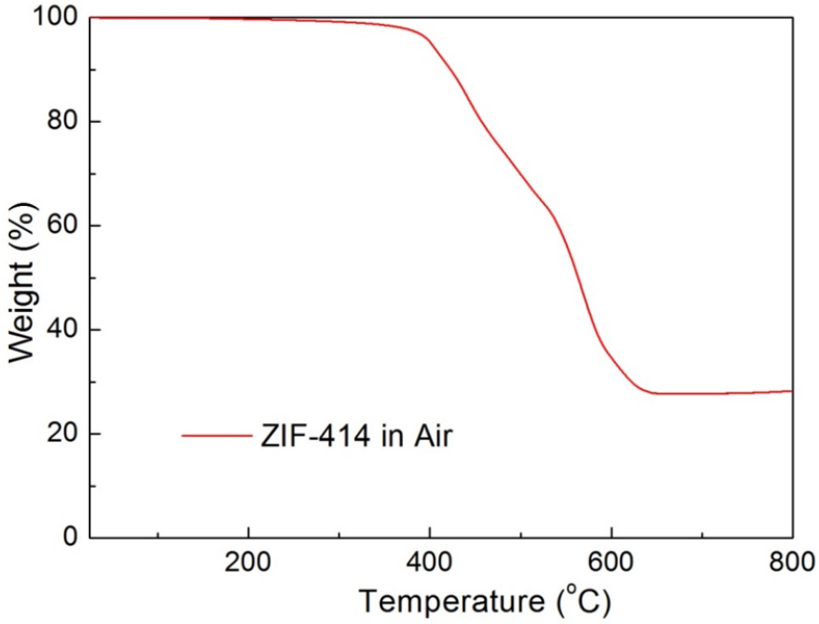

Figure 2.40 TGA trace for the activated sample of ZIF-414.

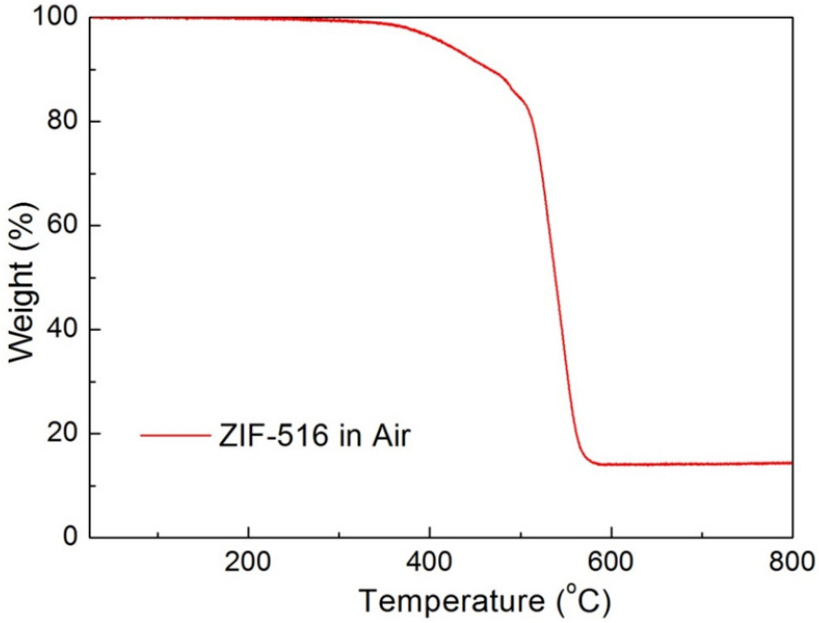

Figure 2.41 TGA trace for the activated sample of ZIF-516.

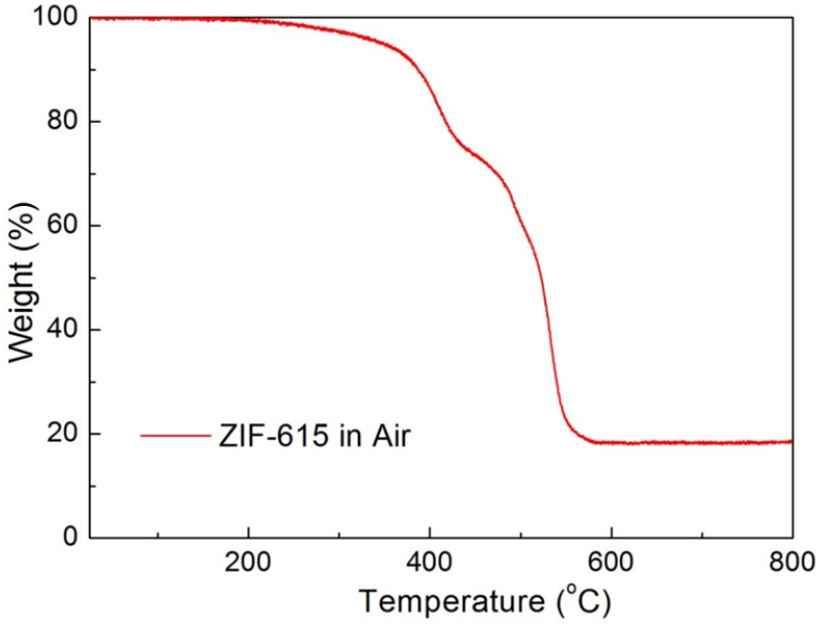

Figure 2.42 TGA trace for the activated sample of ZIF-615.

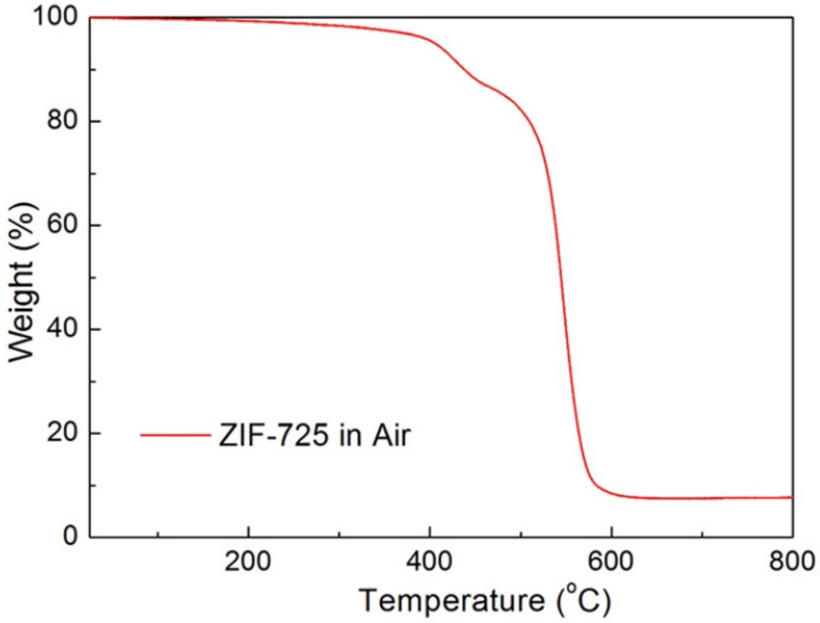

Figure 2.43 TGA trace for the activated sample of ZIF-725.

Low pressure gas adsorption measurements. Ultrahigh-grade gases (99.999% for N_2, Ar, CO_2, CH_4, and He) and activated samples of ZIFs were used for gas adsorption measurements. The N_2 (77 K) isotherms for all ZIFs were measured on a Quadrasorb-SI. Apparent surface area of ZIFs were estimated by Langmuir and BET methods. The CO_2, CH_4, and N_2 adsorption isotherms of reported ZIFs were measured using Autosorb-1 (Quantachrome) volumetric gas adsorption analyzer.

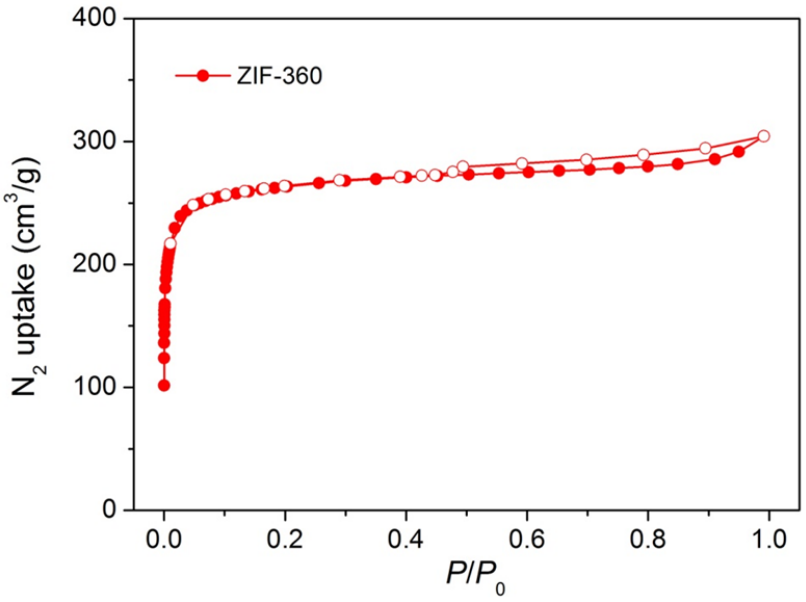

Figure 2.44 Low-pressure nitrogen adsorption isotherm[22] of ZIF-360 at 77 K.

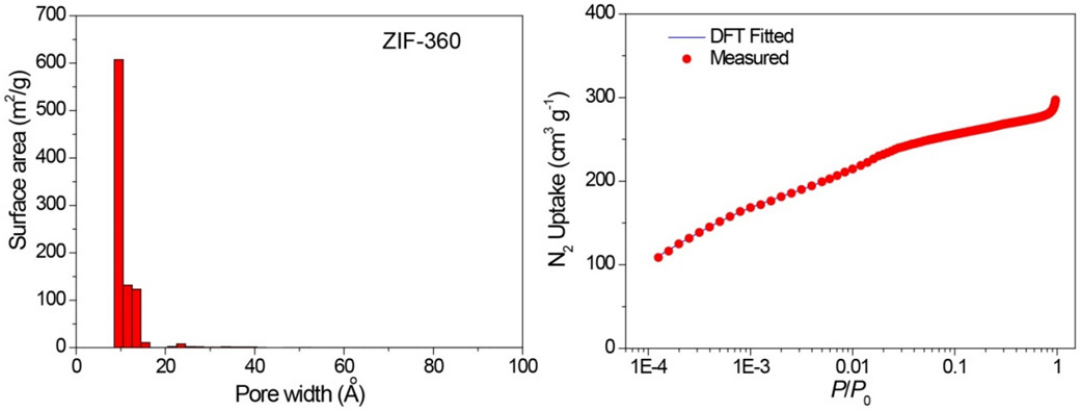

Figure 2.45 (a) Pore size distribution histogram of ZIF-360 calculated from DFT/Monte-Carlo fitting[23] of the adsorption branch of the N_2 adsorption isotherm at 77 K (b) with the fitting error of 0.099% using slit/cylindr./sphere pores QSDFT model.

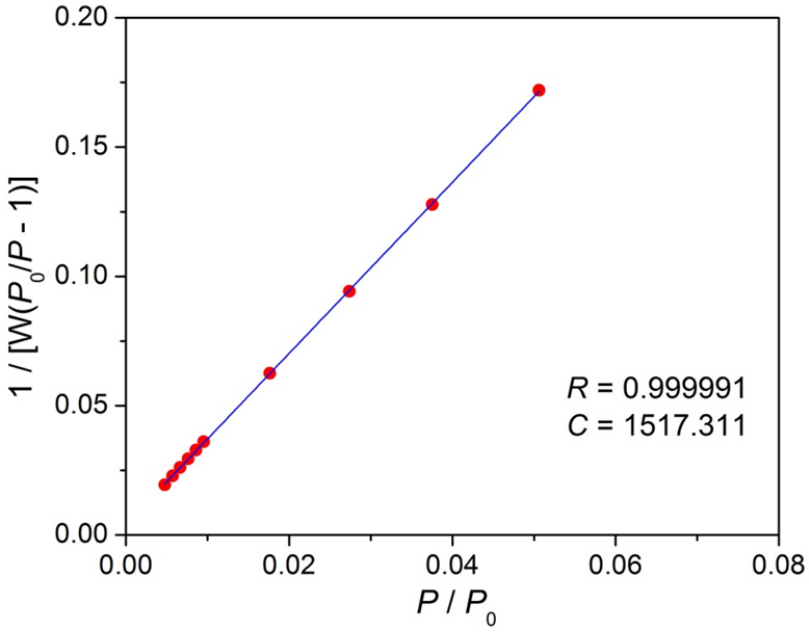

Figure 2.46 Multiple point BET[24] plot of ZIF-360 giving a specific surface area of 1050 m^2/g.

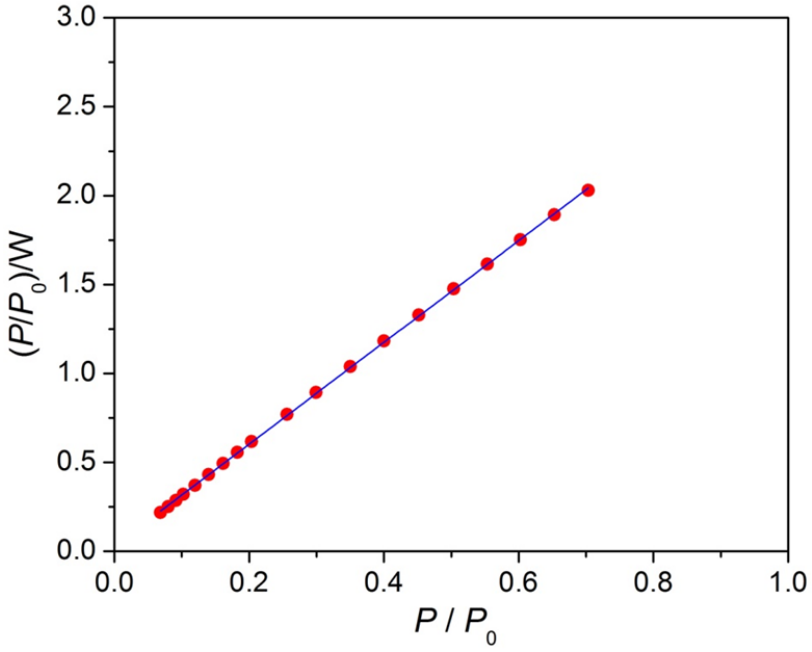

Figure 2.47 Langmuir plot of ZIF-360 giving a specific surface area of 1220 m^2/g.

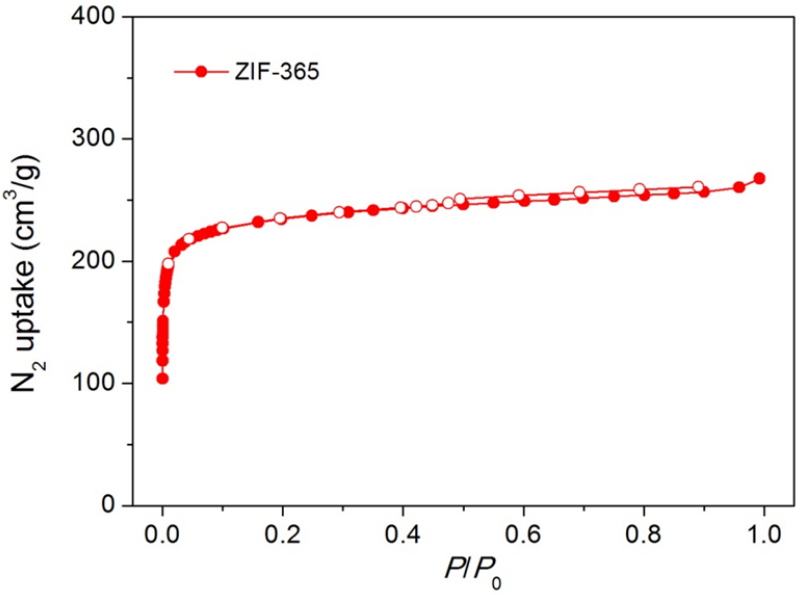

Figure 2.48 Low-pressure nitrogen adsorption isotherm of ZIF-365 at 77 K.

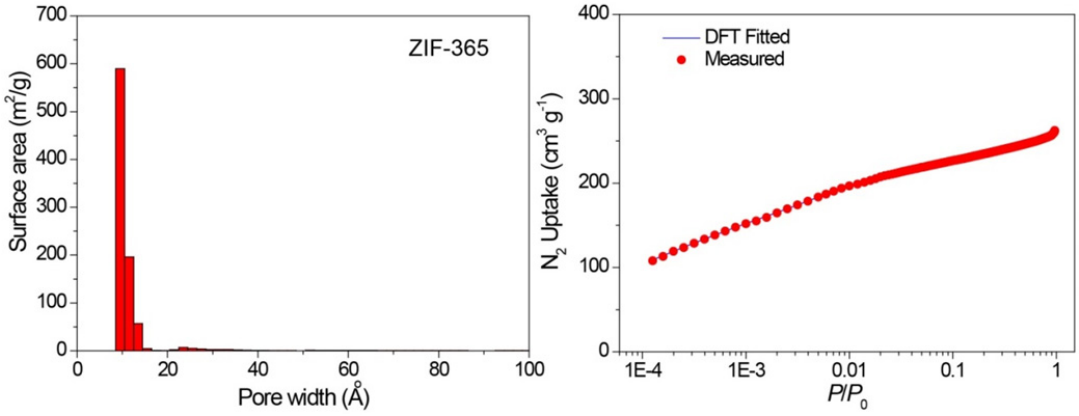

Figure 2.49 (a) Pore size distribution histogram of ZIF-365 calculated from DFT/Monte-Carlo fitting of the adsorption branch of the N_2 adsorption isotherm at 77 K (b) with the fitting error of 0.052% using slit/cylindr./sphere pores QSDFT model.

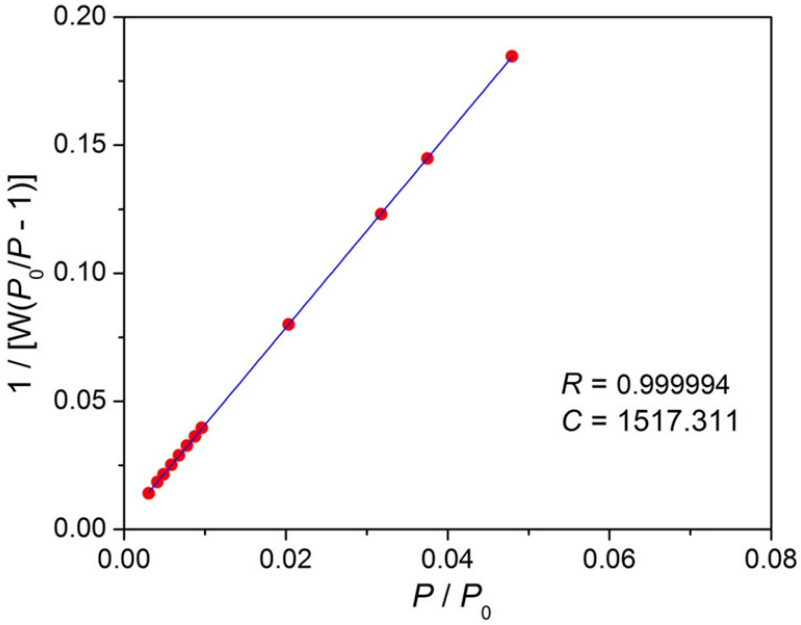

Figure 2.50 Multiple point BET plot of ZIF-365 giving a specific surface area of 920 m^2/g.

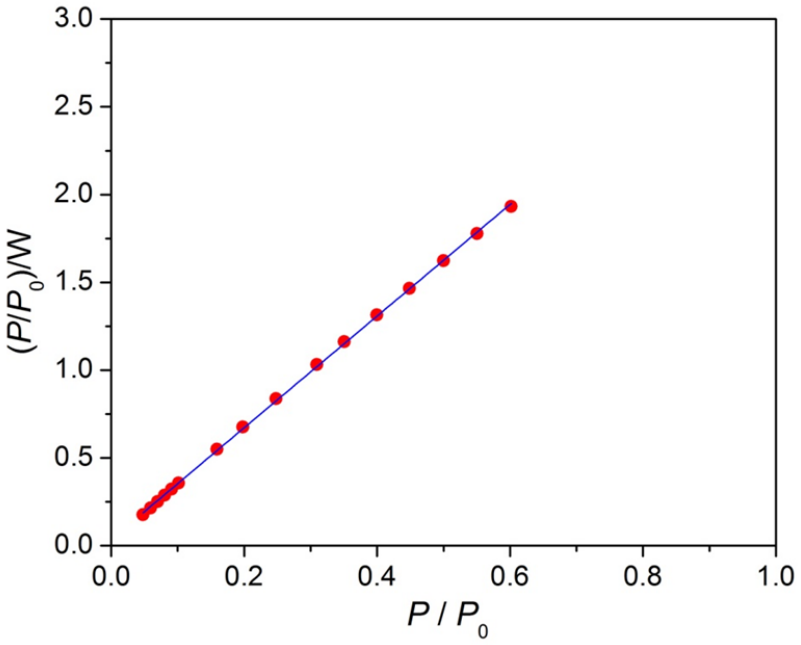

Figure 2.51 Langmuir plot of ZIF-365 giving a specific surface area of 1095 m^2/g.

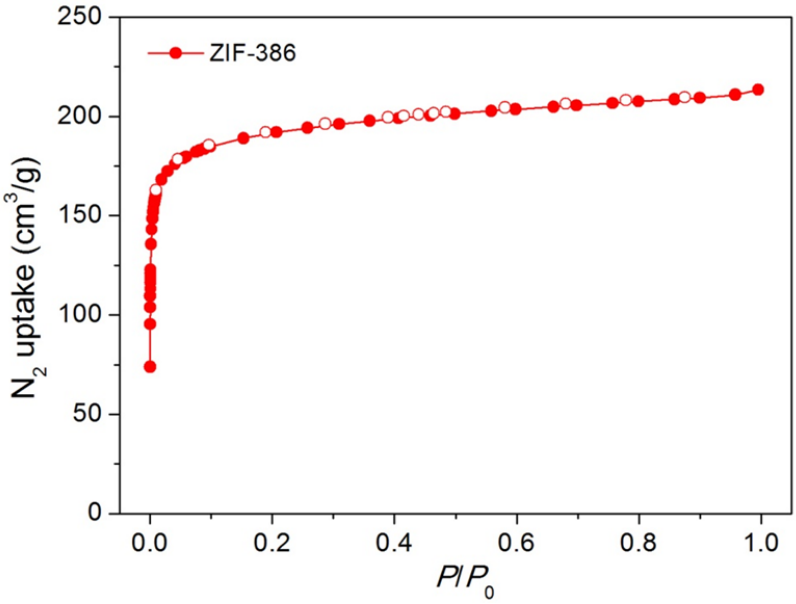

Figure 2.52 Nitrogen adsorption isotherm of ZIF-386 at 77 K.

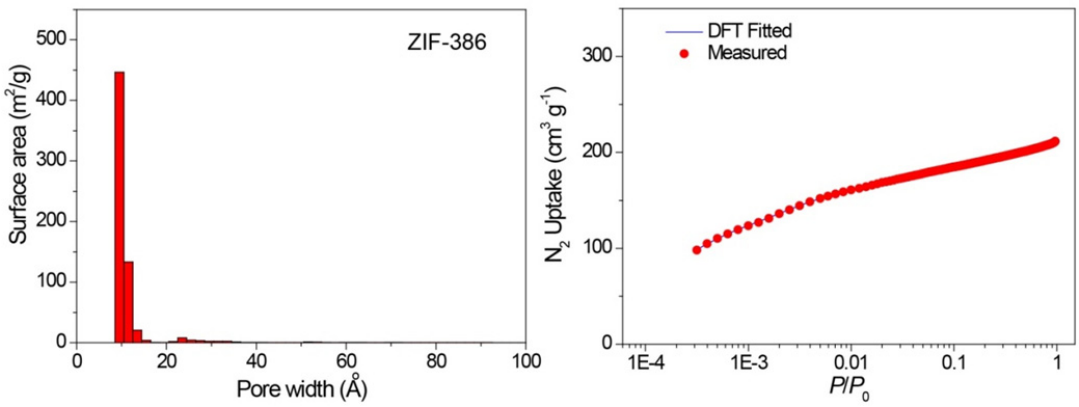

Figure 2.53 (a) Pore size distribution histogram of ZIF-386 calculated from DFT/Monte-Carlo fitting of the adsorption branch of the N_2 adsorption isotherm at 77 K (b) with the fitting error of 0.029% using slit/cylindr./sphere pores QSDFT model.

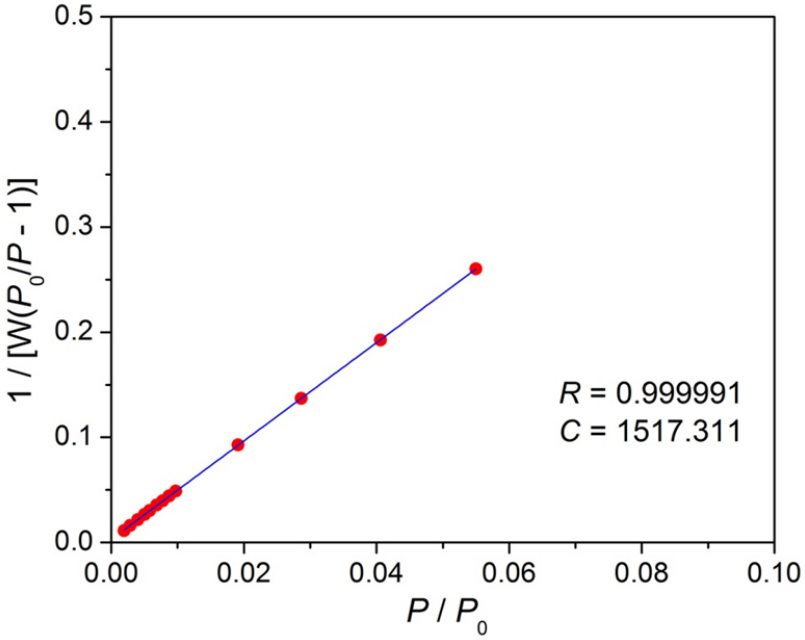

Figure 2.54 Multiple point BET plot of ZIF-386 giving a specific surface area of 740 m^2/g.

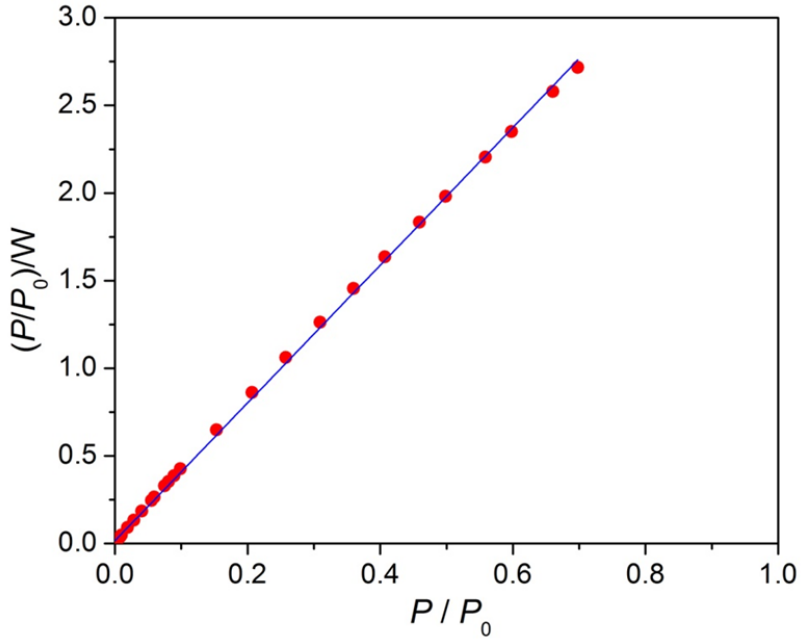

Figure 2.55 Langmuir plot of ZIF-386 giving a specific surface area of 890 m^2/g.

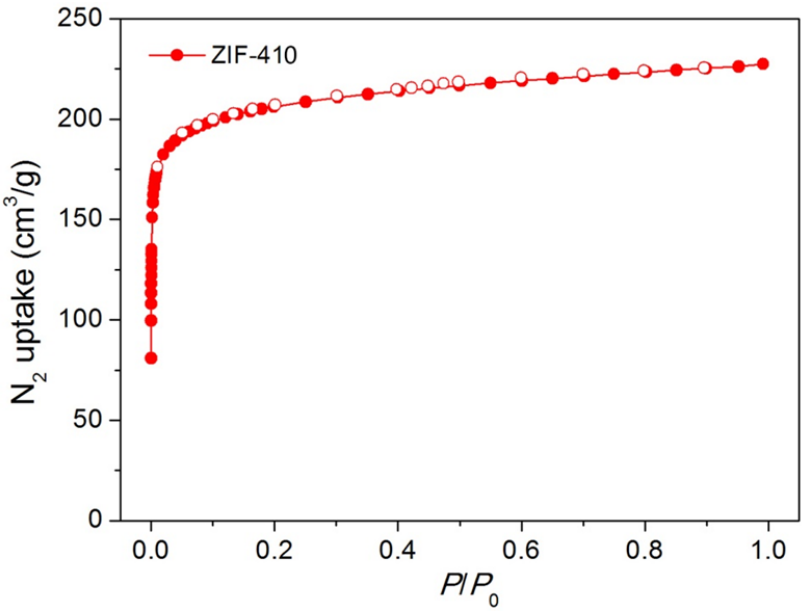

Figure 2.56 Nitrogen adsorption isotherm of ZIF-410 at 77 K.

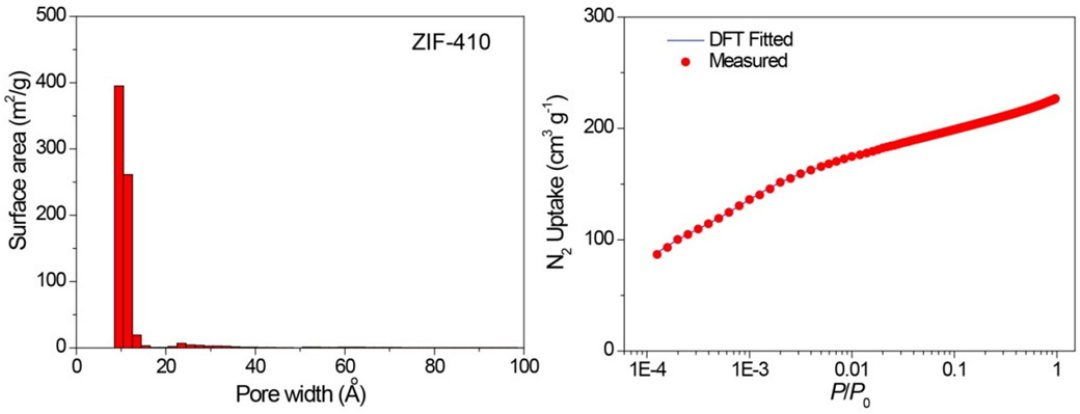

Figure 2.57 (a) Pore size distribution histogram of ZIF-410 calculated from DFT/Monte-Carlo fitting of the adsorption branch of the N_2 adsorption isotherm at 77 K (b) with the fitting error of 0.023% using slit/cylindr./sphere pores QSDFT model.

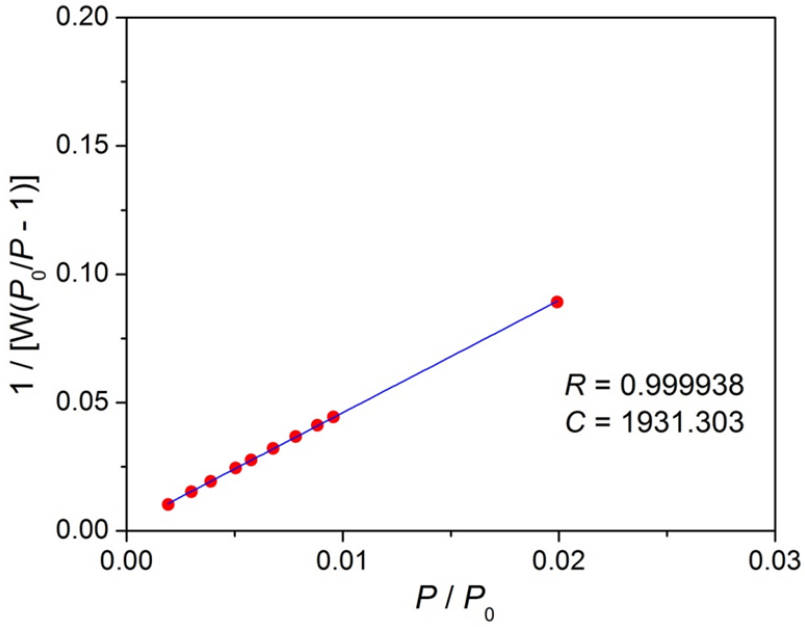

Figure 2.58 Multiple point BET plot of ZIF-410 giving a specific surface area of 795 m^2/g.

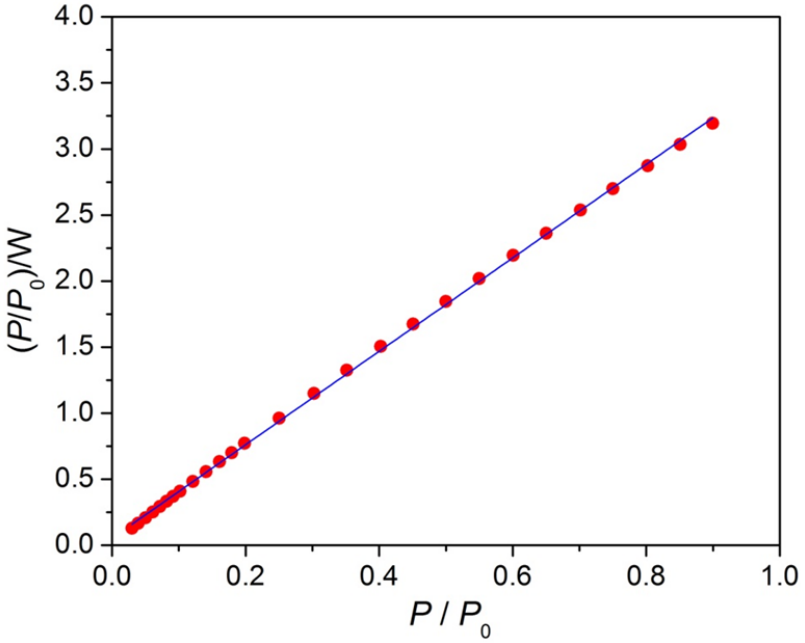

Figure 2.59 Langmuir plot of ZIF-410 giving a specific surface area of 985 m^2/g.

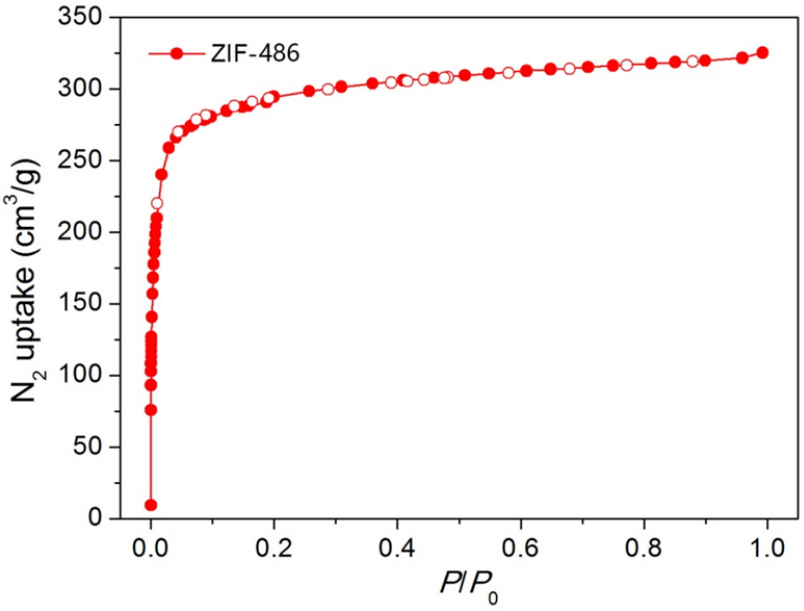

Figure 2.60 Nitrogen adsorption isotherm of ZIF-486 at 77 K.

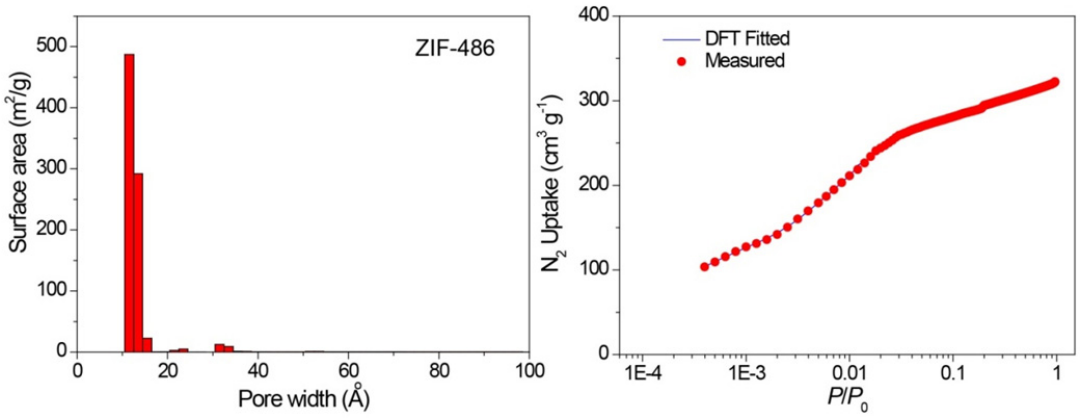

Figure 2.61 (a) Pore size distribution histogram of ZIF-486 calculated from DFT/Monte-Carlo fitting of the adsorption branch of the N_2 adsorption isotherm at 77 K (b) with the fitting error of 0.096% using slit/cylindr./sphere pores QSDFT model.

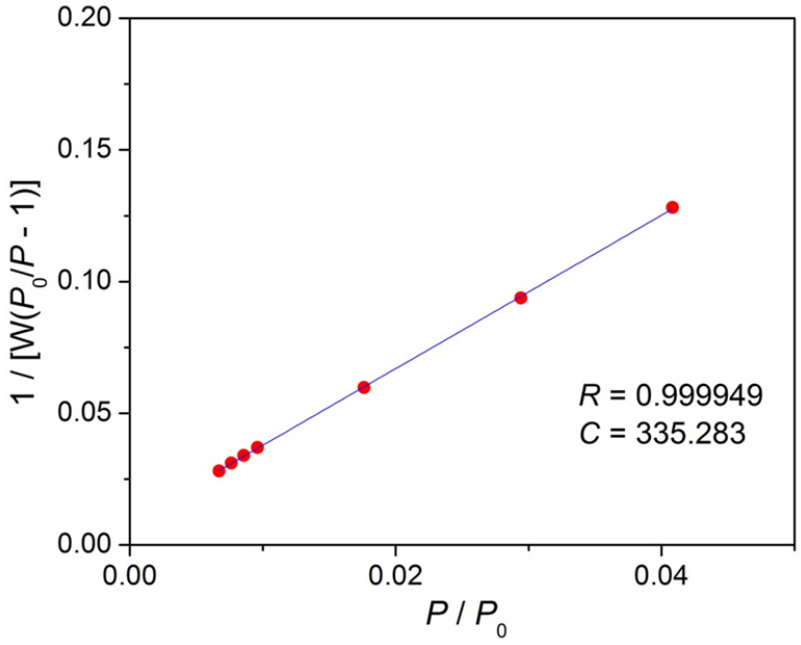

Figure 2.62 Multiple point BET plot of ZIF-486 giving a specific surface area of 1184 m^2/g.

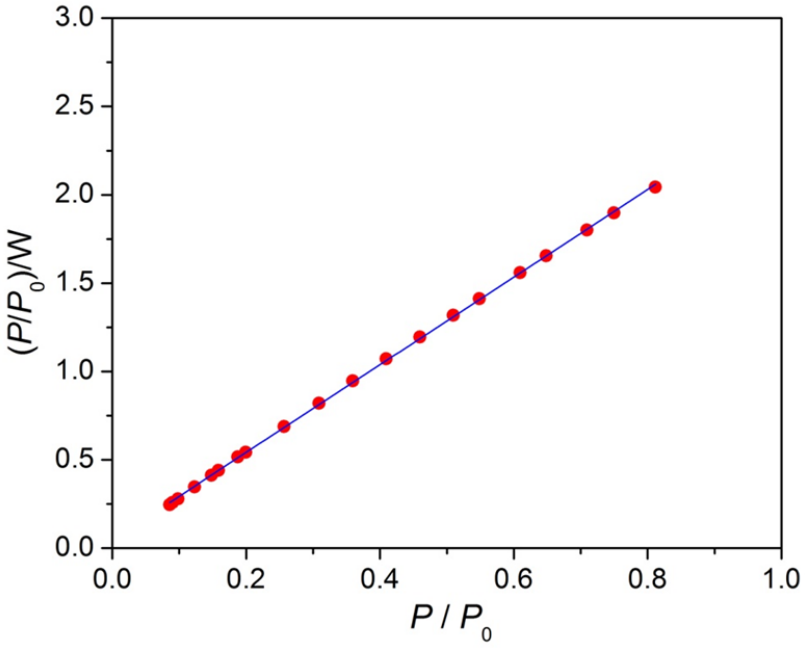

Figure 2.63 Langmuir plot of ZIF-486 giving a specific surface area of 1404 m^2/g.

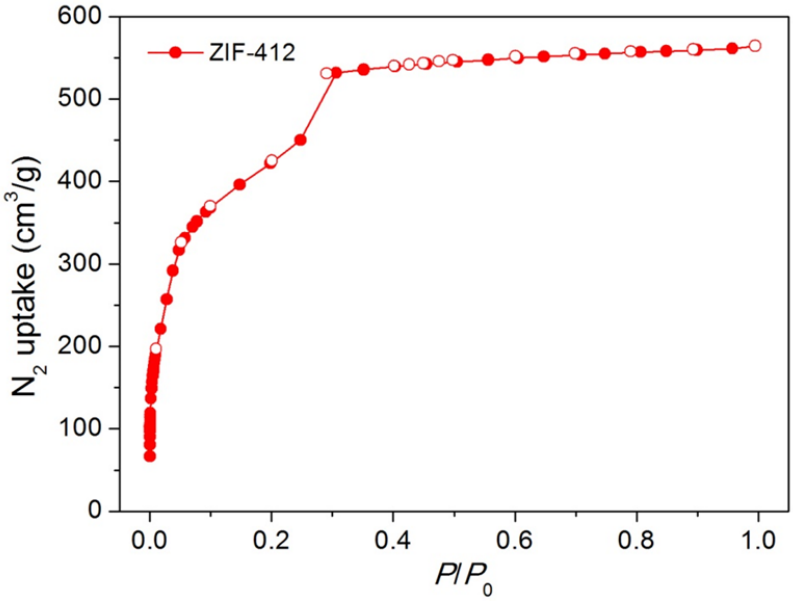

Figure 2.64 Nitrogen adsorption isotherm of ZIF-412 at 77 K.

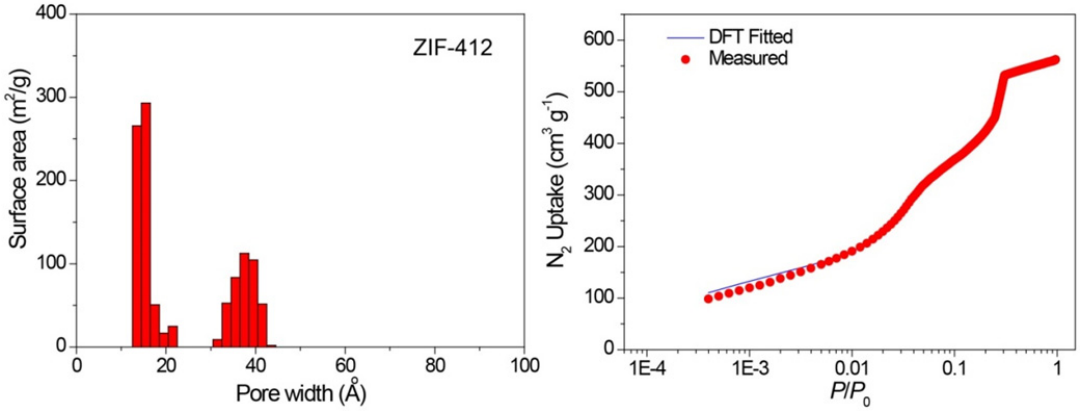

Figure 2.65 (a) Pore size distribution histogram of ZIF-412 calculated from DFT/Monte-Carlo fitting of the adsorption branch of the N_2 adsorption isotherm at 77 K (b) with the fitting error of 0.455% using slit/cylindr./sphere pores QSDFT model.

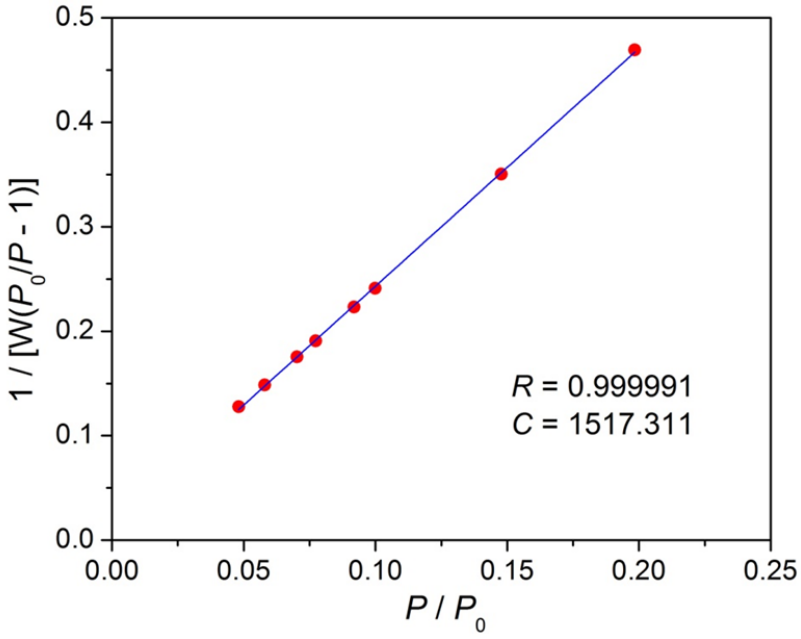

Figure 2.66 Multiple point BET plot of ZIF-412 giving a specific surface area of 1520 m^2/g.

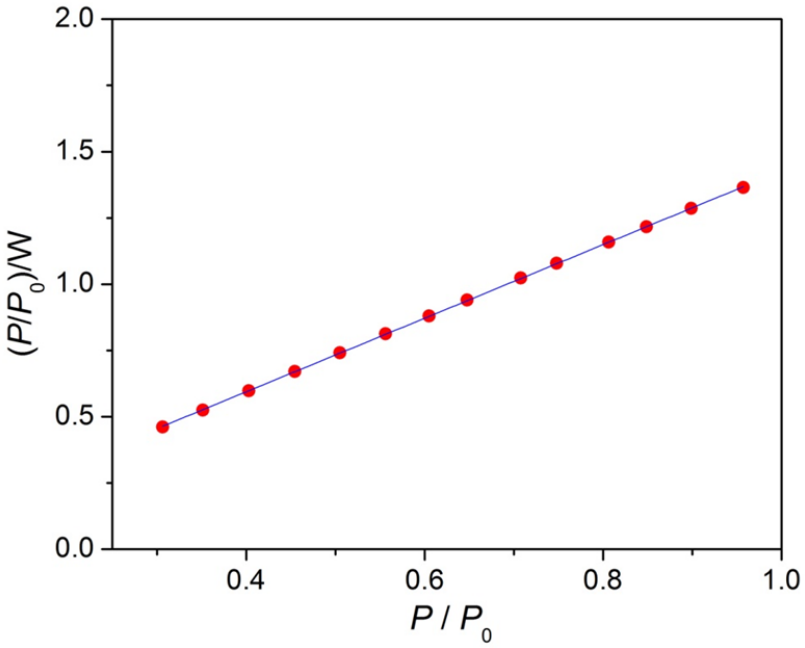

Figure 267 Langmuir plot of ZIF-412 giving a specific surface area of 2500 m^2/g.

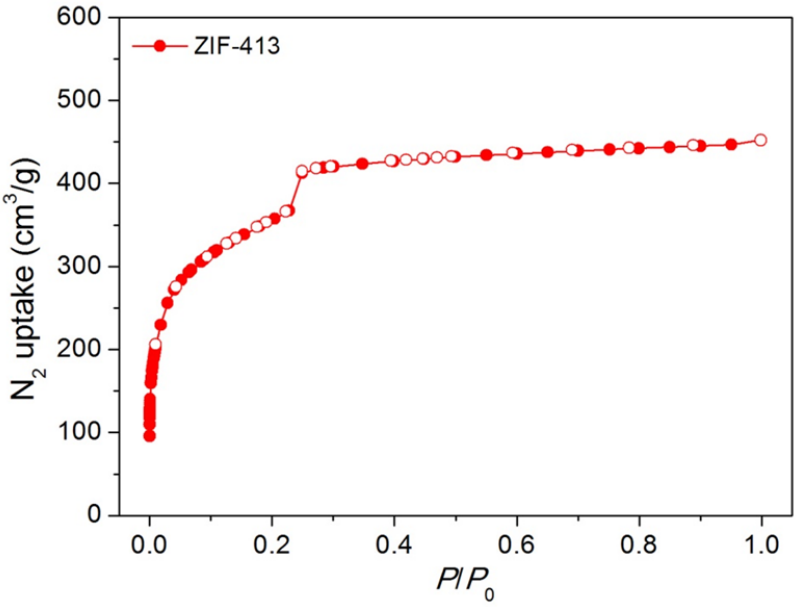

Figure 2.68 Low-pressure nitrogen adsorption isotherm of ZIF-413 at 77 K.

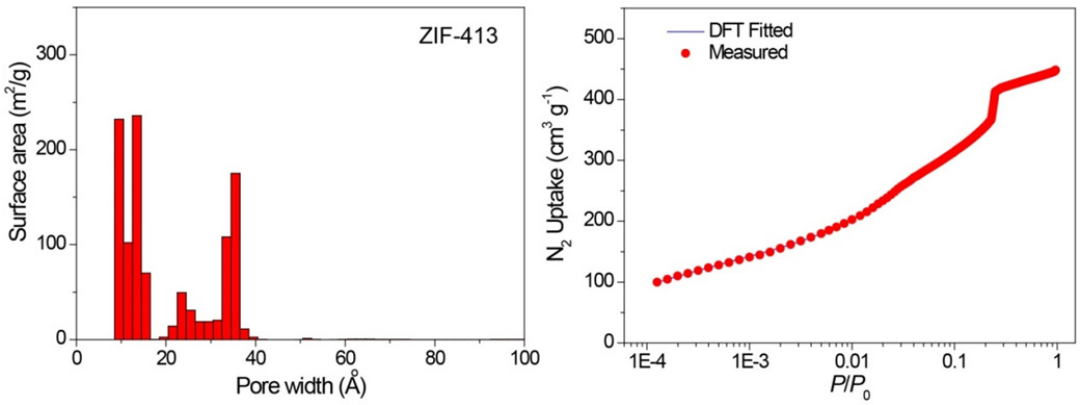

Figure 2.69 (a) Pore size distribution histogram of ZIF-413 calculated from DFT/Monte-Carlo fitting of the adsorption branch of the N_2 adsorption isotherm at 77 K (b) with the fitting error of 0.259% using slit/cylindr./sphere pores QSDFT model.

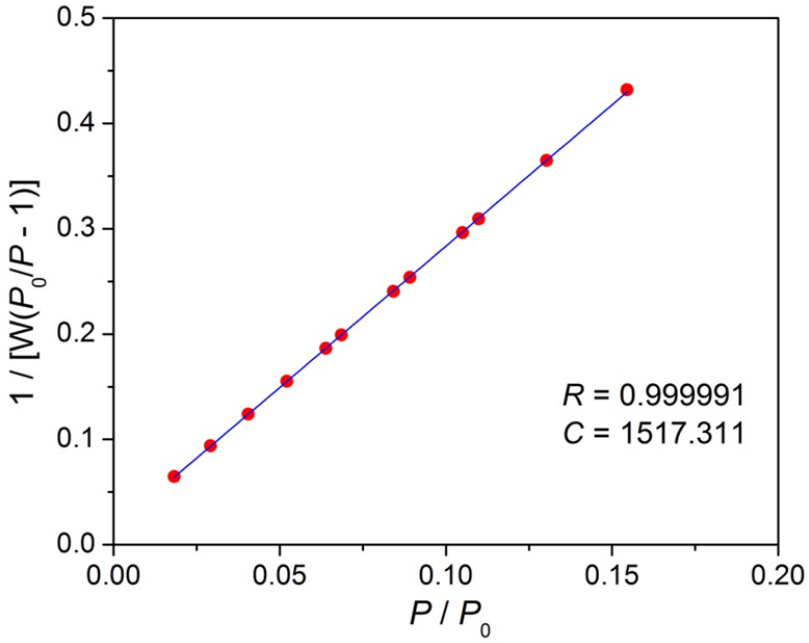

Figure 2.70 Multiple point BET plot of ZIF-413 giving a specific surface area of 1290 m^2/g.

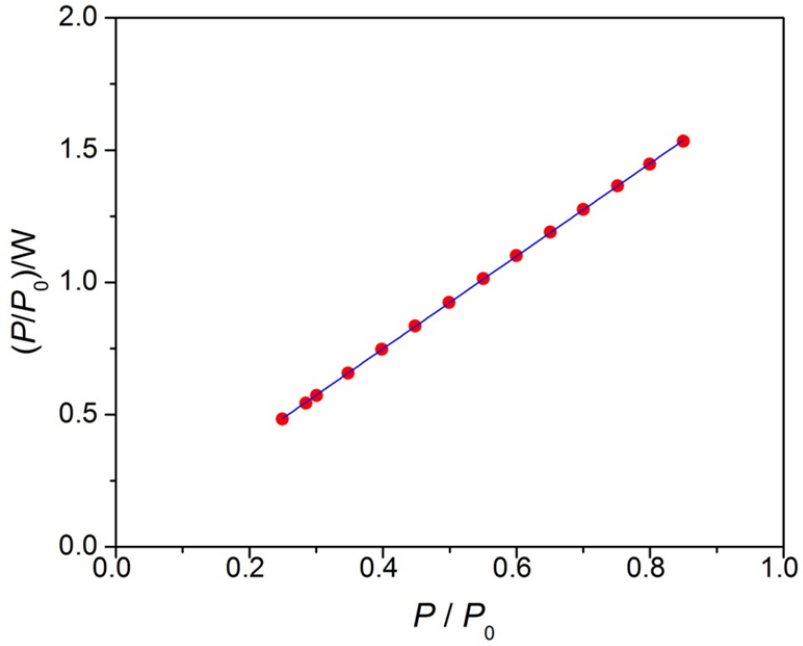

Figure 2.71 Langmuir plot of ZIF-413 giving a specific surface area of 1990 m^2/g.

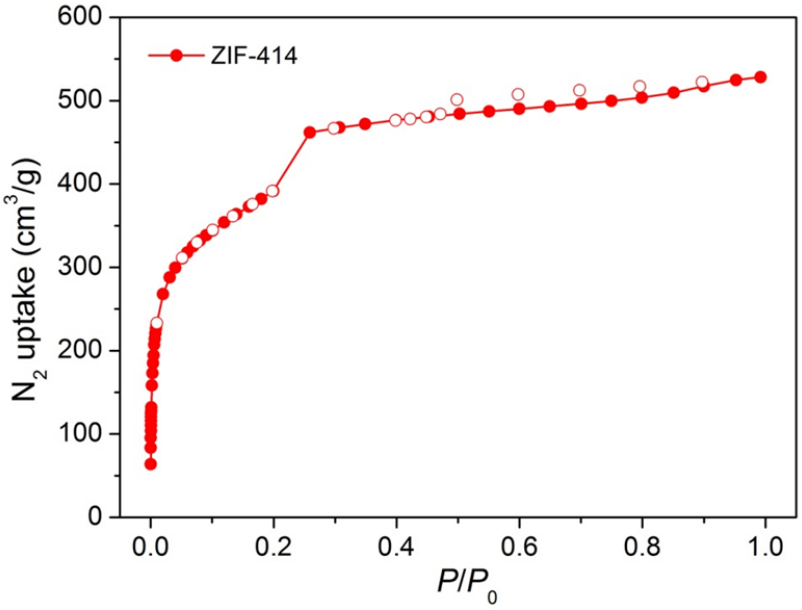

Figure 2.72 Nitrogen adsorption isotherm of ZIF-414 at 77 K.

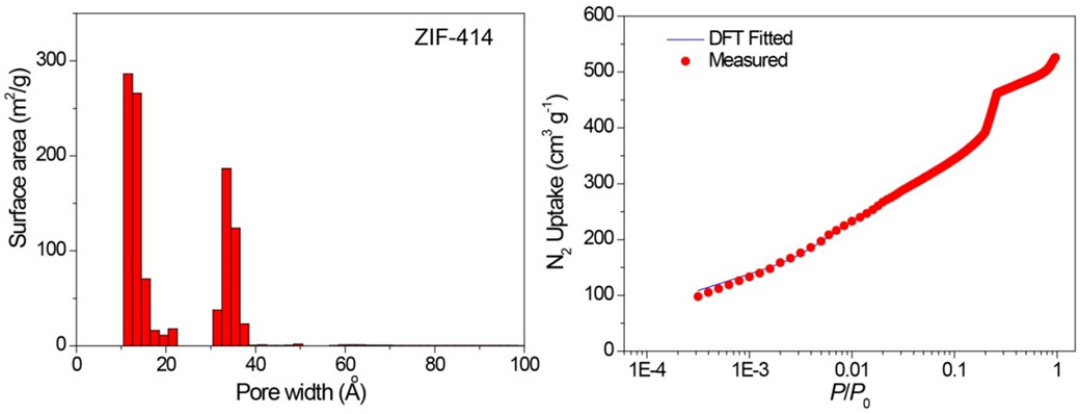

Figure 2.73 (a) Pore size distribution histogram of ZIF-414 calculated from DFT/Monte-Carlo fitting of the adsorption branch of the N_2 adsorption isotherm at 77 K (b) with the fitting error of 0.340% using slit/cylindr./sphere pores QSDFT model.

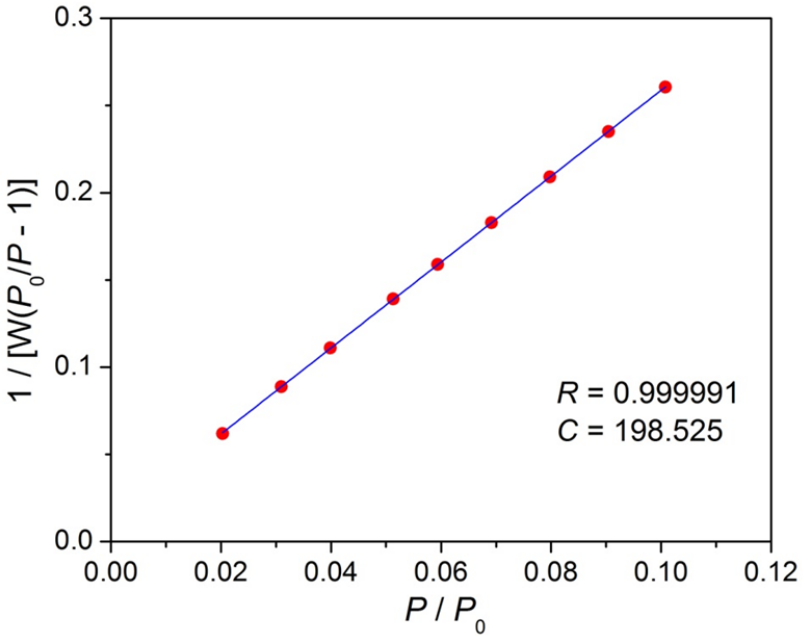

Figure 2.74 Multiple point BET plot of ZIF-414 giving a specific surface area of 1440 m^2/g.

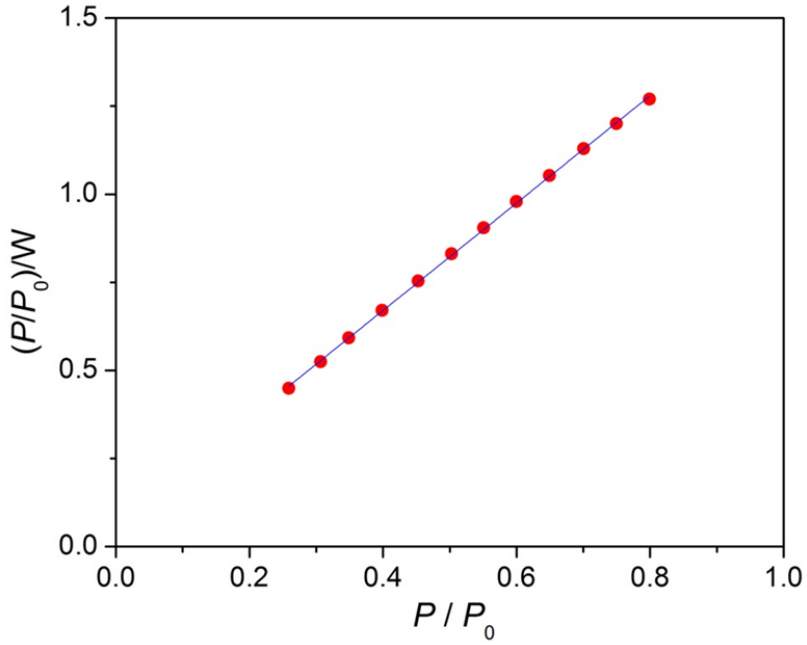

Figure 2.75 Langmuir plot of ZIF-414 giving a specific surface area of 2284 m^2/g.

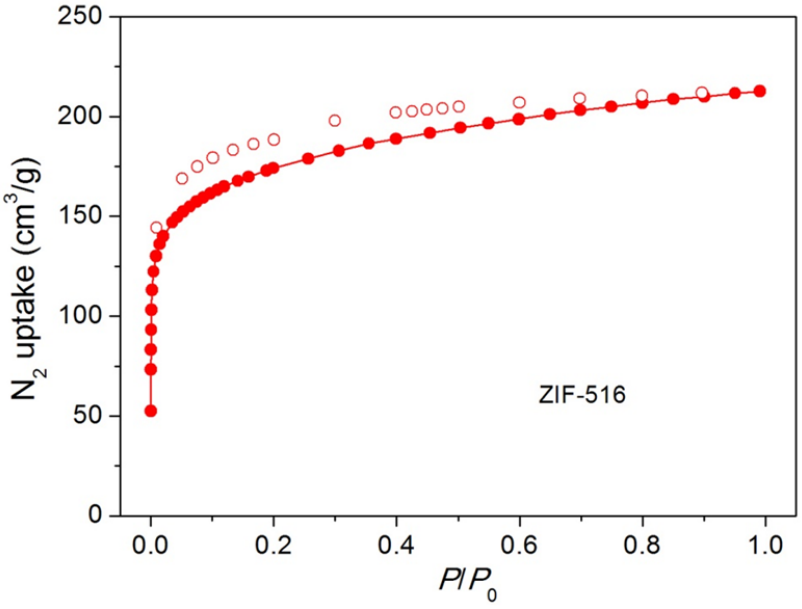

Figure 2.76 Nitrogen adsorption isotherm of ZIF-516 at 77 K.

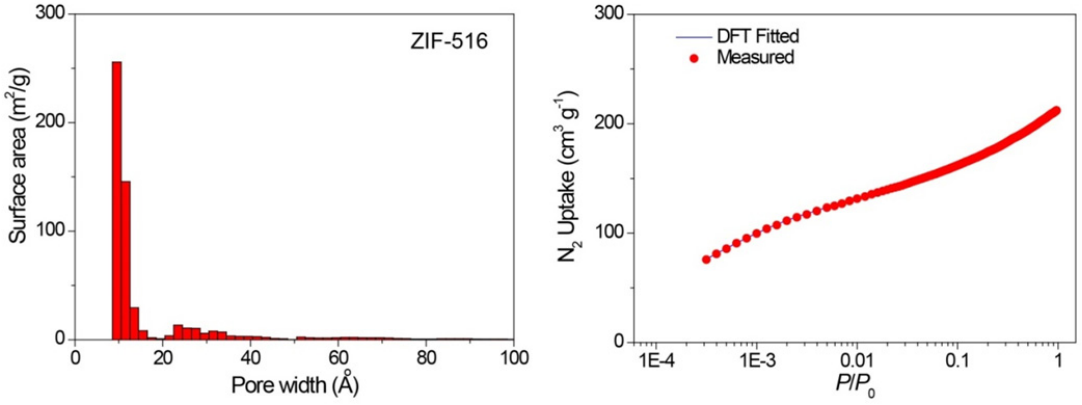

Figure 2.77 (a) Pore size distribution histogram of ZIF-516 calculated from DFT/Monte-Carlo fitting of the adsorption branch of the N_2 adsorption isotherm at 77 K (b) with the fitting error of 0.048% using slit/cylindr./sphere pores QSDFT model.

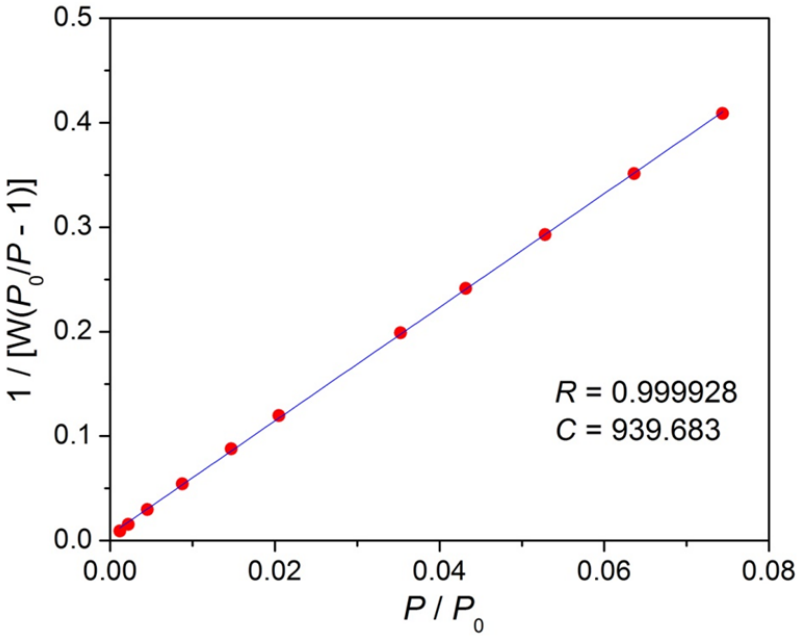

Figure 2.78 Multiple point BET plot of ZIF-516 giving a specific surface area of 639 m^2/g.

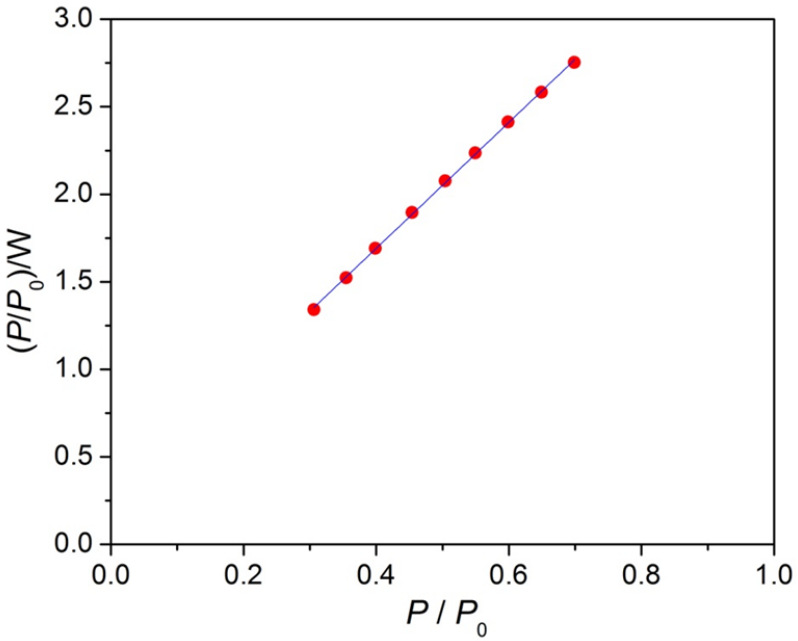

Figure 2.79 Langmuir plot of ZIF-516 giving a specific surface area of 967 m^2/g.

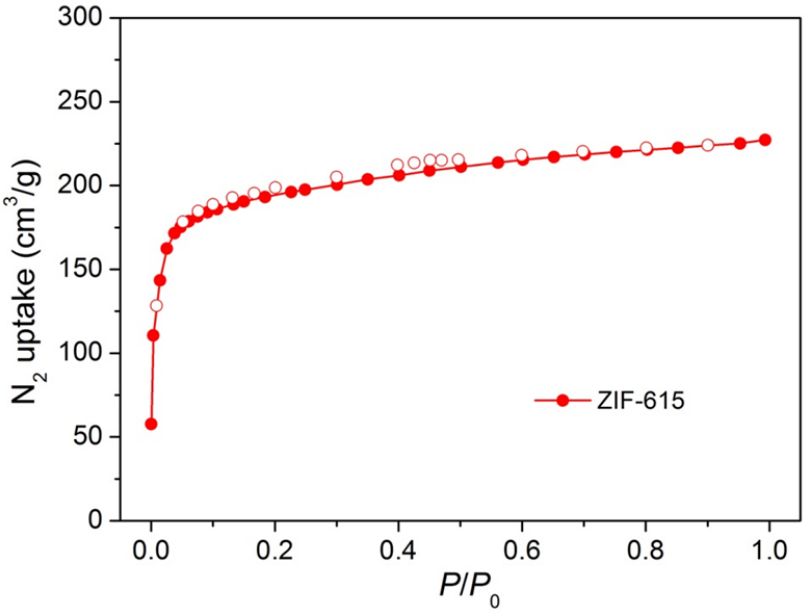

Figure 2.80 Nitrogen adsorption isotherm of ZIF-615 at 77 K.

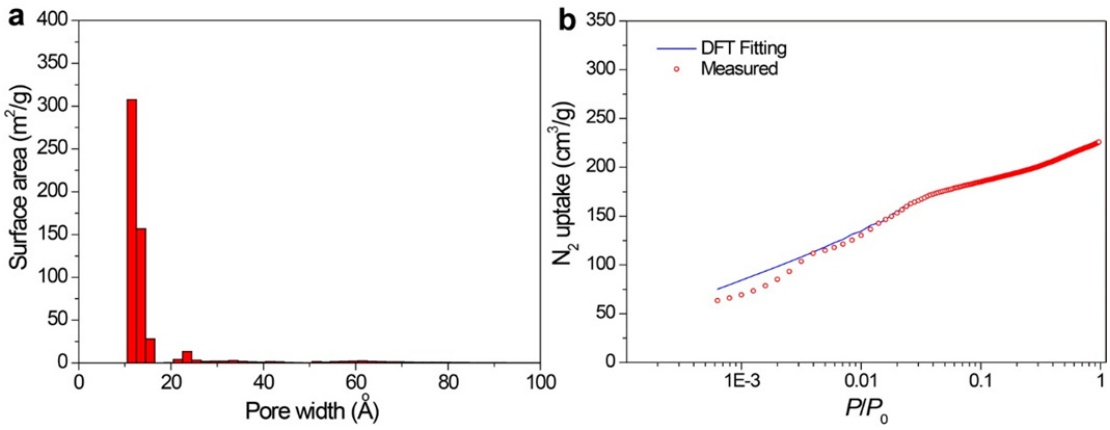

Figure 2.81 (a) Pore size distribution histogram of ZIF-615 calculated from DFT/Monte-Carlo fitting of the adsorption branch of the N_2 adsorption isotherm at 77 K (b) with the fitting error of 0.081% using slit/cylindr./sphere pores QSDFT model.

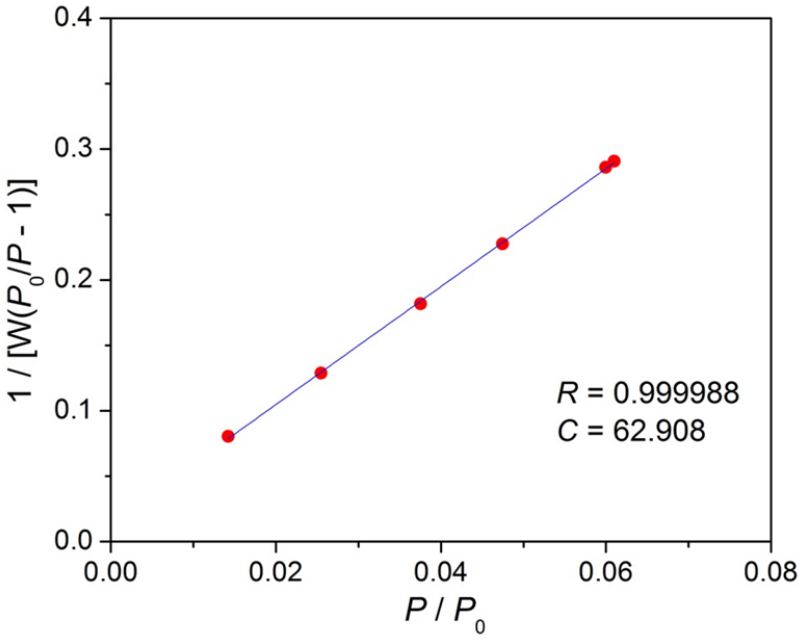

Figure 2.82 Multiple point BET plot of ZIF-615 giving a specific surface area of 769 m^2/g.

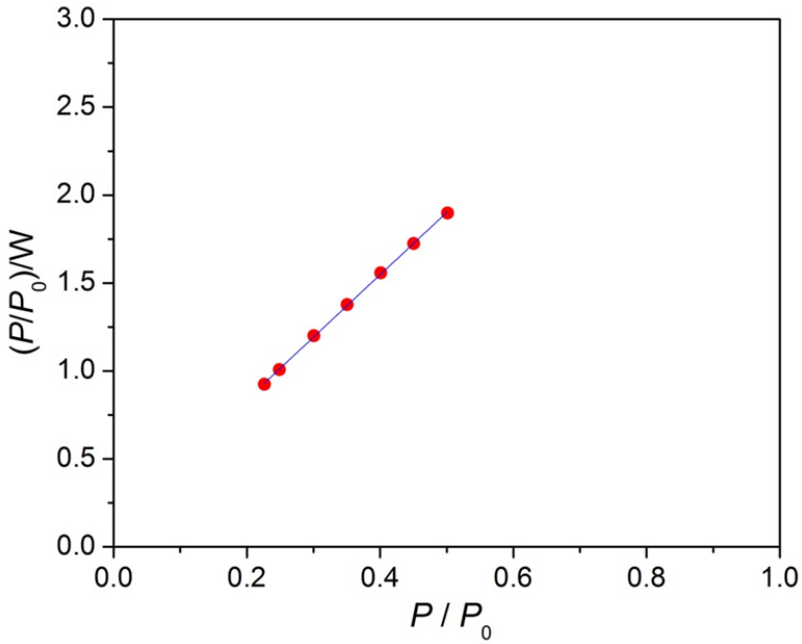

Figure 2.83 Langmuir plot of ZIF-615 giving a specific surface area of 981 m^2/g.

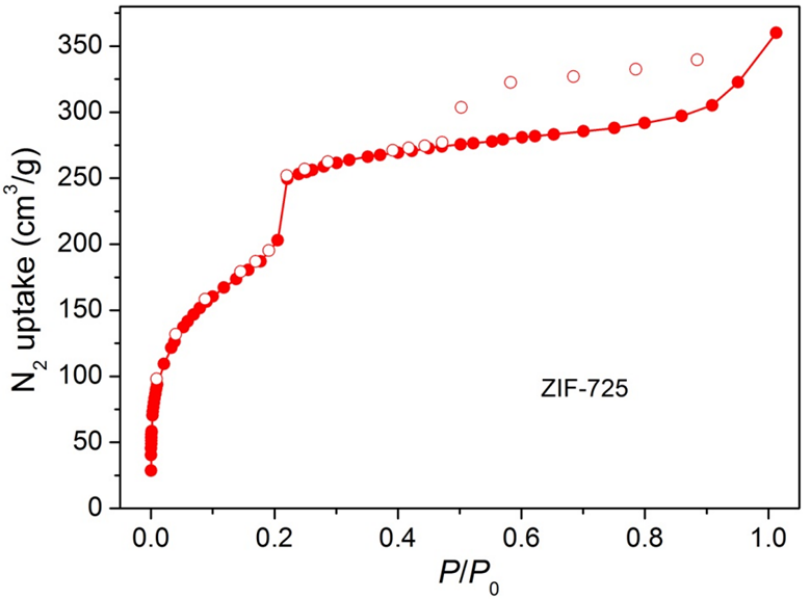

Figure 2.84 Nitrogen adsorption isotherm of ZIF-725 at 77 K.

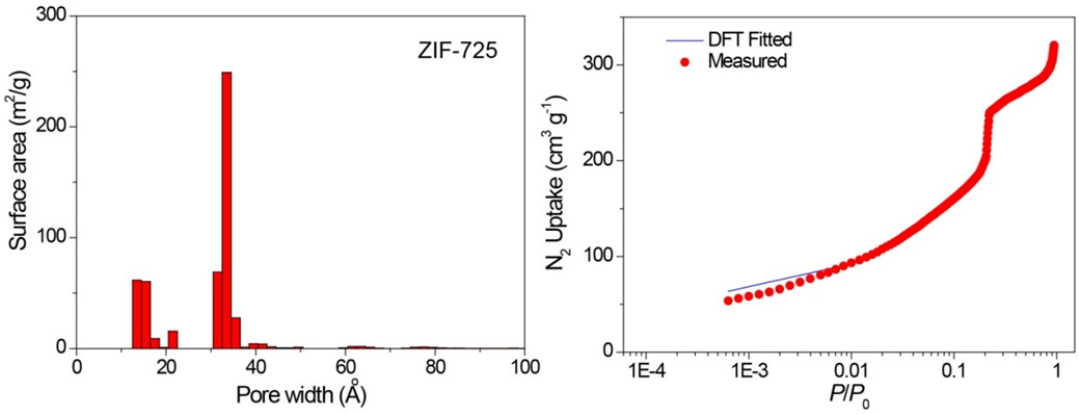

Figure 2.85 (a) Pore size distribution histogram of ZIF-725 calculated from DFT/Monte-Carlo fitting of the adsorption branch of the N_2 adsorption isotherm at 77 K (b) with the fitting error of 0.878% using slit/cylindr./sphere pores QSDFT model.

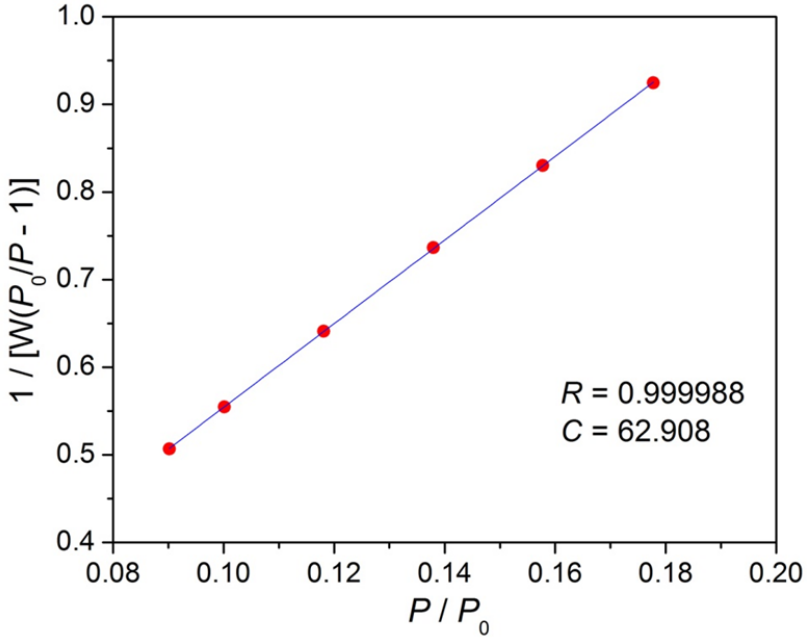

Figure 2.86 Multiple point BET plot of ZIF-725 giving a specific surface area of 718 m^2/g.

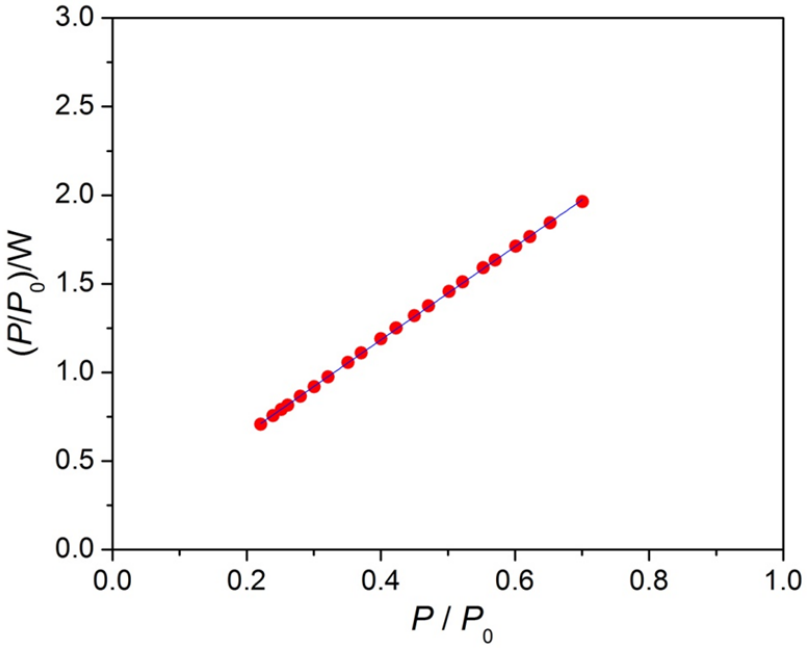

Figure 2.87 Langmuir plot of ZIF-725 giving a specific surface area of 1322 m^2/g.

2.3 Results and Discussions

The linker ratios of all fifteen ZIFs were determined by ^{1}H NMR spectra. As shown in Table 2.1, all the three types of imidazolate linkers are incorporated in each of the ZIFs, suggesting the doability of assembling multiple imidazolates simultaneously which is the base of the present work.

Table 2.1 Chemical compositions, underlying nets, maximum ring sizes (R_{max}), aperture size (d_a), cage size (d_c) of the largest cages, specific surface areas (A_{BET}) and pore size distribution (PSD max, peak maximums of the largest cage) for the obtained ZIFs compared with the state-of-the-art ZIFs and tetrahedral inorganic structures.

Material	Composition	Net	A_{BET} (m^2/g)	R_{max} (MR)	d_a (Å)[a]	d_c (Å)[b]	PSD max (Å)[c]	Reference
ZIF-303	$Zn(cbIM)_{0.70}(nIM)_{0.30}(IM)_{1.00}$	CHA	N/A	8	4.0	21.5	N/A	This work
ZIF-360	$Zn(bIM)_{1.00}(nIM)_{0.70}(IM)_{0.30}$	KFI	1050	8	4.8	27.8	11.0	This work
ZIF-365	$Zn(cbIM)_{0.95}(nIM)_{0.60}(IM)_{0.45}$	KFI	920	8	5.0	27.8	10.1	This work
ZIF-376	$Zn(nbIM)_{0.25}(mIM)_{0.25}(IM)_{1.5}$	LTA	N/A	8	6.9	27.5	N/A	This work
ZIF-386	$Zn(nbIM)_{0.85}(nIM)_{0.70}(IM)_{0.4}$	AFX	740	8	4.9	28.4 × 22.6	9.2	This work
ZIF-95	$Zn(cbIM)_2$	**poz**	1050	12	3.47	38.1 × 33.8	N/A	3
ZIF-100	$Zn_{20}(cbIM)_{39}(OH)$	**moz**	600	12	3.4	41.2	32.5	3
ZIF-408	$Zn(cbIM)_{1.86}(mIM)_{0.09}(OH)_{0.}$	**moz**	N/A	12	3.4	41.2	N/A	This work
ZIF-70	$Zn(nIM)_{0.87}(IM)_{1.13}$	GME	1730	12	13.2	22.6	N/A	10
ZIF-410	$Zn(cbIM)_{1.10}(aIM)_{0.90}$	GME	800[d]	12	5.2	22.6	8.9[d]	This work
ZIF-486	$Zn(nbIM)_{0.20}(mIM)_{0.65}(IM)_{1.1}$	GME	1180	12	6.0	22.6	9.9	This work
ZIF-412	$Zn(bIM)_{1.13}(nIM)_{0.62}(IM)_{0.25}$	**ucb**	1520	12	8.2	45.8	38.1	This work
ZIF-413	$Zn(mbIM)_{1.03}(nIM)_{0.64}(IM)_{0.3}$	**ucb**	1290	12	6.8	45.8	33.2	This work
ZIF-414	$Zn(nbIM)_{0.91}(mIM)_{0.62}(IM)_{0.4}$	**ucb**	1440	12	4.6	45.8	32.0	This work
ZIF-516	$Zn(mbIM)_{1.23}(bbIM)_{0.77}$	**ykh**	640	14	4.5	22.1	8.2	This work
ZIF-586	Zn(mbIM)(2-mbIM)	**ykh**	N/A	14	N/A	22.3	N/A	This work
ZIF-615	$Zn(cbIM)_{1.05}(4\text{-}nIM)_{0.95}$	**gcc**	770	18	14.5	27.2	11.4	This work
ZIF-725	$Zn(bbIM)_{1.35}(nIM)_{0.40}(IM)_{0.2}$	**bam**	720	24	22.5	39.0	31.1	This work
VPI-5	$Al_{18}P_{18}O_{72}$	VFI	N/A	18	12.0-13.0	16.3	N/A	25
ITQ-37	$Ge_{80}Si_{112}O_{400}H_{32}F_{20}$	ITV	690	30	4.3 × 19.3	25.0	10	26

[a]Aperture size (d_a) was estimated by fitting the largest sphere or ellipsoid into the largest ring with consideration of van der Waals radius of all atoms. [b]Cage size (d_c) was estimated with the shortest Zn/Al/Si/P···Zn/Al/Si/P distance across the cage. [c]Pore size distribution (PSD) were assessed by the QSDFT/GCMC fitting using the corresponding N_2 physisorption isotherms at 77 K, only peak maximums were shown here (SI). The pore sizes derived from PSD maximums are smaller compared to the d_c due to the presence of Im linkers. [d]The values are obtained from activated sample, for which we note subtle changes in the PXRD peak position attributable to the slight rotation of the IM linkers along the axis between two Zn metals.

Topology analysis. Seven of these new ZIFs have topologies belonging to known

zeolites (ZIF-303, CHA; ZIF-360 and 365, KFI; ZIF-376, LTA; ZIF-386, AFX; ZIF-410 and 486, GME, respectively), among which the KFI and AFX topologies were achieved for the first time in ZIFs. The other eight new ZIFs have tetrahedral topologies unrealized in zeolites (ZIF-408, **moz**; ZIF-412, 413, and 414, **ucb**; ZIF-516 and 586, **ykh**; ZIF-615, **gcc**; and ZIF-725, **bam**, respectively), and four of these (**ykh**, **gcc**, **bam**, and **ucb**) represent new topologies previously unknown in all porous crystals (Figure 2.88). According to common practice, zeolite topologies are given as capitalized symbols, while new topologies are denoted by a three-letter symbol in bold and lower-case.[27-28]

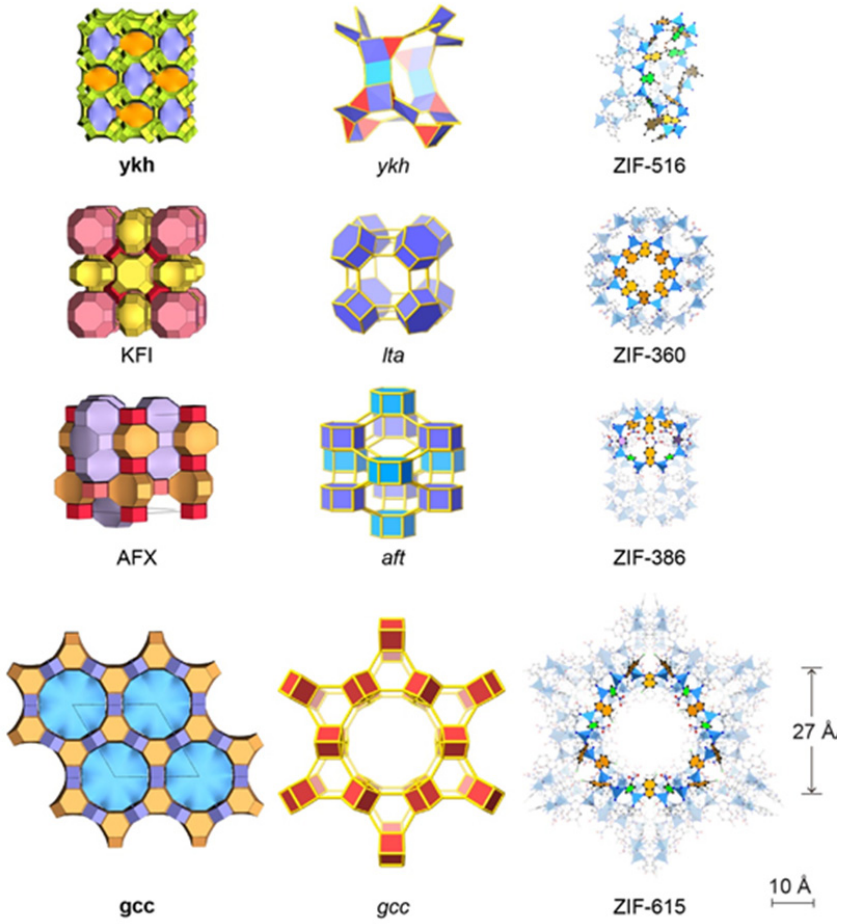

Figure 2.88 Topologies and crystal structures of KFI, ZIF-360; AFX, ZIF-386; **ykh**, ZIF-516; **gcc**, ZIF-615. Topologies are shown in natural tilings; the largest cages are presented with adjacent small cages; characteristic cages are shown with ball-and-stick for linkers (N, blue; C, dark; O, red; Cl, green; Br, orange, H, omitted for clarity) and blue tetrahedron for ZnN_4 units. Largest openings for each cage are highlighted.

Single-crystal structure illustration. The crystal structures of the fifteen new ZIFs were determined by single crystal X-ray diffraction techniques and those representing new topologies are shown in Figure 2.88-90, where the tiling, detailed cage topology, and crystal structure are shown (the largest ring highlighted). The cage name is denoted with a three-letter code in *italics*, and the symbol [...m^n...] means that the cage has n faces that are m-member rings.[29-30] For KFI and AFX ZIFs with 8 MR opening, the largest cages are *lta* [$4^{12}6^8$] and *aft* [$4^{15}6^2$] respectively; for **ykh** with 14 MR opening, the largest cage is *ykh*

[$3^4 4^8 10^2 14^2$] (Figure 2.88), for **gcc**, and **bam** ZIFs having one dimensional cylindrical channels with 18 MR and 24 MR opening, respectively, the cages are *gcc* [$8^6 18^2$] and *bam* [$4^6 8^6 24^2$] (Figure 2.88 and 2.89). The 24 MR opening in **bam** ZIF-725, comprised of 96 ring atoms, has an aperture size of 22.5 Å in diameter, which is the largest among all tetrahedral structures (state-of-the-art GME ZIF-70 with an 12 MR aperture and a size of 13.2 Å and zeolite VPI-5 of 12–13 Å)[10,25] (Table 2.1). Crystallographic aperture sizes of ZIFs are estimated with full occupancy of the bulky imidazolates due to disorderness of imidazolate, thus the real aperture size are underestimated and in fact are even larger. This is exemplified by the disorder of bulky bbIM and small IM in **bam** ZIF-725 as well as the disorder of bulky bIM and small IM in **ucb** ZIF-412 (Table 2.1).

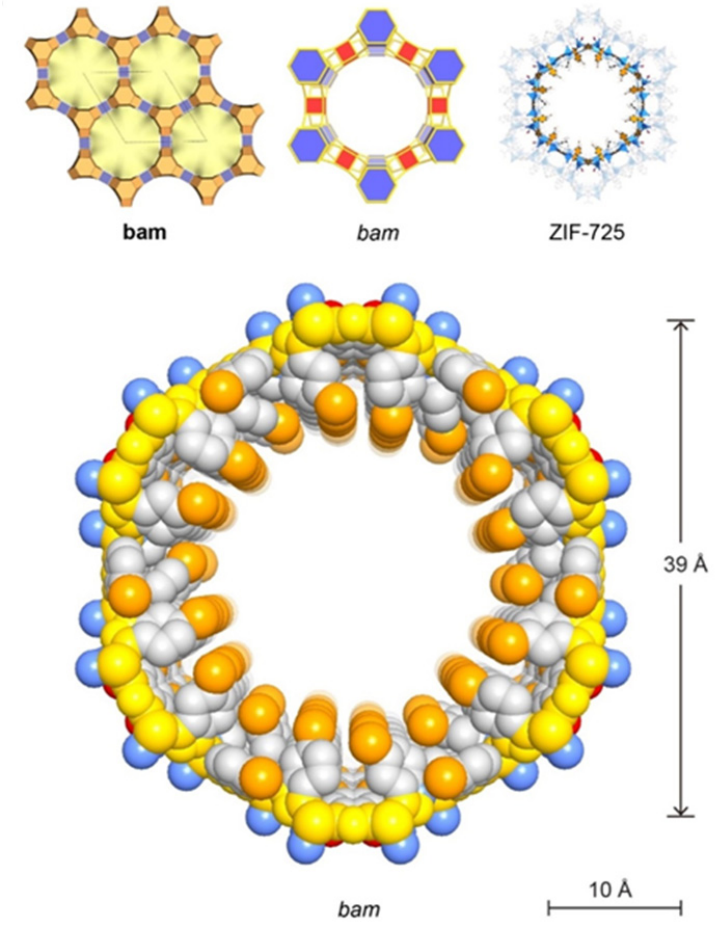

Figure 2.89 Topologies and crystal structures of **bam,** ZIF-725. Topologies are shown in natural tilings; the largest cages are presented with adjacent small cages; characteristic cages are shown with ball-and-stick for linkers (N, blue; C, dark; O, red; Cl, green; Br, orange, H, omitted for clarity) and blue tetrahedron for ZnN_4 units. Largest openings for each cage are highlighted. Space-filling views for the channel in **bam** ZIF (ZIF-725) are shown (zinc, blue; N, light blue; C, grey; O, red; Br, orange). The 24-MR aperture (**bam** ZIF-725, 96 atoms) is highlighted in yellow. Adapted with permission from ref 14. Copyright 2017 American Chemical Society

The three **ucb** ZIFs, ZIF-412, 413, and 414, all crystallized in the high-symmetry cubic system (space group $Fm\bar{3}m$) with a unit cell length and volume exceeding 72 Å and 376000 $Å^3$, respectively, are among the largest unit cell volumes ever reported for synthetic crystals (Figure 2.90).[3] These ZIFs have a hierarchical pore system with three type of cages: a cuboctahedral *lta* $[4^{12}6^8 8^6]$ with 8 MR opening; a tetrahedral *fau* $[4^{18}6^4 12^4]$ with 12 MR opening; and a giant truncated cuboctahedral *ucb* $[4^{36}6^{24}8^6 12^8]$ (shown in Figure 2.90), which is composed of 144 vertices (ZnN_4) and 216 edges (Im) and a cage size of 45.8 Å in diameter, representing the largest porous cage ever made in all tetrahedral structures (state-of-the-art ZIF-100 with a cage size of 41.2 Å, and zeolite ITQ-37 with a cage size of 25 Å)[3,26] (Table 2.1). Recently, a discrete molecular cage compound with a larger size was reported ($M_{48}L_{96}$, 54.8 Å of the shortest Pd···Pd distance across the cage); however, unlike the present ZIFs, investigation of its permanent porosity remains absent.[31]

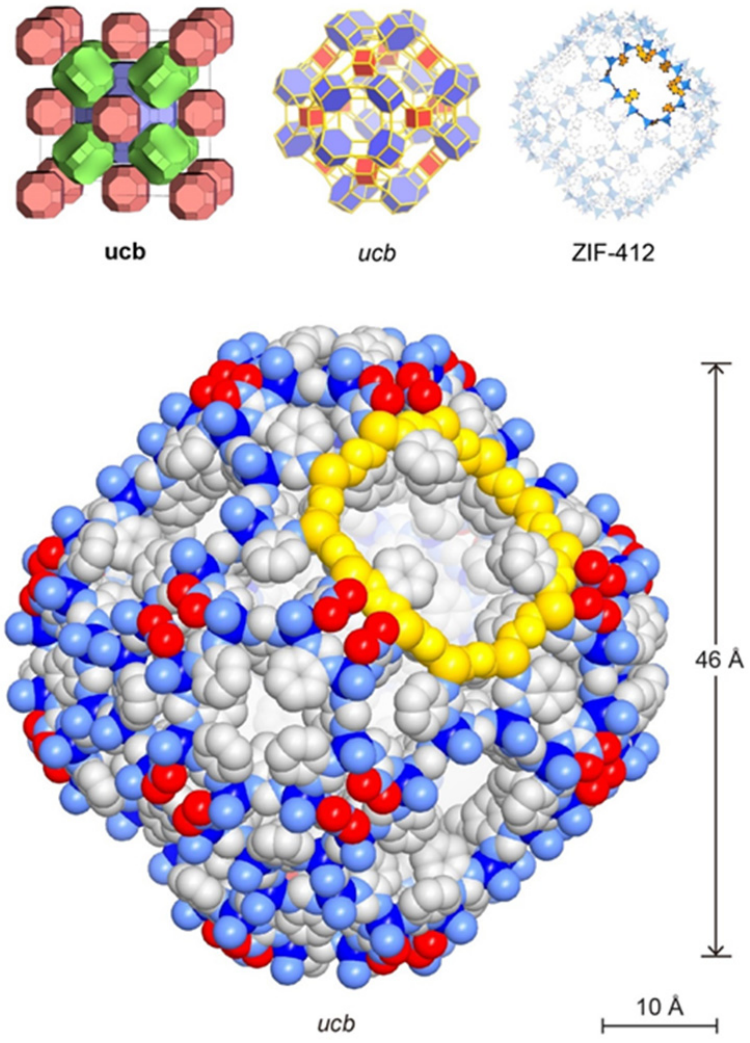

Figure 2.90 Topologies and crystal structures of **ucb**, ZIF-412. Topologies are shown in natural tilings; the largest cages are presented with adjacent small cages; characteristic cages are shown with ball-and-stick for linkers (N, blue; C, dark; O, red; H, omitted for clarity) and blue tetrahedron for ZnN_4 units. Largest openings for each cage are highlighted. Space-filling

view for the largest cage in **ucb** ZIFs (illustrated by ZIF-412) is shown, zinc, blue; N, light blue; C, grey; O, red. The 12 MR opening (**ucb** ZIF-412, 48 atoms) are highlighted in yellow. Adapted with permission from ref 14. Copyright 2017 American Chemical Society

All the new topologies made here have cages with sizes larger than 2 nm, suggesting the usefulness of the strategy.

TGA and porosity characterization. The family of ZIFs reported here show high thermal stability in air up to 350 °C, as confirmed by thermal gravimetric analysis (TGA). The pore size distribution derived from N_2 gas adsorption study reveals a size of *ca.* 38.1 Å in diameter (peak maximum) of the *ucb* cages in ZIF-412 (Table 2.1), far exceeding the previous record held by ZIF-100 with a size of *ca.* 32–33 Å and zeolite ITQ-37 (*ca.* 10 Å). The gas N_2 adsorption isotherms at 77 K also gave Brunauer-Emmett-Teller (BET) surface areas in the range of 640–1520 m^2/g for the majority of ZIFs (Table 2.1). The **ucb** and **bam** ZIFs exhibited Type IV isotherms characteristic of mesopores, which is in agreement with their crystal structures. The **ucb** ZIFs reveal much higher BET surface areas (1290–1520 m^2/g), while the **bam** ZIF shows BET of 718 m^2/g, owing to bulky bbIM linker.

2.4 Conclusions

In this Chapter, the use of multiply functionalized imidazolate is demonstrated useful to make ZIFs of large pores and apertures with topologies known in zeolites and hypothetical ones yet to be achieved. Indeed, this strategy has led to ZIFs with the largest units cells ever made, and the largest pore opening realized in a ZIFs. The success in the use of multivariate imidazolate linkers to make exceptional ZIFs, which cannot be made in any other way, is a clear demonstration of how precise control of the combination of imidazolate with different functionalities can have profound and fruitful impact on the chemistry of porous crystals. I anticipate the synthetic utility of this approach for producing more complex structures.

2.5 Acknowledgments

Support for synthesis and characterization by BASF SE (Ludwigshafen, Germany), hydrocarbon sorption by U.S. Department of Defense, Defense Threat Reduction Agency (DTRA). Researchers at Wuhan University (H. D., Q. L. and H. C.) were supported by the 1000 Talent Plan of China, National Natural Science Foundation of China (21471118, 91545205 and 91622103) and National Key Basic Research Program of China (No. 2014CB239203). I thank Simon, J. Teat and Kevin, J. Gagnon (Advance Light Source, Lawrence Berkeley National Laboratory, U.S.A.) for support during the single-crystal diffraction data collection at the beamline 11.3.1; Dr. H. Furukawa, Mr. Eugene Kapustin for assistance and advice in gas sorption experiments; Prof. Hans-Beat Bürgi (University of Zurich, Switzerland), Prof. Osamu Terasaki (Stockholm University, Sweden) for their helpful suggestions in both X-ray diffraction studies and data analysis; Prof. M. O'Keeffe (Arizona State University, U.S.A.) for useful discussions on topology. Support from Advanced Light Source by the Director, Office of Science, Basic Energy Sciences, of the U.S. Department of Energy under Contract No. DE-AC02-05CH11231; supports from single crystal XRD beam line BL15U, BL17U1, and BL17B in Shanghai Synchrotron Radiation (SSRF), and CheXray in UC Berkeley (NIH Shared Instrumentation Grant S10-RR027172) are acknowledged. Supports from the Recruitment Program for Young Professionals & NSFC 21522105 are acknowledged. Department of Energy, Office of Science, Office of Basic Energy Sciences

under Award No. DE-SC0001015, and was further supported in its initial stages by the Sustainable Products & Solutions Program at the University of California, Berkeley.

2.6 References

[1] Park, K. S.; Ni, Z.; Côté, A. P.; Choi, J. Y.; Huang, R. D.; Uribe-Romo, F. J.; Chae, H. K.; O'Keeffe, M.; Yaghi, O. M. *Proc. Natl. Acad. Sci. U.S.A.* **2006**, *103*, 10186.
[2] Phan, A.; Doonan, C. J.; Uribe-Romo, F. J.; Knobler, C. B.; O'Keeffe, M.; Yaghi, O. M. *Acc. Chem. Res.* **2010**, *43*, 58.
[3] Wang, B.; Côté, A. P.; Furukawa, H.; O'Keeffe, M.; Yaghi, O. M. *Nature* **2008**, *453*, 207–211.
[4] Brown, A. J.; Brunelli, N. A.; Eum, K.; Rashidi, F.; Johnson, J. R.; Koros, W. J.; Jones, C. W.; Nair, S. *Science* **2014**, *345*, 71.
[5] Baerlocher, C. & McCusker, L. B. *Database of Zeolite Structures*, http://www.iza-structure.org/databases.
[6] Furukawa, H.; Cordova, K. E.; O'Keeffe, M.; Yaghi, O. M. *Science*, **2013**, *341*, 1230444.
[7] Foster, M. D. & Treacy, M. M. J. *Atlas of Prospective Zeolite Structures*, http://www.hypotheticalzeolites.net (2010).
[8] Férey, G.; Mellot-Draznieks, C.; Serre, C.; Millange, F.; Dutour, J.; Surblé, S.; Margiolaki, I. *Science* **2005**, *309*, 5743.
[9] Hayashi, H.; Côté, A. P.; Furukawa, H.; O'Keeffe, M.; Yaghi, O. M. *Nature Mater.* **2007**, *6*, 501.
[10] Banerjee, R.; Phan, A.; Wang, B.; Knobler, C.; Furukawa, H.; O'Keeffe, M.; Yaghi, O. M. *Science* **2008**, *319*, 939.
[11] Wu, T.; Bu, X.; Zhang, J.; Feng, P. *Chem. Mater.* **2008**, *20*, 7377.
[12] Nguyen, N. T. T.; Furukawa, H.; Gándara, F.; Trickett, C. A.; Jeong, H. M.; Cordova, K. E.; Yaghi, O. M. *Angew. Chem. Int. Ed.* **2014**, *40*, 10645.
[13] Shi, Q.; Xu, W.-J.; Huang, R.-K.; Zhang, W.-X.; Li, Y.; Wang, P.; Shi, F.-N.; Li, L.; Li, J.; Dong, J. *J. Am. Chem. Soc.* **2016**, *138*, 16232.
[14] Yang, J.; Zhang, Y.; Liu, Q.; Trickett, C. A.; Gutierrez-Puebla, E.; Monge, M. Á.; Cong, H.; Aldossary, A.; Deng, H.; Yaghi, O. M. *J. Am. Chem. Soc.* 2017, *139*, 6448–6455.
[15] Thorn, A.; Dittrich, B.; Sheldrick, G. M. *Acta Cryst. A* **2012**, *68*, 448.
[16] Bruker. *APEX2*. (Bruker AXS Inc., Madison, Wisconsin, U.S.A. 2010).
[17] Sheldrick, G. M. *Acta Cryst. A* **2008**, *64*, 112–122.
[18] CrysAlis Software System, version 171.37.33; Agilent Technologies: Santa Clara, CA, 2014.
[19] Dolomanov, O. V.; Bourhis, L. J.; Gildea, R. J.; Howard, J. A. K.; Puschmann, H. J. *Appl. Cryst.* **2009**, *42*, 339.
[20] Rees, B.; Jenner, L. B.; Yusupov, M. *Acta Cryst. D* **2005**, *61*, 1299.
[21] Spek, A. L. *Acta Cryst. D* **2009**, *65*, 148.
[22] Thommes, M.; Kaneko, K.; Neimark, A. V.; Olivier, J. P.; Rodriguez-Reinoso, F.; Rouquerol, J.; Sing, K. S. W. *et al.*, *Pure Appl. Chem.* **2015**, *87*, 1051.
[23] Ravikovitch, P. I.; Neimark, A. V. *Langmuir* **2006**, *22*, 11171.
[24] Walton, K. S.; Snurr, R. Q. *J. Am. Chem. Soc.* **2007**, *129*, 8552.
[25] Davis, M. E.; Saldarriaga, C.; Montes, C.; Garces, J.; Crowdert, C. *Nature* **1988**, *331*, 698.
[26] Sun, J.; Bonneau, C.; Cantín, Á.; Corma, A.; Díaz-Cabañas, M. J.; Moliner, M.; Zhang, D.; Li, M.; Zou, X. *Nature* **2009**, *458*, 1154.

[27] Alexandrov, E. V.; Blatov, V. A.; Kochetkov, A. V.; Proserpio, D. M. *CrystEngComm* **2011**, *13*, 3947.
[28] Banerjee, R.; Furukawa, H.; Britt, D.; Knobler, C.; O'Keeffe, M.; Yaghi, O. M., *J. Am. Chem. Soc.* **2009**, *131*, 3875.
[29] Blatov, V. A.; Delgado-Friedrichs, O.; O'Keeffe, M.; Proserpio, D. M. *Acta Crystallogr. A* **2007***, 63*, 418.
[30] Anurova, N.; Blatov, V. A.; Ilyushin, G. D.; Proserpio, D. M. *J. Phys. Chem. C* **2010**, *114*, 10160.
[31] Fujita, D.; Ueda, Y.; Sato, S.; Mizuno, N.; Kumasaka, T.; Fujita, M. *Nature* **2016**, *540*, 563–566.

Chapter 3: General Principles for the Structural Design of Zeolitic Imidazolate Frameworks

3.1 Introduction

Over the past decade major research efforts have been devoted to the challenge of the designed synthesis of ZIFs. Early explorations relied largely on a trial-and-error approach.[1-2] It was found that the functionalities on the imidazolate building units have a profound impact on resulting structure type through steric or hydrogen-bonding based link-link interactions.[3-4] A high-throughput synthesis was developed to improve the efficiency of screening.[5] Templates were also employed and new ZIFs were obtained with bulky molecules.[6-7] While the trial-and-error approach has yielded the large family of ZIF structures known today, it is intrinsically limited with regard to efficient discovery of new topologies and structures due to the lack of guided synthesis.

The high-throughput method used robots to automatically mix reactants in varying concentrations into microplate wells followed by heating the mixtures; twenty-five different ZIF crystals were synthesized out of 9600 microreactions, among which five new topologies were discovered.[5] This method is time and cost saving, but has not answered the scientific question: What underlying principles govern the assembly of ZIFs and how can we guide the synthesis ZIF structures?

One outcome of the high-throughput synthesis is the introduction of additional degrees of complexity into ZIFs by employing mixtures of imidazolates. The authors synthesized ZIF-68 with GME topology by reticulating 2-nitroimidazole (nIM) and benzmidazole (bIM) with zinc ion. In contrast, reticulating only nIM with zinc ions will result in ZIF-67 with SOD topology, and ZIF-11 with RHO topology is formed from pure bIM. This phenonmenon is quite different compared to carboxylate MOFs, where altering the body of a linker but keeping geometry and connectivity identidal yields isoreticular multivariate (MTV) MOFs will rather than affecting a change of topology.[8] The result indicated that the topology of ZIFs is highly dependent on the linker functionalities.

3.2 Results and Discussion

Close examination of the ZIFs reported previously and here revealed a striking commonality: the 2- and 4,5-positions of Im (imidazolate) linkers tend to point into the 4 MR and ≥8 MR, respectively. Both positions are usually found in the 6 MR because this is the ring sharing the 4 MR with ≥8 MR (Figures 3.1-3.15). These Im positions arrangement is generally followed; however, exceptions arise when the 4 MR is adjacent to another 4 MR through sharing of edges as for example in ZIFs of the MER topology, where the 2- and 4,5-positions have to point into a 4 MR.

The rings and their compositions in 15 topologies with the largest cages are analyzed here.[9] A typical ZIF from a topology are used for demonstration. Small rings (3 and 4 MR) are shown as their assemblies in the structure to illustrate the influence from adjacent small rings, 6 MR and larger rings (8, 12, 14, 18, and 24 MR) are shown on their own, and ring composition in the largest cage are demonstrated. The following results show that in all ZIFs with large pore, the 2-positions of Im linkers tend to point into the 4 MR (or 3 MR) and 4,5-positions of Im linkers tend to point into the rings ≥8 MR. Both the 2- and 4,5- positions are usually found in the 6 MR.

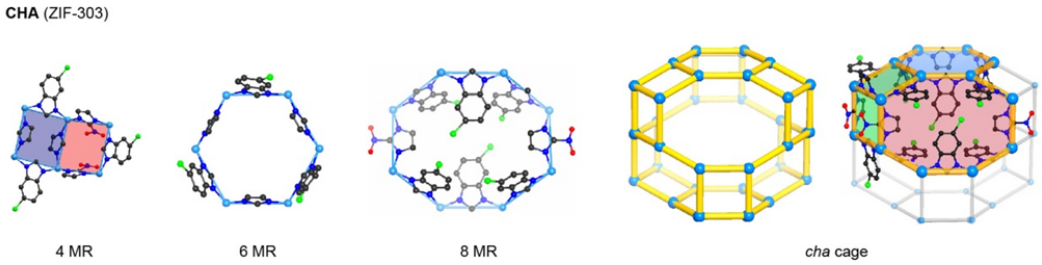

Figure 3.1 Rings and the *cha* cage in **CHA ZIF-303**, Zn in cyan, C in black, N in blue, O in red, Cl in green, H is omitted for clarity. Note that IM and cbIM are position disordered.

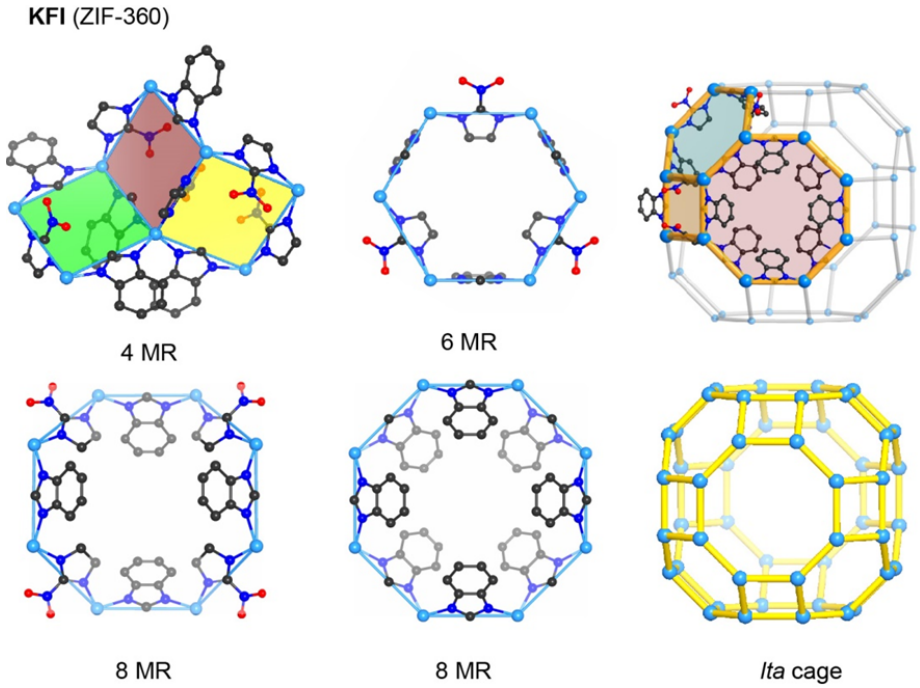

Figure 3.2 Rings and the *lta* cage in **KFI ZIF-360**, Zn in cyan, C in black, N in blue, O in red, H is omitted for clarity. Note that IM and bIM are position disordered.

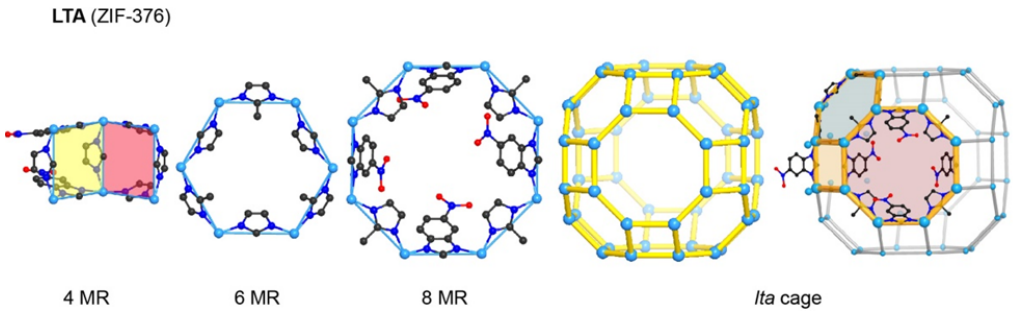

Figure 3.3 Rings and the *lta* cage in **LTA ZIF-376**, Zn in cyan, C in black, N in blue, O in red, H is omitted for clarity. Note that IM and nbIM are position disordered.

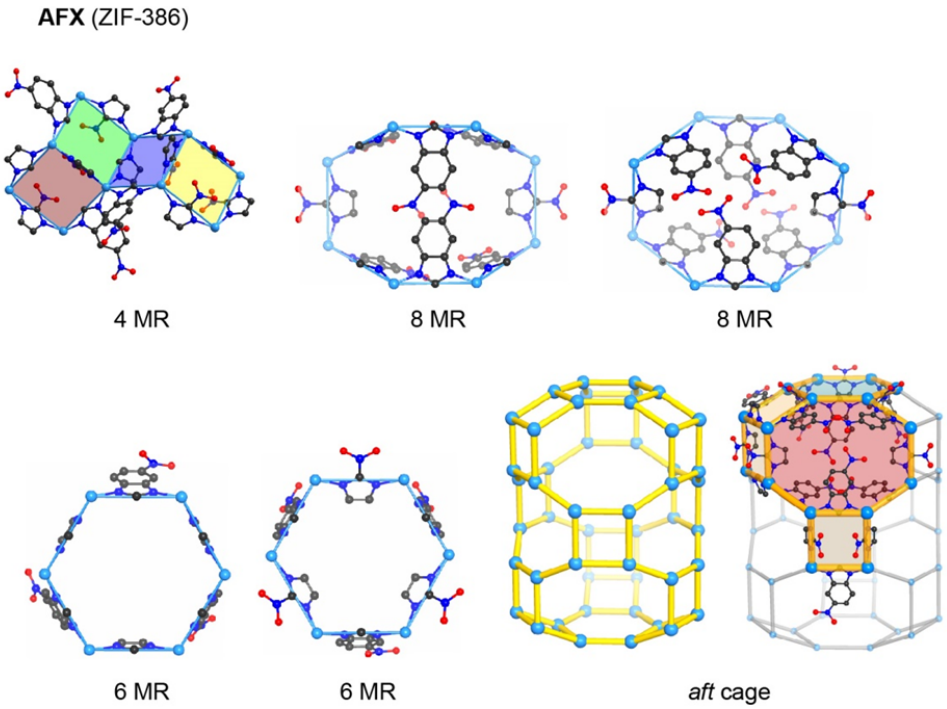

Figure 3.4 Rings and the *aft* cage in **AFX ZIF-386**, Zn in cyan, C in black, N in blue, O in red, H is omitted for clarity. Note that IM and nbIM are position disordered.

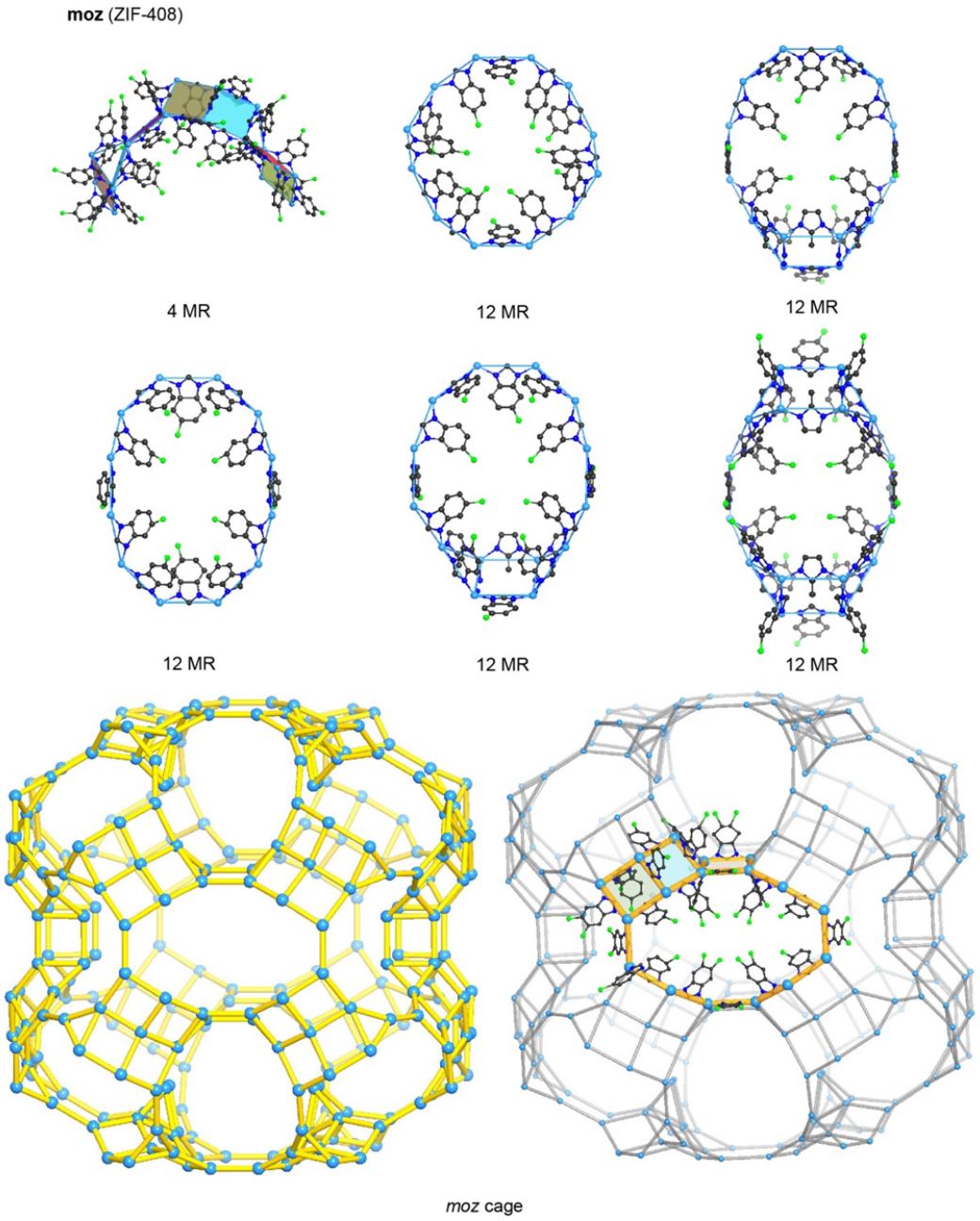

Figure 3.5 Rings and the *moz* cage in **moz** ZIF-408, Zn in cyan, C in black, N in blue, O in red, Cl in green, H is omitted for clarity.

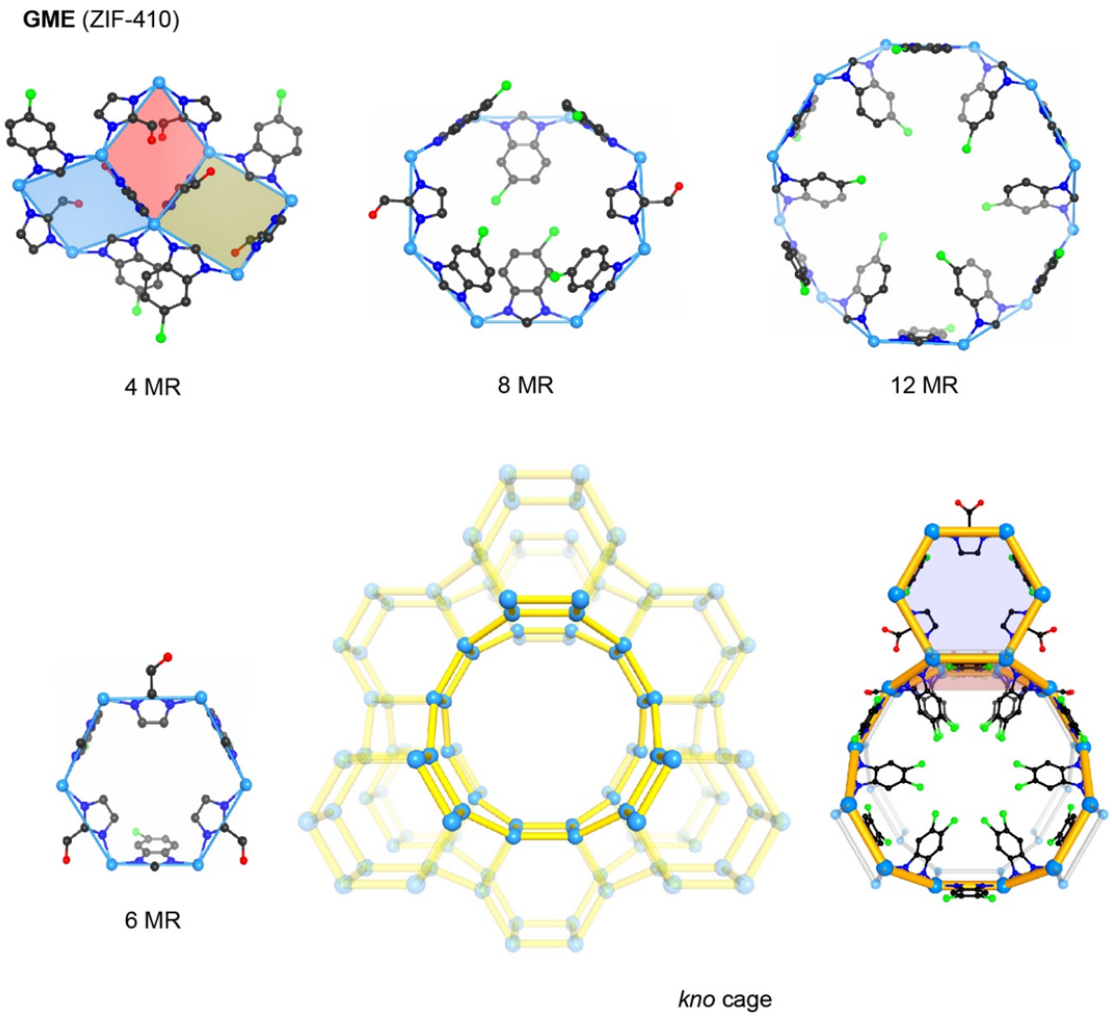

Figure 3.6 Rings and the *kno* cage in GME ZIF-410, Zn in cyan, C in black, N in blue, O in red, Cl in green, H is omitted for clarity. GME-ZIF-68 has the same linker arrangement as GME ZIF-410 except the bIM replaces cbIM.

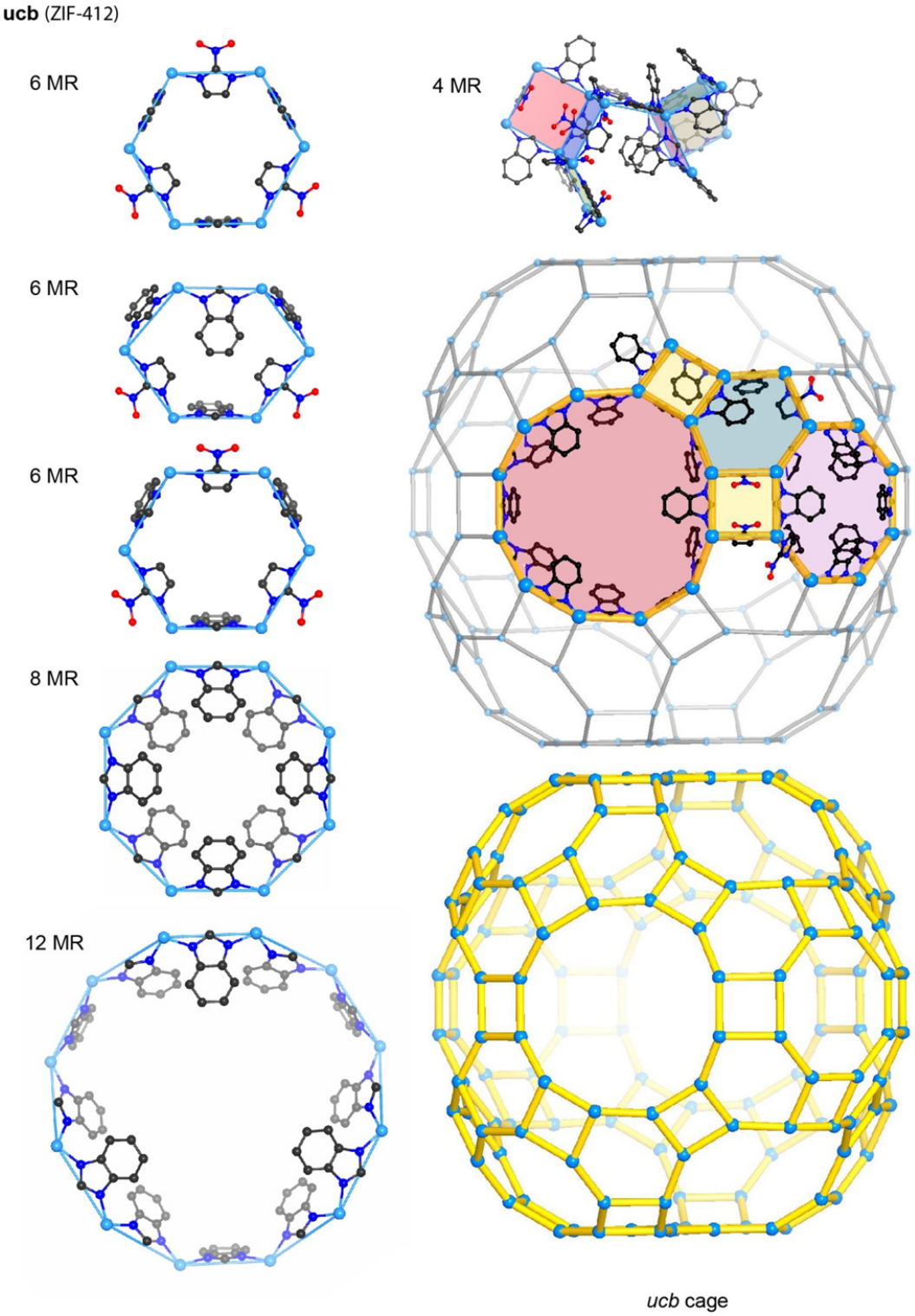

Figure 3.7 Rings and the *ucb* cage in **ucb** ZIF-412, Zn in cyan, C in black, N in blue, O in red, H is omitted for clarity. Note that IM and bIM are position disordered.

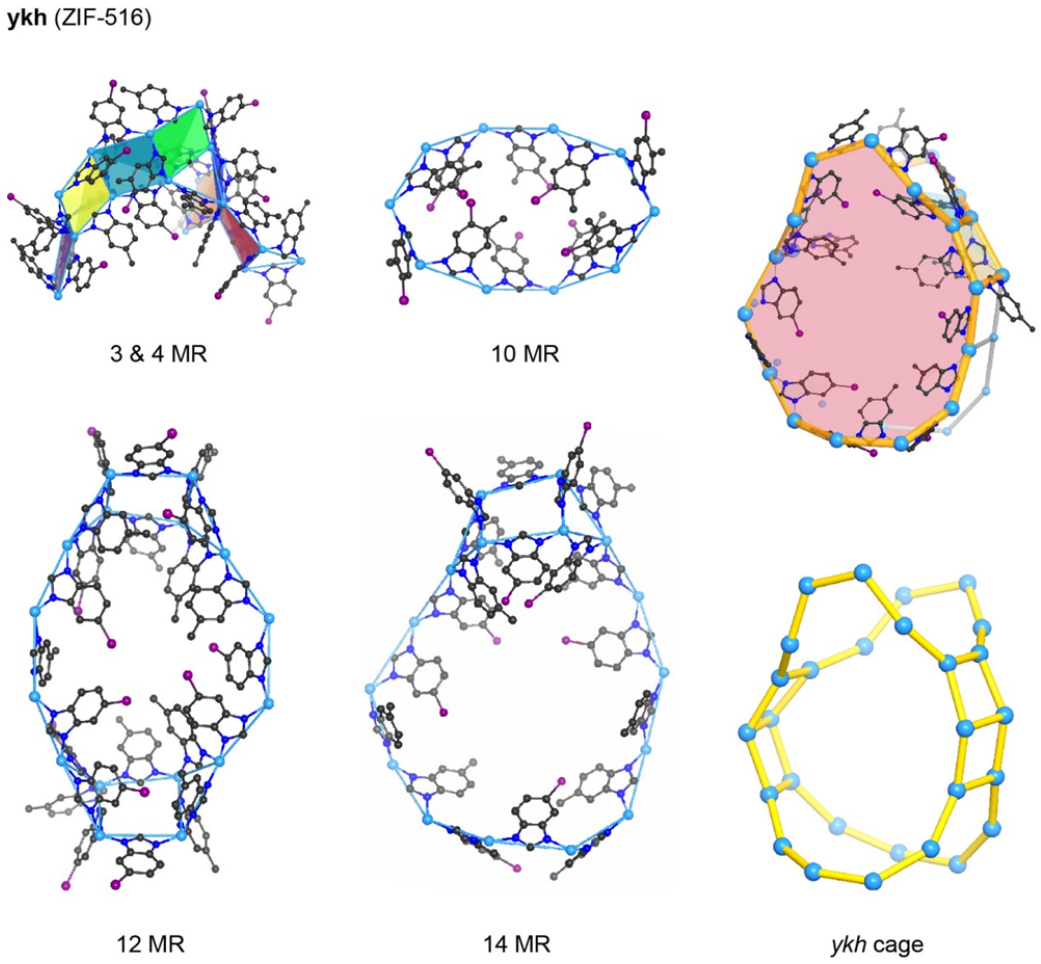

Figure 3.8 Rings and the *ykh* cage in **ykh** ZIF-516, Zn in cyan, C in black, N in blue, Br in violet, H is omitted for clarity. Note that mbIM and bbIM are position disordered.

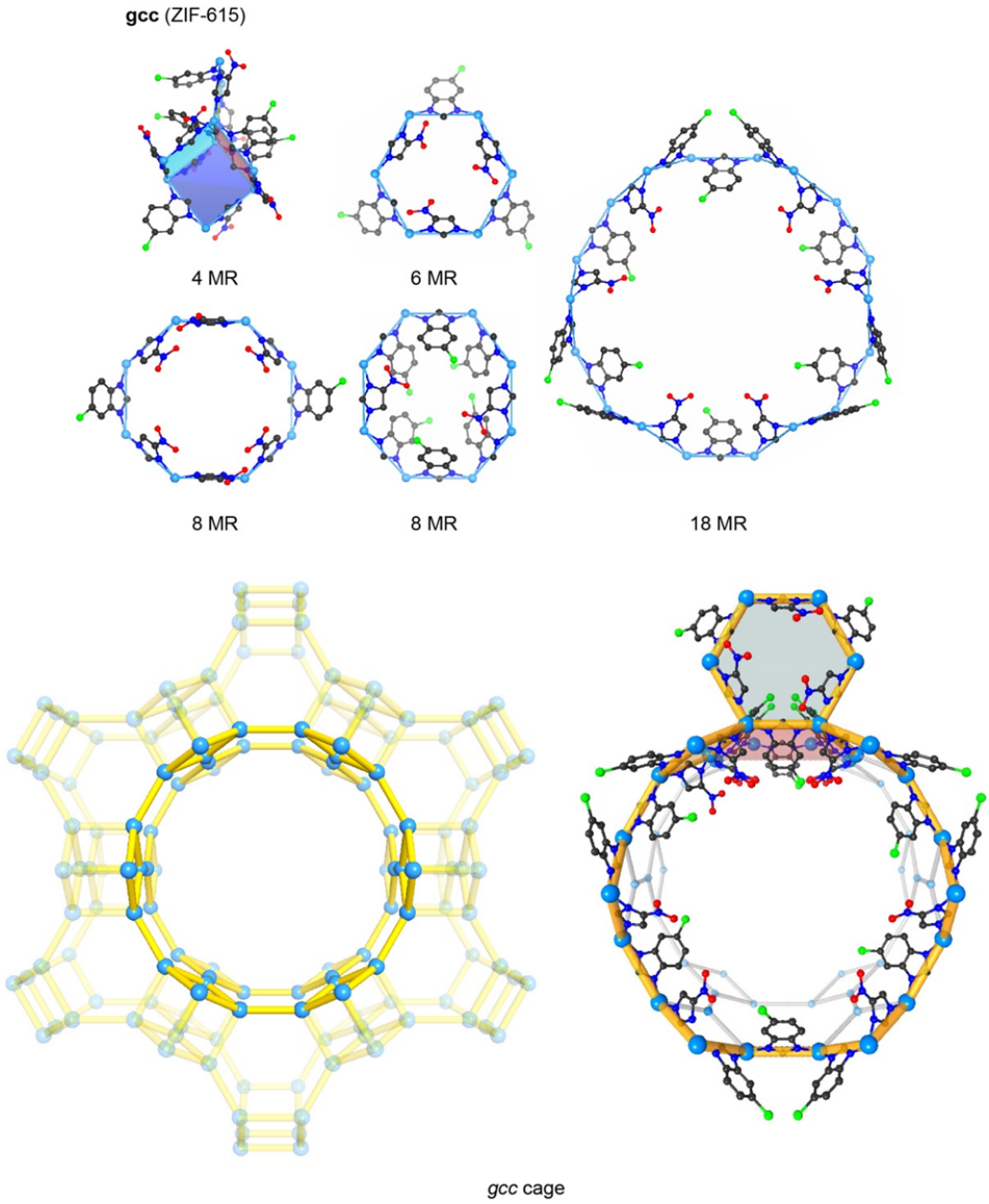

Figure 3.9 Rings and the *gcc* cage in **gcc** ZIF-615, Zn in cyan, C in black, N in blue, O in red, Cl in green, H is omitted for clarity. Note that in the 18 MR and one of the 8 MR here, several cbIM have their 4,5-positions pointing outside of the ring, this is because their 4,5-positions are pointing to the adjacent 8 MR (these edges are shared by two large rings).

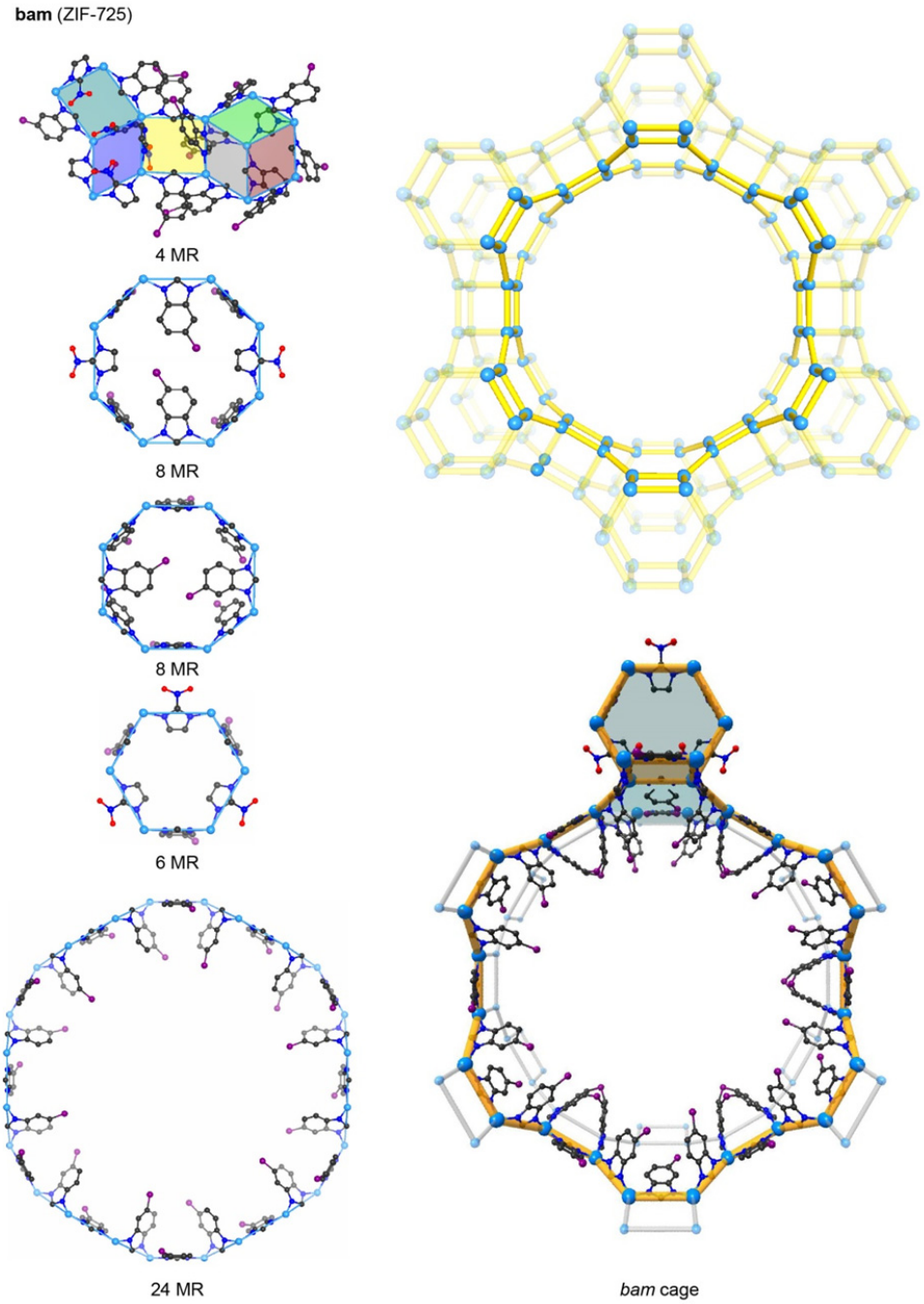

Figure 3.10 Rings and the *bam* cage in **bam** ZIF-725, Zn in cyan, C in black, N in blue, O in red, Br in violet, H is omitted for clarity. Note that IM and bbIM are position disordered.

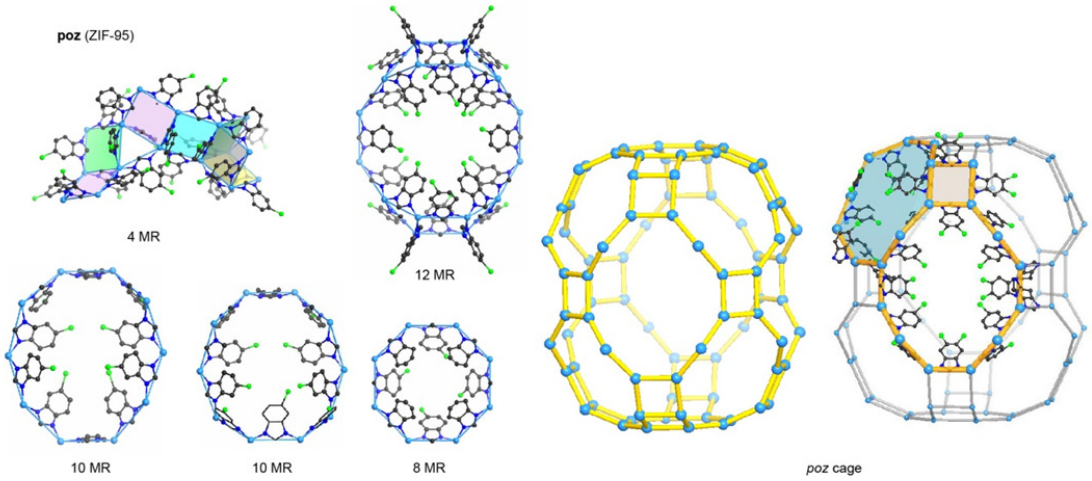

Figure 3.11 Rings and the *poz* cage in **poz** ZIF-95, Zn in cyan, C in black, N in blue, Cl in green, H is omitted for clarity.

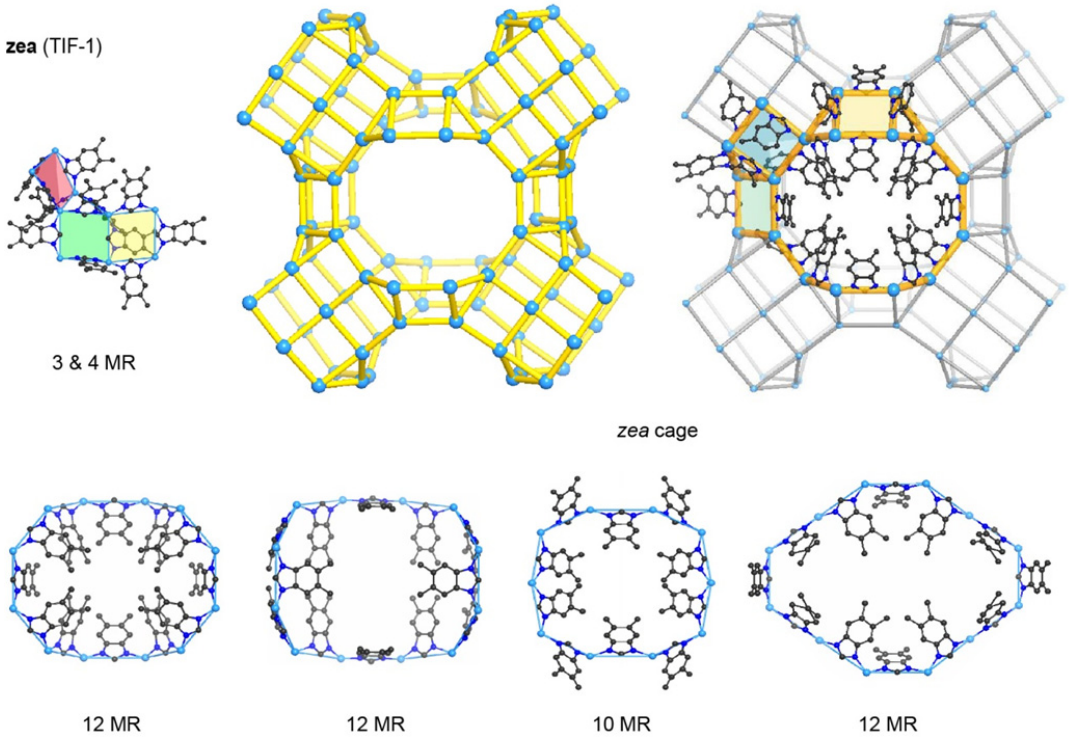

Figure 3.12 Rings and the *zea* cage in **zea** TIF-1, Zn in cyan, C in black, N in blue, H is omitted for clarity. Note that in the 10 MR and one of the 12 MR here, several dmbIM have their 4,5-positions pointing outside of the ring, this is because their 4,5-positions are pointing to the adjacent 12 MR (these edges are shared by two large rings).

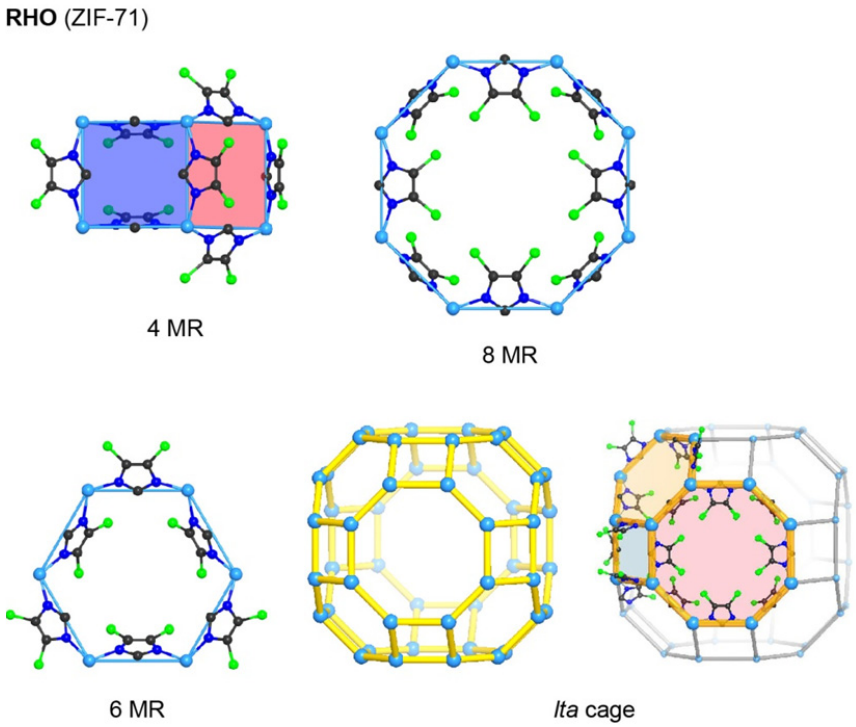

Figure 3.13 Rings and the *lta* cage in RHO ZIF-71, Zn in cyan, C in black, N in blue, Cl in green, H is omitted for clarity.

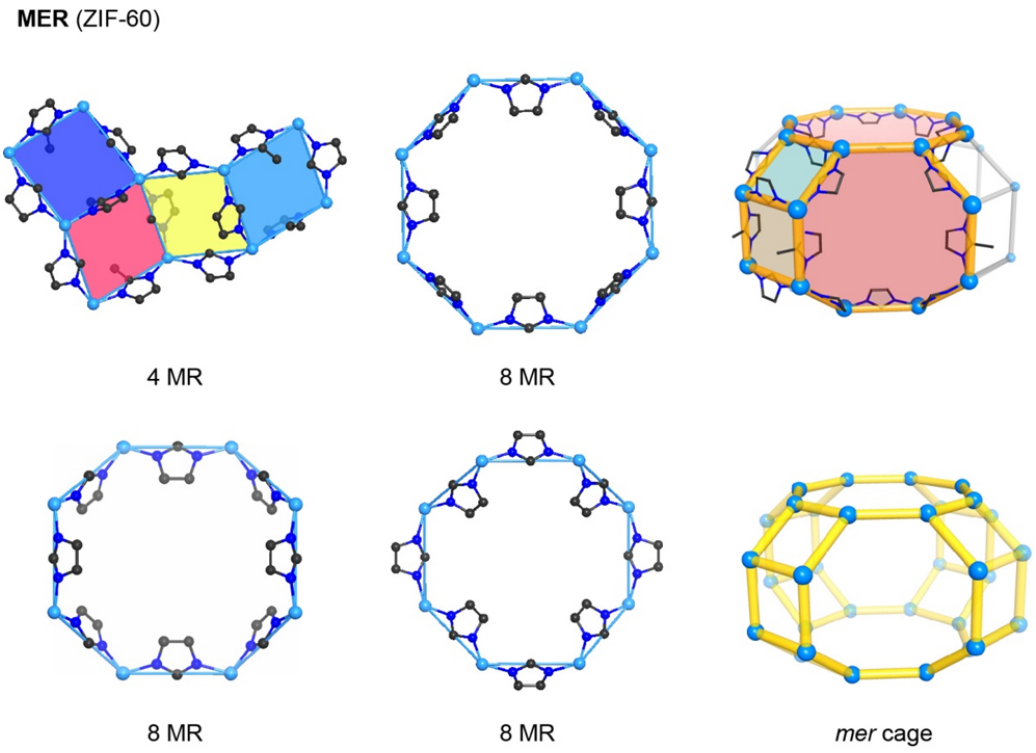

Figure 3.14 Rings and the *mer* cage in MER ZIF-60, Zn in cyan, C in black, N in blue, H is omitted for clarity. Note that in one of the 8 MR here, several IM have their 4,5-positions pointing outside of the ring, this is because their 4,5-positions are pointing to the adjacent 8 MR (these edges are shared by two 8 MR).

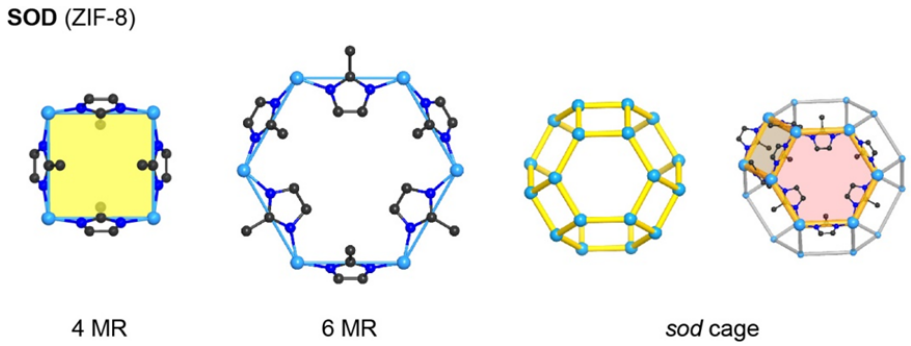

Figure 3.15 Rings and the *sod* cage in SOD ZIF-8, Zn in cyan, C in black, N in blue, H is omitted for clarity. 2-positions of mIM point into 4 MR. Parts 2- positions and the rest of 4,5- positions of mIM point into 6 MR.

One may think what leads to this commonality? The answer is pretty simple: it is the size difference (steric hindrance) of the functionalities on an Imidazolate. Large ring has a large inner space and thus can accommodate bulkier functional groups while a small ring can only accommodate small functional groups due to the limited space. Typically, the 2-position functionality of imidazolate is less sterically hindered compared to the 4,5-positions (even for the pure non-substituted imidazole), therefore, the 2-position prefers to stay in a small ring, and 4,5-position prefers to stay in a large ring.

The fact that the 4,5-position points into larger rings, meant that ZIFs with much larger rings, and therefore larger pore openings could be potentially achieved by introducing bulkiness in the Im linkers at that specific position. In principle, it might be possible to make large rings by adding a very bulky group to the 2-position; however, it is far more effective to introduce such bulkiness at the 4,5-position and thus this was the focus of our work. Indeed, two relevant distances (l_2 and $l_{4,5}$) are determined for Im (Figure 3.16) and considered the longer of these (4,5-position) (l) for the linkers employed in our study. The steric index (δ) is defined as the product of the van der Waals volume (V) of Im and l, and it is a measure of the size and shape of the Im (Figure 3.16 and Table 3.1). The larger the steric index is, the bulkier the functional group is.

Table 3.1 Common imidazolate linkers and their δ values

Imidazolate linker	**Abbr.**	l_{max}^{*}/Å	**vdW**	δ/Å^4
Imidazole	HIM	4.09	60.7	248
2-chloroimidazole	HclIM	4.09	75.3	308
2-methylimidazole	HmIM	4.09	78.0	319
2-bromoimidazole	HbrIM	4.09	79.1	324
2-imidazolecarboxaldehyde	HaIM	4.09	80.0	327

2-nitroimidazole	HnIM	4.09	84.9	347
2-ethylimidazole	HeIM	4.09	94.3	386
4-methylimidazole	4-HmIM	5.04	78.2	394
4-cyanoimidazole	4-HcnIM	5.66	77.8	440
4,5-dichloroimidazole	HdclIM	5.17	89.1	461
4,5-dimethylimidazole	HdmIM	5.04	94.5	476
4-nitroimidazole	4-HnIM	5.89	84.9	500
2-propylimidazole	HprIM	4.56	111.7	509
4-cyano-5-aminoimidazole	HcaIM	5.66	90.1	510
4-methyl-5-carboxaldehydeimidazole	HmcIM	5.39	97.2	524
4-methyl-5-hydroxymethylimidazole	HmhmIM	5.35	102.7	549
4-methyl-5-nitroimidazole	HmnIM	5.88	102	600
Purine	HPur	6.48	95.4	618
4-azobenzimidazole	4-HabIM	6.53	99.6	650
5-azobenzimidazole	5-HabIM	6.54	99.8	653
benzimidazole	HbIM	6.55	103.6	679
2-methylbenzimidazole	2-HmbIM	6.55	121.2	794
5-methylbenzimidazole	HmbIM	7.51	121.5	913
5-chlorobenzimidazole	HcbIM	7.69	119.0	915
5-bromobenzimidazole	HbbIM	7.93	123.5	979
5,6-dimethylbenzimidazole	HdmbIM	7.51	138.3	1039
5-nitrobenzimidazole	HnbIM	8.33	127.7	1064

* l_{max} and vdW volume (Connolly probe radius of zero) were calculated using software Materials Studio.

The steric effects of different imidazolate can now be compared quantitatively with the steric index. Based on this, Upon going over all known ZIF structures and ZIFs made herein, three general principles are proposed which can be used for guiding the synthesis of ZIFs. These principles are termed as ‘ring-directed synthesis’ as the structural rings can be considered as a bridge to cnnect starting materials and final structures.

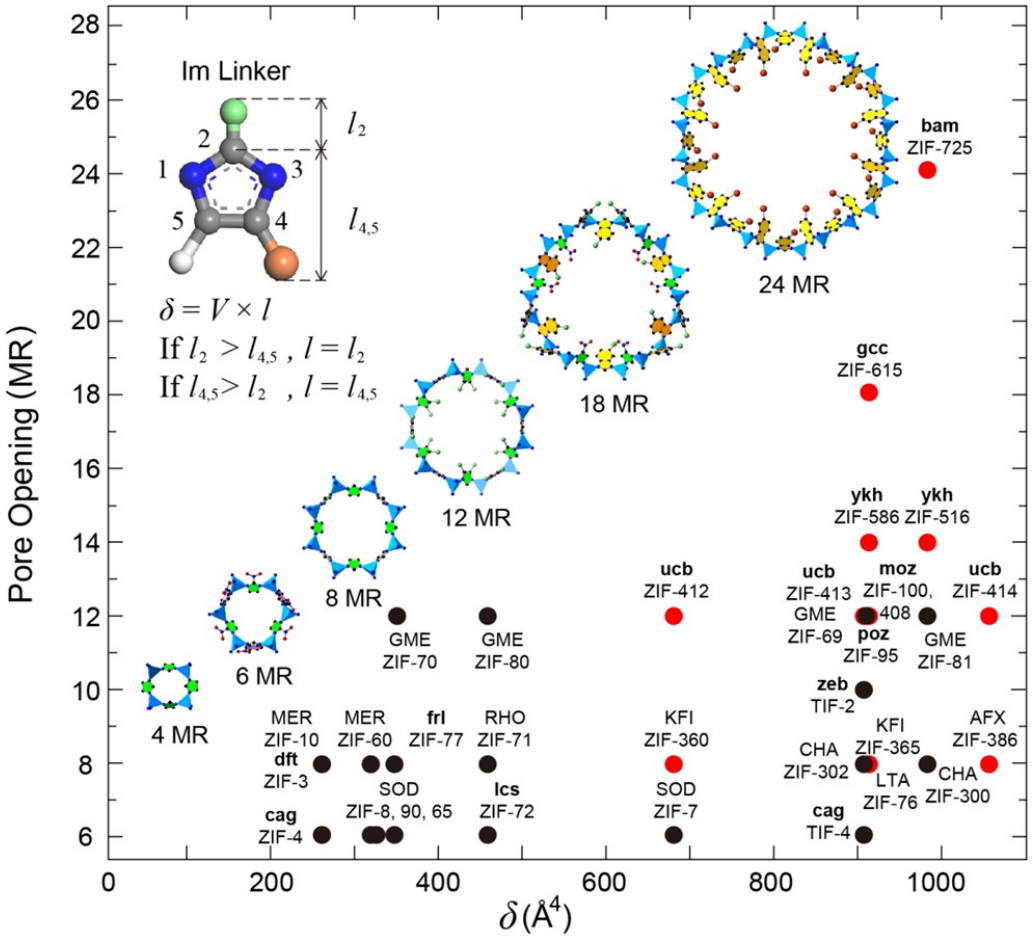

Figure 3.16 Correlation between the δ values of Im linkers with the largest ring sizes in ZIFs where progressively larger ring sizes (pore opening) are made in ZIFs by increasing Im linker' size and shape (steric index, δ). The corresponding rings are displayed in ball-and-stick representation with the ring size shown (N, blue; C, dark; O, red; Cl, green; Br, orange; and ZnN_4 units, light blue tetrahedral. H atoms are omitted for clarity). Several ZIFs made by bulky solvent templating approach are not plotted [Five topologies (**zni**, **zni-b**, **zec**, CAN, and AFI) have rings larger than 8 MR but are excluded for analysis here. The reasons are given as following: (1) the 12 MR in **zni** and **zni-b** are both collapsed (only 7.8 Å in diameter, compared to 15.5 Å of regular 8 MR, size refers to the shortest Zn···Zn distance across the ring), suggesting the linker itself can't support such large ring because of its small steric hindrance; (2) the formation of 10 and 12 MR (13.4 Å, and 21.7 Å) in **zec**, CAN and AFI relies on the use of bulky solvent as structural directing agent (template).[10-11] It is the bulky solvent template and the imidazolate linker together supporting the large ring, while a system with only the linker cannot. All above cases suggest that the intrinsic character of the specific linker used do not allow the formation of stable and open large rings, and thus these cases are excluded. However, it is expected that these ZIFs would still follow the rule, but just a larger ring size would be achieved when implementing same linker compared to the system without template. Also upon increasing the solvent template size, the ring size shall also increase (illustrated by 10 MR in zec templated by *N,N*-Diethylformamide and 12 MRs in CAN and

AFI templated by an even bulkier *N,N*-Dibutylformamide). This is simply because the bulky solvent molecules provide some steric hindrance to help the linkers to form a larger ring, lowering down the steric requirement for the linkers. But templating is not always working and the fruitfulness is limited due to the intrinsic size limitation and the narrow choice of bulky solvents]. Inset upper left, schematics of Im linker including the definition of δ. Molecular structures of Im linkers discussed in here shown along with their respective δ values. Red dots represent structures reported here, and black dots represent already reported structures. Reprinted with permission from ref 9. Copyright 2017 American Chemical Society

Principle I: Ring sizes. Our new series of ZIFs and those previously reported are shown on a plot of the largest ring size *vs.* the largest δ presented in a ZIF structure where a clear correlation is observed between these two parameters. It is clear that high steric index enabled me to achieve ZIFs with large (the highest ever reported) ring size [14 MR in ZIF-516 and 586 (**ykh**); 18 MR in ZIF-615 (**gcc**); and 24 MR in ZIF-725 (**bam**)], far exceeding the previous 12 MR record held by GME, CAN, AFI, **zea**, **poz**, and **moz** ZIFs; and the largest pore opening [14.5 Å in ZIF-615 (**gcc**), and 22.5 Å in ZIF-725 (**bam**)], far exceeding the previously record held by GME and AFI ZIFs (13.2 Å) (Figure 3.16 and Table 2.1).[4,5,10,11] It is worthy of note that although the increment of linker bulkiness will influence the pore opening, we can clearly see that larger pore openings would be achieved in larger rings as illustrated here by **gcc** and **bam** ZIFs (Table 2.1). These results match well with our analysis since larger rings can accommodate large imidazolates. Importantly, although large δ leads to large ring sizes (pore opening), it does not preclude the possibility of making smaller ring since it still has small 2-position functionality (typically H atom). However, large rings are not obtained when Im linkers of small δ are used, in such case, smaller rings are obtained. The essence of the first principle is that the maximum value of δ leads to the *maximum* possible ring size and this determines the size of the pore opening.

Principle II: Pore sizes. In order to assemble all rings together to make an extended porous zeolitic framework, small rings must appear together with large rings. In fact, the average size of all rings in a 3-dimensional 4-connected net is approximately 6.[12] More intuitively, small rings (small tiles) are needed to connect large rings (large tiles) by filling the empty space between them to form a continuous surface. Following this rule, it is apparent that incorporation of imidazolate with small δ could help to create ZIFs with large pores and apertures because imidazolate of large δ can produce large rings while imidazolate of small δ provides small rings.

The sole use of imidazolate with small δ can not produce ZIFs with large structures due to the incapability to create large rings. Similarly, the use of imidazolate with large δ creates large rings but it makesit difficult to create small rings. In fact, small 6 MRs are missing in all ZIFs constructed solely from bulky cbIm or larger linkers (**poz**, **moz**, **zea**, and **ykh**). To meet the average ring size requirement, these bulky imidazolates have to crowd their 2-H positions together to form ultra-small 3 MR, leading to a highly strained and distorted structure due to the increased curvature of the surface, thus decreasing the porosity of the structure. In addition, the bulky functionality sizes of the incorporated imidazolates further sacrifices useful pore spaces.

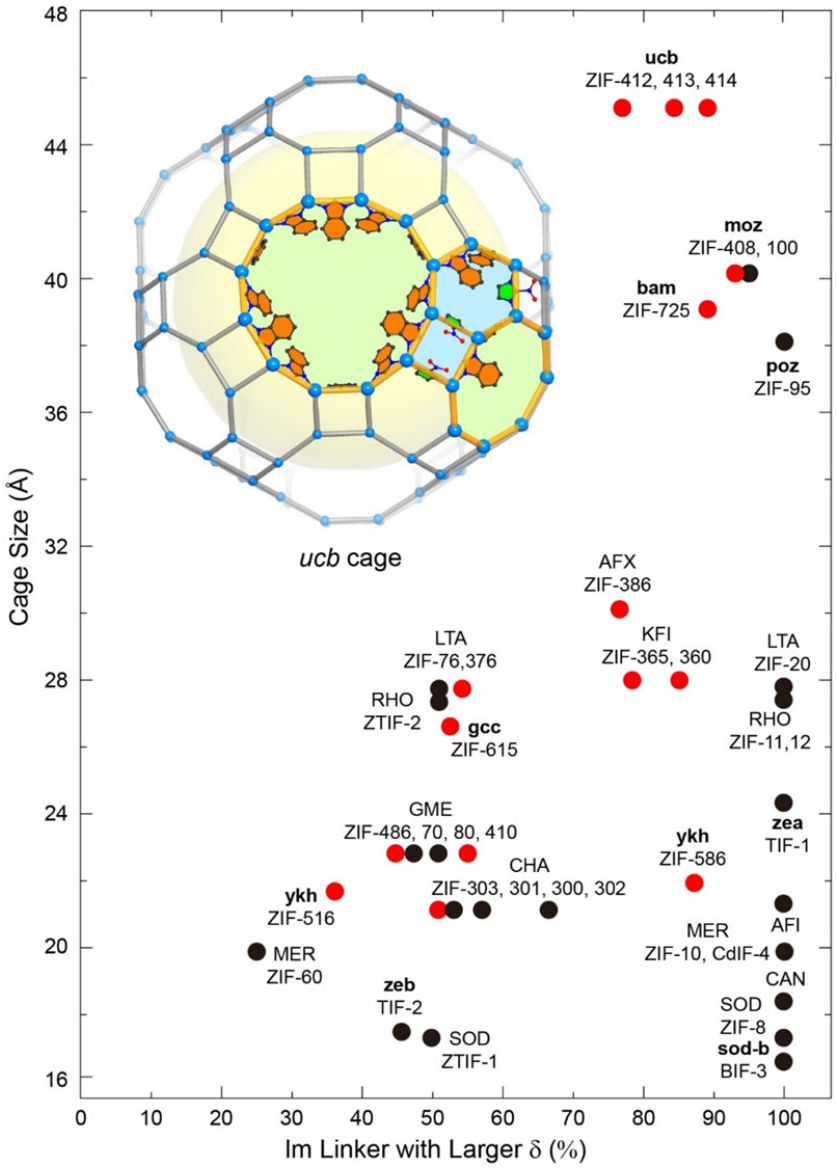

Figure 3.17 Distribution map of cage sizes as a function of the corresponding larger linker percentages in ZIFs. The size of the largest cage in each topology is plotted *vs.* the percentage of Im linkers with larger δ in each of the corresponding ZIFs. Larger Im is indicated for ZIFs containing a combination of Im linkers, where the smallest Im in the set is excluded. ZIFs made from only one Im linker are shown at 100%. Red dots represent structures reported in my thesis, and black dots represent already reported structures. Insert upper left, schematic of the largest *ucb* cage in **ucb** ZIF-412. It reveals how the large rings (8, and12 MRs) are joined through the smaller rings (4, and 6 MRs). The composition of these rings is also shown. Note that some imidazolates are aligned perpendicularly to the cage surface with their 2-positions pointing to the 4 MR perpendicular to the cage surface, which connect the cage into three-dimensional structures. Reprinted with permission from ref 9. Copyright 2017 American Chemical Society

Thus, use of bulky imidazolate and the addition of non-bulky Im are highly important

for making large cages and intuitively a balance must be struck when combining Im linkers of large and small δ. This is exemplified by comparison of ZIF-412 $[Zn(bIM)_{1.13}(nIM)_{0.62}(IM)_{0.25}]$ with **ucb** topology and the already reported ZIF-68 [Zn(bIM)(nIM)] with GME topology. They both contain ZIF linkers of larger δ value (679 and 347 $Å^4$ for bIM and nIM, respectively), which provide the 8 MR and 12 MR necessary to generate large cages. However, the addition of IM, which has a relatively smaller δ (248 $Å^4$), leads to the formation of more small rings (4 and 6 MR) in the structure of ZIF-412, and therefore this ZIF has a cage double the size of that found in ZIF-68 (Figure 3.17, Table 2.1).
It is clear from the discussion thus far that combining Im linkers with large and small δ, and balancing their proportion are critical to achieving ZIFs with large cages. Figure 3.17 shows a plot of the correlation of the percentage of linkers with relatively large δ *vs*. the resulting cage size in a ZIF. It reveals that progressively larger cages of diameter above 20Å can be achieved if at least 25% of the bulky Im linkers (all Im linkers other than those with the smallest δ in the composition of a ZIF) are present. Based on this relationship, the three new **ucb** ZIFs (ZIF-412, 413, and 414) stand out as having the largest cage size among all ZIFs.
Previously only eight topologies in ZIFs have shown large cage sizes: MER,[5] 20.5 Å; CHA,[13] 21.5 Å; AFI,[11] 21.7 Å, GME,[5] 22.6 Å; **zea**,[10] 25.1 Å; RHO,[5] 27.3 Å; LTA,[3] 27.5 Å; **poz**,[4] 38.1 × 33.8 Å; and **moz**,[4] 41.2 Å. Here, another six new topologies of large pore sizes: **ykh**, 22.3 Å; **gcc**, 27.2 Å; KFI, 27.8 Å; AFX, 28.4 × 22.6 Å; **bam**, 39.0 Å; and **ucb**, 45.8 Å are reported (cage size is estimated by the shortest Zn···Zn distance across the cage in order to compare the intrinsic difference of structure types, Figure 2, Table 1).

Combining multiple Im linkers with smaller and larger δ values is more fruitful in achieving large cages compared to single Im linker since we now can tune the small rings and larger rings respectively through the judicious selection of linker combinations; besides, less strained rings (4 MR, 6 MR) provide smooth surfaces and less strained structures; and small imidazolate increases the useful pore space due to their small sizes. This is demonstrated for all our new ZIF structures, most especially those with very large cages belonging to LTA, KFI, AFX, **gcc**, **bam**, and **ucb** topologies.

The use of too many of Im linkers with small δ will compromise the formation of the largest cages. This is made clear by the appearance of ZIFs with the largest cages (**ucb** ZIFs) on the right side instead of the left side of the plot in Figure 3.17, which is also pretty straightforward as the formation of the rings are now dominated by the small imidazolate. The second principle emphasizes that since large cages require both small and large rings, using combinations of Im linkers of small and large δ greatly facilitates the formation of such cages.

Principle III: Structure tunability. The first and second principles provide clear guidelines for achieving pore metrics without putting limits on the number and functionality of the Im linkers. A general question arises: How can we create diversity from a given set of available linkers? Based on this study, It is found that the ratio of Im linkers provides a handle for access ing ZIFs with a range of pore metrics. For example, the combination of IM (δ = 248 $Å^4$), mIM (δ = 319 $Å^4$), and nbIM (δ = 1064 $Å^4$), which when employed in different ratios gave us three new ZIFs that belong to three different topologies: ZIF-486 $[Zn(nbIM)_{0.20}(mIM)_{0.65}(IM)_{1.15}$, GME], ZIF-376 $[Zn(nbIM)_{0.25}(mIM)_{0.25}(IM)_{1.5}$, LTA] and ZIF-414 $[Zn(nbIM)_{0.91}(mIM)_{0.62}(IM)_{0.47}$, **ucb**] with cage sizes of 22.6, 27.5, and 45.8 Å, respectively (Figure 2 and Table 1). In essence, the third principle points to an immense diversity to be exploited for ZIF structures by varying the Im ratios, where not only the maximum pore opening and cage size are achieved but also any values up to the maximum. A point worthy of mention is that as the number of Im types increases in ZIF; the power of this

principle will be amplified in creating diverse structures and pore metrics.

3.3 Conclusions

In this Chapter, I analyzed the compositions and structures of known ZIFs and some of the ZIFs reported herein, to find underlying principles that could be used to guide the synthesis of ZIFs. A ring-directed synthesis approach was proposed proposed and found to be useful to guide the synthesis of other ZIFs reported here. The rings, which are building blocks in ZIF structures, act as a bridge to connect the starting material–imidazolate to the final structure. The imidazolate size influences the as-formed ring size in a ZIF structure, which in turn controls the pore and aperture sizes of a ZIF. The use of multiple imidazolate linkers allows the precise and gradual control of ring sizes, representing a powerful handle. I believe this approach could help to the future design of ZIF structures, as well as the fine tune of ZIF structures for specific functions.

3.4 Acknowledgements

I thank Prof. Omar Yaghi, Prof. Hexiang Deng, Dr Qi Liu for discussions, figures and summaries.

3.5 References

[1] Park, K. S.; Ni, Z.; Côté, A. P.; Choi, J. Y.; Huang, R. D.; Uribe-Romo, F. J.; Chae, H. K.; O'Keeffe, M.; Yaghi, O. M. *Proc. Natl. Acad. Sci. U.S.A.* **2006**, *103*, 10186.
[2] Phan, A.; Doonan, C. J.; Uribe-Romo, F. J.; Knobler, C. B.; O'Keeffe, M.; Yaghi, O. M. *Acc. Chem. Res.* **2010**, *43*, 58.
[3] Hayashi, H.; Côté, A. P.; Furukawa, H.; O'Keeffe, M.; Yaghi, O. M. *Nature Mater.* **2007**, *6*, 501.
[4] Wang, B.; Côté, A. P.; Furukawa, H.; O'Keeffe, M.; Yaghi, O. M. *Nature* **2008**, *453*, 207–211.
[4] Brown, A. J.; Brunelli, N. A.; Eum, K.; Rashidi, F.; Johnson, J. R.; Koros, W. J.; Jones, C. W.; Nair, S. *Science* **2014**, *345*, 71.
[5] Banerjee, R.; Phan, A.; Wang, B.; Knobler, C.; Furukawa, H.; O'Keeffe, M.; Yaghi, O. M. *Science* **2008**, *319*, 939.
[6] Ramirez, J. R.; Yang, H.; Kane, C. M.; Ley, A. N.; Holman, K. T. *J. Am. Chem. Soc.* **2016**, *138*, 12017.
[7] Shi, Q.; Xu, W.-J.; Huang, R.-K.; Zhang, W.-X.; Li, Yang; Wang, P.; Shi, F.-N.; Li, L.; Li, J.; Dong, J. *J. Am. Chem. Soc.* **2016**, *138*, 16232.
[8] Deng, H.; Doonan, C. J.; Furukawa, H.; Ferreira, R. B.; Towne, J.; Knobler, C. B.; Wang, B.; Yaghi, O. M. *Science* **2010**, *327*, 846.
[9] Yang, J.; Zhang, Y.; Liu, Q.; Trickett, C. A.; Gutierrez-Puebla, E.; Monge, M. Á.; Cong, H.; Aldossary, A.; Deng, H.; Yaghi, O. M. *J. Am. Chem. Soc.* 2017, *139*, 6448.
[10] Tian, Y. Q.; Zhao, Y.-M.; Chen, Z.-X.; Zhang, G.-N.; Weng, L.-H.; Zhao, D.-Y. *Chem. Eur. J.* **2007**, *13*, 4146.
[11] Shi, Q.; Xu, W.-J.; Huang, R.-K.; Zhang, W.-X.; Li, Y.; Wang, P.; Shi, F.-N.; Li, L.; Li, J.; Dong, J. *J. Am. Chem. Soc.* **2016**, *138*, 16232.
[12] Brunner, G. O. *Zeolites* **1990**, *10*, 612.
[13] Nguyen, N. T. T.; Furukawa, H.; Gándara, F.; Trickett, C. A.; Jeong, H. M.; Cordova, K. E.; Yaghi, O. M. *Angew. Chem. Int. Ed.* **2014**, *40*, 10645.

Chapter 4: A Mixed-linker Approach toward Porous Calcium Lactate Frameworks

4.1 Introduction

The successful implementation of mixed-linker approach in ZIFs encouraged us to explore the feasibility of this strategy in other fields. In this Chapter, the application of this approach to the field of environmentally friendly calcium-based MOFs was investigated.

Metal-organic frameworks (MOFs) have been widely applied to gas separation, storage, and catalysis.[1] However, the majority of MOFs are constructed from transition metal ions and organic linkers derived from petrochemical sources. The toxicity of these compounds has precluded the application of MOFs in many important areas requiring eco-friendly materials, such as, industrial food processing, biomedical devices, drug delivery, and agriculture.[2-3]

Preparation of MOFs from eco-friendly metal ions such as Ca^{2+}, with non-toxic, naturally occurring linkers would expand the scope of such applications. However, these materials remain largely synthetically inaccessible. Specifically, there have been no reported examples of MOFs bearing Ca^{2+} ions and environmentally friendly linkers. This challenge manifests as the result of the wide variety of coordination geometries and high coordination number of Ca^{2+} metal ions, and the lack of rigidity in naturally occurring organic linkers. Therefore, attempts to form MOFs from these constituient building blocks typically results in dense, non-porous structures.[4]

To overcome this problem, a mixture of lactate and acetate linkers was employed with Ca^{2+} in this work to synthesize the first two examples of porous calcium lactate frameworks.[5] Each of the two linkers was essential to the formation of the structure.

4.2 Materials and Methods

General synthesis and characterization methods. Calcium acetate monohydrate ($Ca(OAc)_2 \cdot H_2O$), L-(+)-Lactic acid, anhydrous methanol and ethanol were purchased from commercial source and were used directly without further purification. All synthetic procedures were conducted in air. The MOFs were activated by the following method: As-synthesized MOFs were washed with fresh anhydrous ethanol (MOF-1201) and methanol (MOF-1203) for 1 day, six times per day. The samples were then evacuated to remove guest molecules under vacuum (0.01 Torr) at ambient temperature for 12 hrs. The following measurements were conducted using the activated samples for MOFs unless otherwise noted. Elemental analysis (EA) of activated MOF-1201 and -1203 were performed using a Perkin Elmer 2400 Series II CHNS elemental analyzer; Attenuated-total-reflectance Fourier-transform infrared (ATR-FTIR) spectra of neat MOFs were recorded on a Bruker ALPHA Platinum ATR-FTIR Spectrometer.

MOF-1201, Ca_{14}(L-lactate)$_{20}$(Acetate)$_8$(EtOH)(H_2O). 0.071 g calcium acetate monohydrate ($Ca(OAc)_2 \cdot H_2O$, 0.4 mmol), and 0.072 g L-(+)-Lactic acid (HL, 0.8 mmol) were mixed in 6 mL anhydrous ethanol in a 23 mL Teflon autoclave. The autoclave was then sealed and heated in 120 °C isothermal oven for 4 days. After cooling down to room temperature, the crystals were washed with anhydrous ethanol for 1 day. (Yield: 26% based on Ca). EA: Calcd. for $Ca_{14}(C_3H_5O_3)_{20}(C_2H_3O_2)_8(C_2H_6O)(H_2O)$: C, 32.54; H, 4.62. Found: C, 31.67; H, 4.75. ATR-FTIR (4000-400 cm^{-1}): 3250(br), 2979(w), 1563(s), 1422(s), 1314(m), 1267(m), 1122(s), 1089(w), 1044(m), 930(w), 858(m), 773(m), 664(m), 616(m), 550(m), 469(w), 442(w), 423(w).

MOF-1203, Ca_6(L-lactate)$_3$(Acetate)$_9$(H_2O). 0.071 g calcium acetate monohydrate ($Ca(OAc)_2 \cdot H_2O$, 0.4 mmol), and 0.036 g L-(+)-Lactic acid (HL, 0.4 mmol) were mixed in 6 mL anhydrous methanol in a 23 mL Teflon autoclave. The autoclave was then sealed and heated in 100 °C isothermal oven for 3 days. After cooling down to room temperature, the crystals were washed with anhydrous methanol for 1 day. (Yield: 25% based on Ca). EA: Calcd. for $Ca_6(C_3H_5O_3)_3(C_2H_3O_2)_9$: C, 30.68; H, 4.20. Found: C, 31.33; H, 4.07. ATR-FTIR (4000-400 cm^{-1}): 3300(br), 2981(w), 1540(s), 1462(s), 1417(s), 1320(w), 1271(m), 1138(m), 1123(m), 1051(w), 1024(m), 956(w), 934(w), 860(m), 774(m), 662(s), 649(m), 617(s), 561(m), 468(m), 419(w).

^{1}H-NMR spectroscopy. ^{1}H NMR spectra on digested solutions of MOFs were acquired on a Bruker AVB-400 NMR spectrometer, with chemical shifts of linkers identified by comparing with spectra for each pure linker. Samples (*ca.* 10 mg for each) were dissolved in D_2O (600 µL) with sonication.

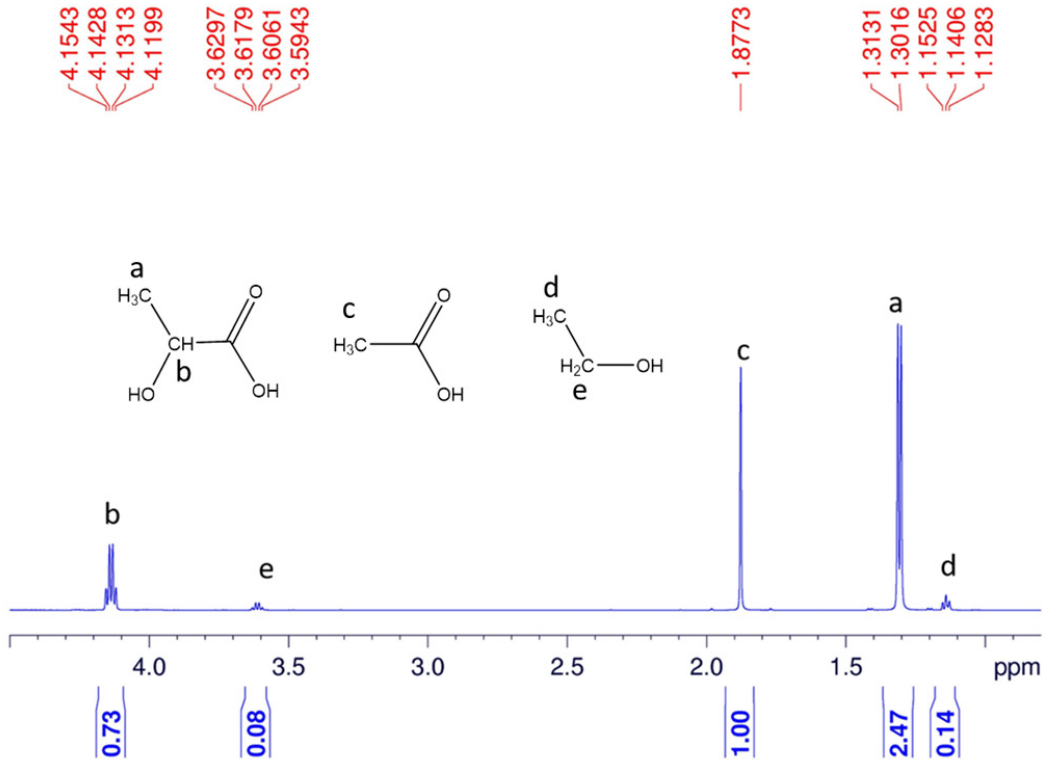

Figure 4.1 [1]H-NMR spectrum of digested MOF-1201.

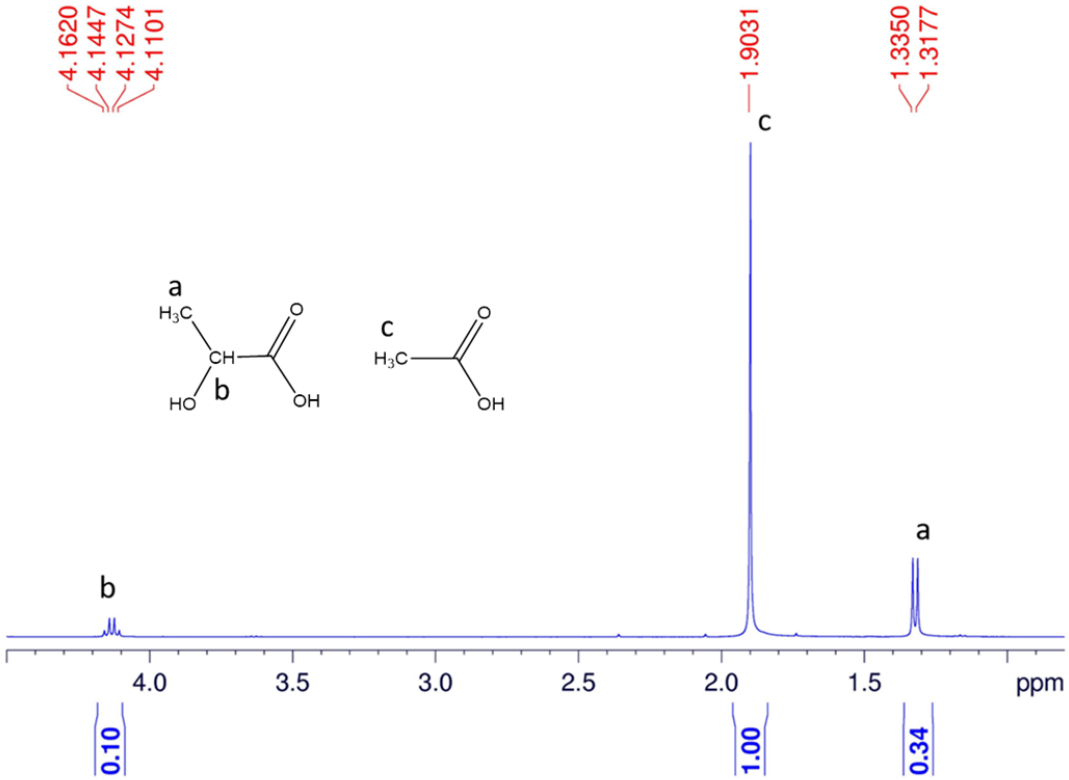

Figure 4.2 [1]H-NMR spectrum of digested MOF-1203.

Single crystal X-ray diffraction. Single crystal X-ray diffraction (SXRD) data was collected for both MOFs using as-synthesized crystals. Data for MOF-1201 and -1203 were collected at beamline 11.3.1 of the ALS at LBNL, equipped with a Bruker Photon 100 CMOS area detector using synchrotron radiation (10-17 KeV), at 0.7749(1) Å. Samples were mounted on MiTeGen® kapton loops and placed in a 100(2) K nitrogen cold stream.
Data were processed with the Bruker APEX2 software package,[6-7] integrated using SAINT v8.34A and corrected for the absorption by SADABS 2014/5 routines (no correction was made for extinction or decay). The structures were solved by intrinsic phasing (SHELXT) and refined by full-matrix least squares on F^2 (SHELXL-2014). All non-hydrogen atoms were refined anisotropically. Hydrogen atoms were geometrically calculated and refined as riding atoms unless otherwise noted. In both structures, highly disordered guest molecules occupying the cavities of the structure, which could not be modeled and so were accounted for using solvent masking using the Olex2 software package.[8-9]

Table 4.1 Crystal data and structure determination for MOF-1201

Compound	**MOF-1201**
Chemical formula	$C_{76}H_{127}O_{76}Ca_{14}$
Formula mass	2817.89
Crystal system	monoclinic
Space group	$P2_1$
λ (Å)	0.7749(1)
a (Å)	24.3868(11)
b (Å)	13.2612(6)
c (Å)	24.9710(10)
β (°)	90.327(2)
Z	2
V (Å^3)	8075.4(6)
Temperature (K)	100(2)
Size /mm^3	0.1 × 0.02 × 0.02
Density (g/cm^{-3})	1.159
Measured reflections	119229
Unique reflections	29436
Parameters	1544
Restraints	265
R_{int}	0.0723
θ range (°)	2.10-27.89
R_1, wR_2	0.0621, 0.1772
S (GOF)	1.076
Max/min res. dens. (e/Å^3)	0.60/-0.33
Flack parameter	0.150(10)

$^a R_1 = \Sigma||F_o| - |F_c||/\Sigma|F_o|$; $^b wR_2 = [\Sigma w(F_o^2 - F_c^2)^2/\Sigma w(F_o^2)^2]^{1/2}$; $^c S = [\Sigma w(F_o^2 - F_c^2)^2/(N_{ref} - N_{par})]^{1/2}$.

Table 4.2 Crystal data and structure determination for MOF-1203

Compound	**MOF-1203**
Chemical formula	$C_{40}H_{59.33}O_{40.67}Ca_9$
Formula mass	1551.64
Crystal system	orthorhombic
Space group	$I2_12_12_1$
λ (Å)	0.7749(1)
a (Å)	10.5046(4)
b (Å)	22.2580(9)
c (Å)	31.2485(13)
Z	4
V (Å^3)	7306.3(5)
Temperature (K)	100(2)
Size /mm^3	0.09 × 0.005 × 0.005
Density (g/cm^{-3})	1.411
Measured reflections	7620
Unique reflections	3865
Parameters	433
Restraints	59
R_{int}	0.1195
θ range (°)	2.23-22.86
R_1, wR_2	0.0524, 0.1406
S (GOF)	1.026
Max/min res. dens. (e/Å^3)	0.60/-0.33
Flack parameter	0.09(3)

$^aR_1 = \Sigma||F_o| - |F_c||/\Sigma|F_o|$; $^bwR_2 = [\Sigma w(F_o^2 - F_c^2)^2/\Sigma w(F_o^2)^2]^{1/2}$; $^cS = [\Sigma w(F_o^2 - F_c^2)^2/(N_{ref} - N_{par})]^{1/2}$.

Powder X-ray diffraction. Powder X-ray diffraction (PXRD) analysis were conducted on a Bruker D8 Advance diffractometer with Cu Kα radiation (λ = 1.54056 Å).

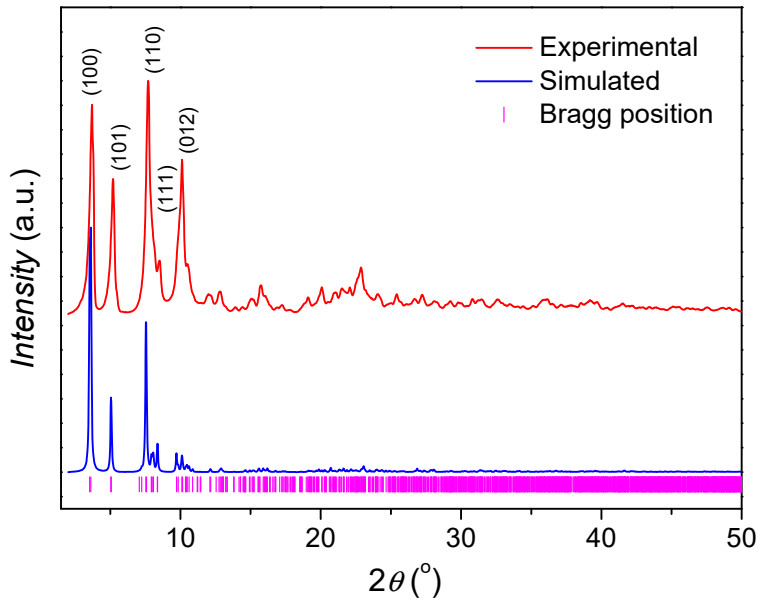

Figure 4.3 Comparison of the experimental PXRD patterns of MOF-1201: activated (red) and simulated pattern (blue) from single crystal X-ray data.

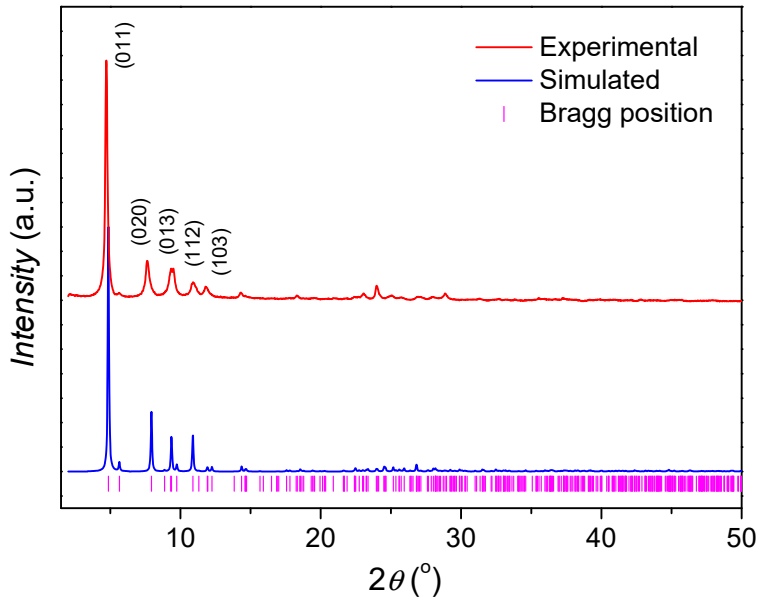

Figure 4.4 Comparison of the experimental PXRD patterns of MOF-1203: activated (red) and simulated pattern (blue) from single crystal X-ray data.

Low-pressure gas adsorption measurements.

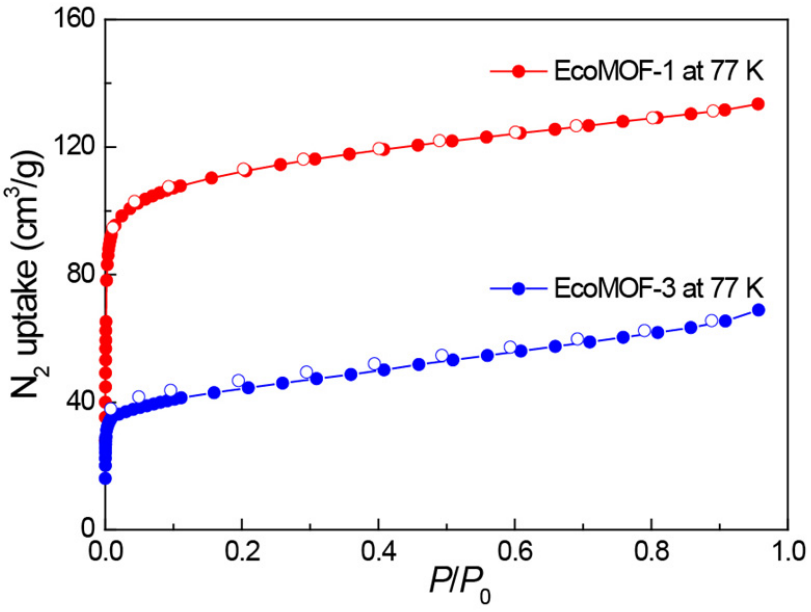

Figure 4.5 Nitrogen adsorption isotherms of MOF-1201 and MOF-1203 at 77 K.

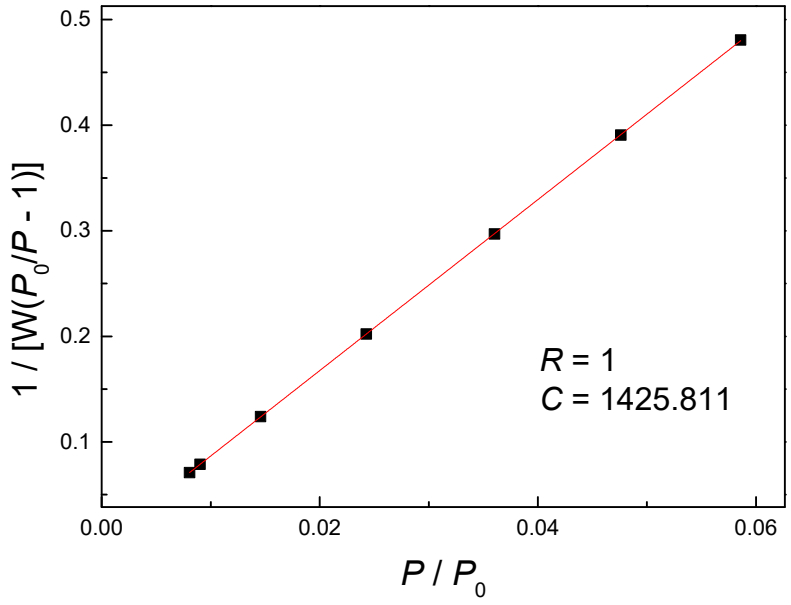

Figure 4.6 Multiple point BET plot[10] of MOF-1201 giving a surface area of 430 m^2/g.

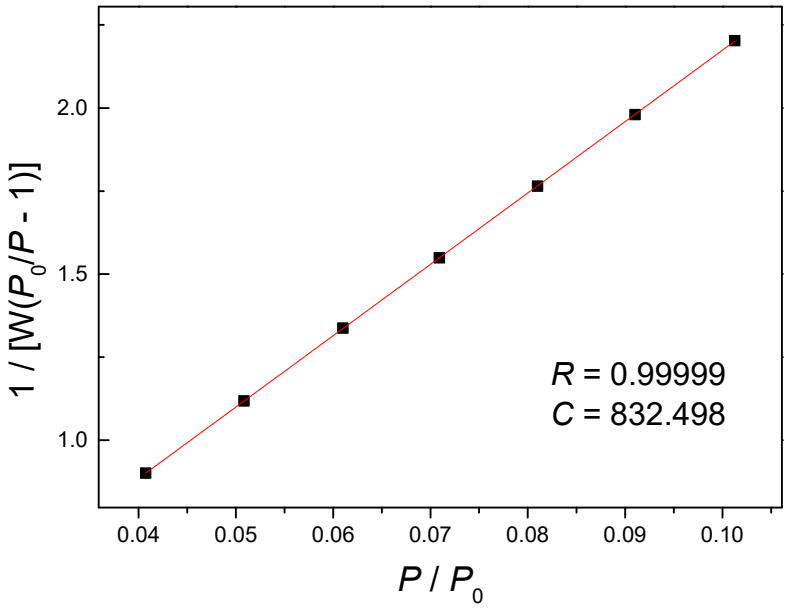

Figure 4.7 Multiple point BET plot of MOF-1203 giving a surface area of 160 m^2/g.

4.3 Results and Discussion

Hydrothermal reaction of a suspension of calcium acetate and L-lactic acid in ethanol (methanol) at 120 °C (100 °C) for a period of 4 (3) days gave colorless rod-shaped crystals of MOF-1201 (needle-shaped crystals of MOF-1203), respectively. The crystals were then harvested for single-crystal X-ray diffraction analysis. The exact molar ratios of the lactate and acetate linkers in the MOFs were further determined by ^{1}H-NMR spectroscopy and elemental microanalysis of the solvent-free samples

Single-crystal X-ray diffraction analysis revealed that both MOF-1201 and 1203 are extended frameworks constructed from Ca^{2+} as nodes and both lactate and acetate as linkers. MOF-1201 crystallizes in the monoclinic $P2_1$ space group with the lattice constants of a = 24.39 Å, b = 13.26 Å, c = 24.97 Å, β = 90.33°. In this structure, fourteen crystallographically unique calcium atoms exist [Ca(1) to Ca(14)] (Figure 4.8), all of which are capped by the O atoms from lactate (carboxylic O or hydroxyl O), acetate (carboxylic O) or water to form calcium oxide polyhedra. Coordination modes of the linkers to Ca^{2+} vary—four different modes are found in lactate [(i), (ii), (iii), and (vi)] and three in acetate [(vii), (ix), and (xi)] (Figure 4.8), among which the lactate with mode (vi) and the acetate with mode (vii) act as terminal ligands and cap only one Ca^{2+} center [Ca(5), and Ca(11), respectively], while the remaining others act as bridges to connect two or three Ca^{2+}. These bridging lactates and acetates link together all Ca^{2+} centers to form MOF-1201, *e.g.* Ca(1), Ca(2), and Ca(3) are bridged by a lactate with coordination mode (i): Ca(1) coordinates to the hydroxyl O and the adjacent carboxylic O, Ca(2) coordinates to only the carboxylic O, and Ca(3) coordinates to the other carboxylic O. Similarly, Ca(1), Ca(2), and Ca(4) are bridged by the same mode; Ca(4), Ca(5), and Ca(7) are bridged by mode (iii); Ca(7), Ca(8), and Ca(9) by mode (i); Ca(7),

Ca(8), and Ca(10) by mode (i); Ca(10), Ca(11), and Ca(12) by mode (xi); Ca(6), Ca(5), and Ca(7) by mode (ii); Ca(12), Ca(13), and Ca(14) by mode (i) to connect all of the Ca^{2+} centers.

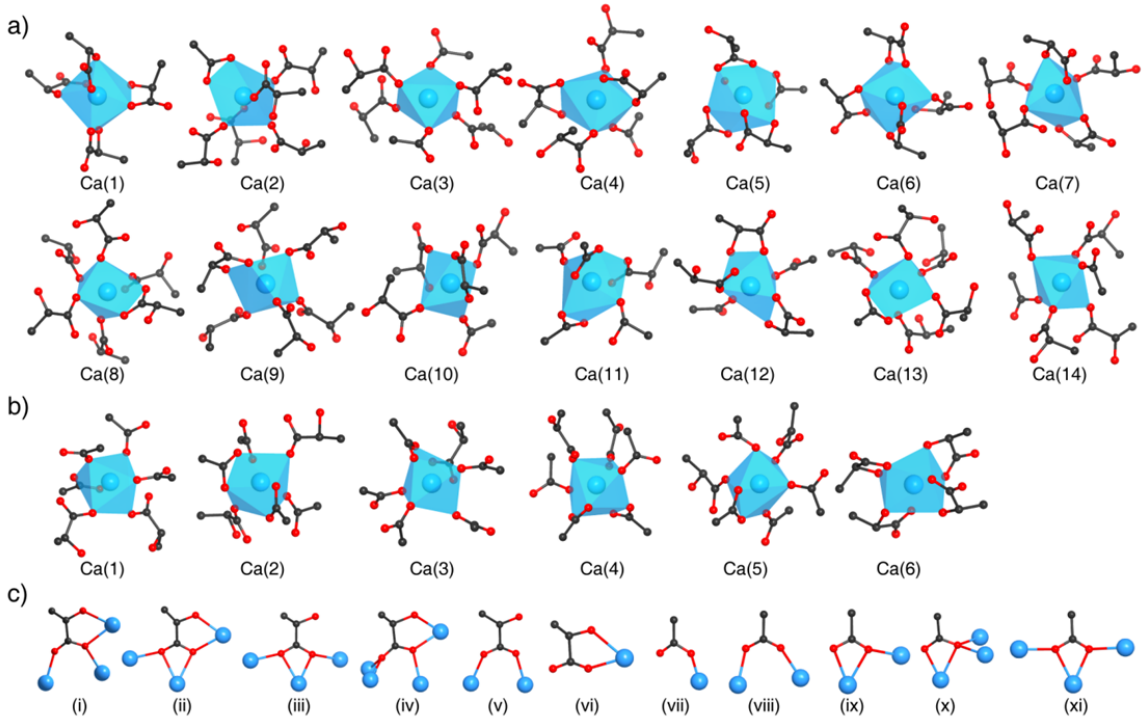

Figure 4.8 The Ca^{2+} centers in MOF-1201 (a) and in MOF-1203 (b) and their coordination with lactate and acetate. Coordination numbers for Ca(1) to Ca(14) in MOF-1201 are 8, 7, 6, 7, 9, 8, 7, 7, 7, 7, 8, 7, 7, and 6, respectively. Coordination numbers for Ca(1) to Ca(6) in MOF-1203 are 7, 8, 7, 8, 7, and 9, respectively. (c) Coordination modes of the lactate [(i)-(vi)] and acetate [(vii)-(xi)]. C in black, O in red, Ca in blue, Ca^{2+} oxide polyhedra in blue. H omitted for clarity. Reprinted with permission from ref 5. Copyright 2017 American Chemical Society

MOF-1201 has 1D infinite channels along the *b*-axis (Figure 4.9). The channels are encompassed by a right-handed single strand helical chain, with sixteen Ca^{2+} atoms per turn [in the sequence of Ca(5), Ca(4), Ca(2), Ca(1), Ca(11), Ca(12), Ca(13), Ca(6), Ca(5), Ca(4), Ca(2), Ca(1), Ca(11), Ca(12), Ca(13), Ca(6)]. The aperture is around 7.8 Å and the pitch is around 13.3 Å. Two adjacent turns are further crosslinked by additional calcium oxide polyhedra. Specifically, two Ca(2) and two Ca(13) centers in each turn are bridged by three calcium oxide polyhedra (in the sequence of Ca(3)-Ca(2)-Ca(3), and Ca(14)-Ca(13)-Ca(14). The two Ca(5) and two Ca(11) in each turn are bridged by seven calcium oxide polyhedra [in the sequence of Ca(7)-Ca(8)-Ca(9)-Ca(8)-Ca(9)-Ca(8)-Ca(7), and Ca(10)-Ca(8)-Ca(9)-Ca(8)-Ca(9)-Ca(8)-Ca(10). The curved bridges result in a slightly larger internal pore size (*ca.* 9.6 Å) compared to the aperture (*ca.* 7.8 Å).

MOF-1203 crystallized in the orthorhombic $I2_12_12_1$ space group and has the lattice constants of a = 10.50 Å, b = 22.26 Å, c = 31.25 Å. Six distinct Ca^{2+} centers exist in the structure, and are linked by lactate and acetate to form linked calcium oxide polyhedra

(Figure 4.8). Three coordination modes are found in lactate [(i), (iv), and (v)] and in acetate [(viii), (x), and (xi)] (Figure 1c), all linkers act as bridges connecting two to four Ca^{2+} centers. For example, Ca(1), Ca(2), and Ca(3) are bridged by an acetate with coordination mode (xi). Ca(1) coordinates to only one of the carboxylic O, Ca(3) coordinates to the other, and Ca(2) coordinates both of the carboxylic O. Similarly, Ca(3), Ca(4), and Ca(5) are bridged by the same mode; Ca(6), Ca(1), and Ca(5) by mode (i). The resultant framework reveals another type of 1D open channel (Figure 4.9), which is surrounded by four calcium oxide polyhedra based rings [10 membered-ring (10 MR)—Ca(6), Ca(1), Ca(5), Ca(3), Ca(1), Ca(6), Ca(1), Ca(3), Ca(5), Ca(1)] crosslinked by two Ca(4) and two Ca(2) (Figure 2c). The channel has an aperture constructed from 22 calcium oxide polyhedra, however, the internal diameter of the channel are smaller than MOF-1201 as the result of its rectangular shape, and the two incurvate Ca(4) and their linkers further divided channel into two smaller parts with an aperture of *ca.* 4.6 Å and pore of *ca.* 5.6 Å.

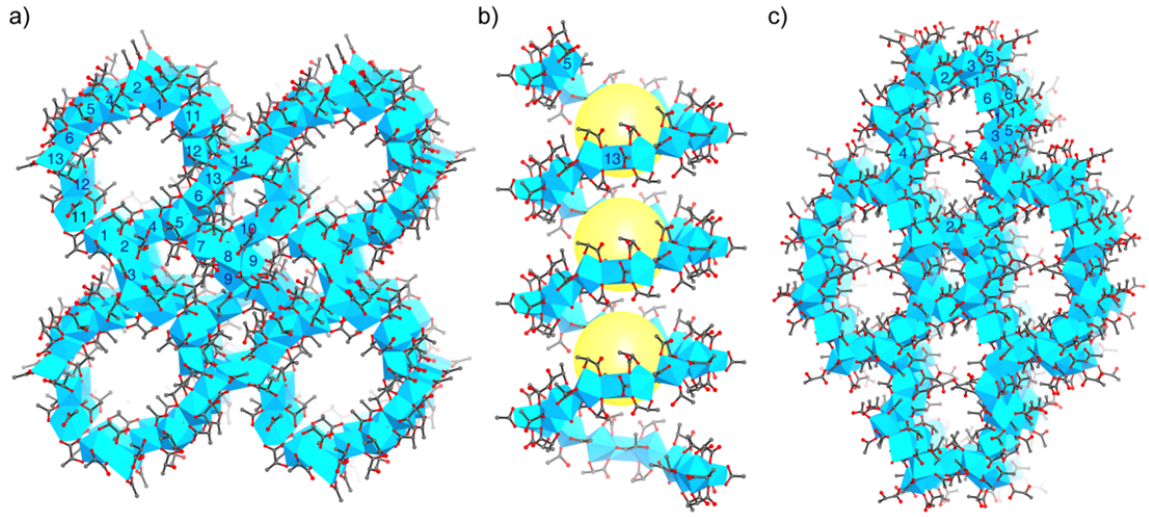

Figure 4.9 X-ray single crystal structure of MOF-1201 (a,b) and MOF-1203 (c). (a) The structure of MOF-1201, viewed along *b* axis; (b) The single helical channel of MOF-1201, viewed along *a* axis; (c) The structure of MOF-1203, viewed along *a* axis; Channels and pores are illustrated in yellow balls in (b); C in black, O in red, Ca in blue, Ca^{2+} oxide polyhedra in blue. H omitted for clarity. Reprinted with permission from ref 5. Copyright 2017 American Chemical Society

Samples of MOF-1201 and MOF-1203 were solvent exchanged with ethanol (MOF-1201) and methanol (MOF-1203) for three days, followed by direct evacuation under dynamic vacuum (0.04 mbar) at room temperature for 12 hours to give solvent-free samples for evaluation of their permanent porosity. Nitrogen sorption measurements at 77 K were then carried out. Both of the frameworks exhibited fully reversible Type I isotherms with steep N_2 uptake in the low-pressure regions ($P/P_0 < 0.05$) (Figure 4.5), indicating the permanent microporosity of these materials.[11] The Brunauer-Emmett-Teller (BET) surface areas[9] of MOF-1201 and MOF-1203 are estimated to be 430 and 160 $m^2\ g^{-1}$ from N_2 isotherms. They have pore volumes of 0.18 $cm^3\ g^{-1}$ and 0.06 $cm^3\ g^{-1}$, respectively, which are consistent with those calculated from single crystal structures using PLATON.[10] Crystallinity of the solvent-free samples were then checked with powder X-ray diffraction (PXRD). The obtained powder patterns are in good agreement with the diffraction patterns simulated from

the single crystal structures, confirming the maintenance of their structural integrity upon activation and the phase purity of the bulk materials (Figure 4.9).

Lactate has access to multiple coordination modes, allowing it to bridge multiple metal centers to form an extended structure. In contrast, acetate binds fewer metal centers, reducing the connectivity of the metals and the amount of space they occupy. (Figure 4.8) Without the lactate linkers, a three-dimensional framework does not form, while without the acetate linkers, only dense calcium lactate was obtained. These results delineate the importance of a mixed-linker approach in which each linker plays a distinct role and cooperatively produce porous structures.

4.4 Conclusions

Employing a mixed-linker approach is proved to be instrumental in the successful synthesis of porous, environmentally friendly calcium lactate frameworks. The lactate and acetate linkers with different sizes and coordination modes cooperated synergistically to balance the space occupation and connectivity of the porous framework. I expect that this principle can be applied to guide the synthesis of other MOFs from naturally occurring flexible linkers to expand this family of environmentally-friendly MOFs.

4.5 Acknowledgments

Support for synthesis and characterization by BASF SE (Ludwigshafen, Germany). Support from Advanced Light Source by the Director, Office of Science, Basic Energy Sciences, of the U.S. Department of Energy under Contract No. DE-AC02-05CH11231 (Beamline 11.3.1). This research benefits from an ongoing collaboration with King Abdulaziz Center for Science and Technology (KACST).

4.6 References

[1] Schröder, M. *Functional Metal-Organic Frameworks: Gas Storage, Separation and Catalysis;* Springer: Berlin, 2010.
[2] Forgan, R.S. Metal-Organic Frameworks: Edible Frameworks. *Encyclopedia of Inorganic and Bioinorganic Chemistry*; John Wiley & Sons: New York, 2014.
[3] Imaz, I.; Rubio-Martínez, M.; An, J.; Solé-Font, I.; Rosi, N. L.; Maspoch, D. *Chem. Comm.* **2011**, *47*, 7287.
[4] Fromm, K. M. *Coord. Chem. Rev.* **2008**, *252*, 856.
[5] Yang, J.; Trickett, C. A.; Alahmadi, S. B.; Alshammari, A. S.; Yaghi, O. M. *J. Am. Chem. Soc.* **2017**, *139*, 8118.
[6] Bruker. *APEX2*. (Bruker AXS Inc., Madison, Wisconsin, U.S.A. 2010).
[7] Sheldrick, G. M. *Acta Cryst. A* **2008**, *64*, 112–122.
[8] Dolomanov, O. V.; Bourhis, L. J.; Gildea, R. J.; Howard, J. A. K.; Puschmann, H. J. *Appl. Cryst.* **2009**, *42*, 339.
[9] Rees, B.; Jenner, L. B.; Yusupov, M. *Acta Cryst. D* **2005**, *61*, 1299.
[10] Walton, K. S.; Snurr, R. Q. *J. Am. Chem. Soc.* **2007**, *129*, 8552.
[11] Thommes, M.; Kaneko, K.; Neimark, A. V.; Olivier, J.; Rodriguez-Reinoso, F.; Rouquerol, J.; Sing, K. S. *Pure and Appl. Chem.* **2015**, *87*, 1051.

Chapter 5: The Use of Metal-Organic Frameworks for Emerging Environmetal Applications

5.1 Introduction

There is ever-increasing concern over global environmental issues including air pollution, water pollution. These phenomena pose significant health risks to the global population. Indeed, the World Health Organization (WHO) suggests that poor air quality is linked to one eighth of total global deaths.[1]

Selective adsorption of pollutants from air and water by porous materials can greatly augment environmental remediation efforts. Traditional adsorbents (porous carbon and zeolites) have been widely applied, and in the last decade, the emergence of MOF materials brought new opportunities to this field.[2] This is largely due to their exceptional structural and chemical designability, allowing for precise tailoring to adsorb specific pollutant molecules.

In this Chapter, the efforts on the uses of the newly made zeolitic imidazolate frameworks and calcium lactate frameworks for environmental applications are presented. I will show that the hydrophobicity, stability, and porosity of ZIFs can be advantageous with respect to the removal of large volatile organic compounds from mixed gas streams for air purification. I will also demonstrate that the environmentally-friendly components and porosity of calcium lactate frameworks can be used to address the excessive, inefficient, and pollutive nature of pesticides in agriculture. The MOF can be used as an effective pesticide carrier for agricultural purposes, representing the first example of using MOFs for agriculture applications.

5.2 Materials and Methods

Removal of volatile organic compounds (VOCs) from humid air. Water, octane, and *p*-xylene isotherms were measured at 25 ^{o}C using an in-house BEL Japan BELSORP-aqua3. Prior to measurement, analytes were flash frozen in liquid nitrogen and then evacuated under dynamic vacuum at least twice to remove any gases in the reservoir. The measurement temperature was controlled and monitored with a water bath held at 25 ^{o}C. Helium was used to estimate dead space for vapor adsorption measurements.

Breakthrough experiments were carried out according to published procedures with some modifications.[3-4] Figure 5.2 depicts the breakthrough apparatus. The system contains a fixed adsorbent bed and bypass line. Adsorbent materials were packed into stainless steel Swagelok tubing (2 mm i.d. × 20 mm) with a height of 8 mm. The experiments under dry conditions were performed by first flowing dry air at 7 sccm through glassblower cell with octane or *p*-xylene (Glassblowers.com Inc.). The glassblower cell sits in a water bath of 15 ^{o}C generating octane vapor (25 ^{o}C for generating a vapor pressure of *p*-xylene). Then the gas stream was mixed with another stream of dry air at 13 sccm to achieve a final flow rate of 20 sccm before passing through the adsorbent bed. The flow rate was determined by MKS Alta digital mass flow controllers; the pressure was held at 770 Torr by an MKS type 640 pressure controller. The gaseous effluent from the sample bed was monitored for nitrogen, oxygen, water, and octane/*p*-xylene with a mass spectrometer (Hiden Analytical HPR20). Breakthrough concentration is defined as 5% analyte as a function of the feed concentration. The time at which the concentration of contaminant gas in the effluent surpasses the breakthrough concentration is designated as the breakthrough time. Feed concentration was determined using SHIMADZU GCMS QP2010SE with benzene vapor as internal standard

(910 ppm for octane and 850 ppm for *p*-xylene). The breakthrough time was corrected by subtracting the time needed for octane or *p*-xylene to breakthrough a bed filled with sand. In wet cycles, the 13 sccm air flow was saturated with moisture by passing through a humidifying glassblower cell (Glassblowers Inc.). The cell was placed in a water bath held at 30 °C, generating 100% relative humidity. Before introducing the resulting wet octane/*p*-xylene gas feed stream, the adsorbent material was equilibrated with 100% moisture-saturated air for 30 mins. Regeneration of the adsorbent was done by purging the sample in a dry air flow (30 mins at R.T. and 60 mins at 95 °C). Ultra-high-purity grade N_2, air, and He gases (Praxair, 99.999% purity) were used throughout the experiments. Crystal density of Mg-MOF-74 (0.91 g cm^{-3}) and Cr-MIL-101 (0.44 g cm^{-3}) were adopted from reference 4 and 5, respectively.

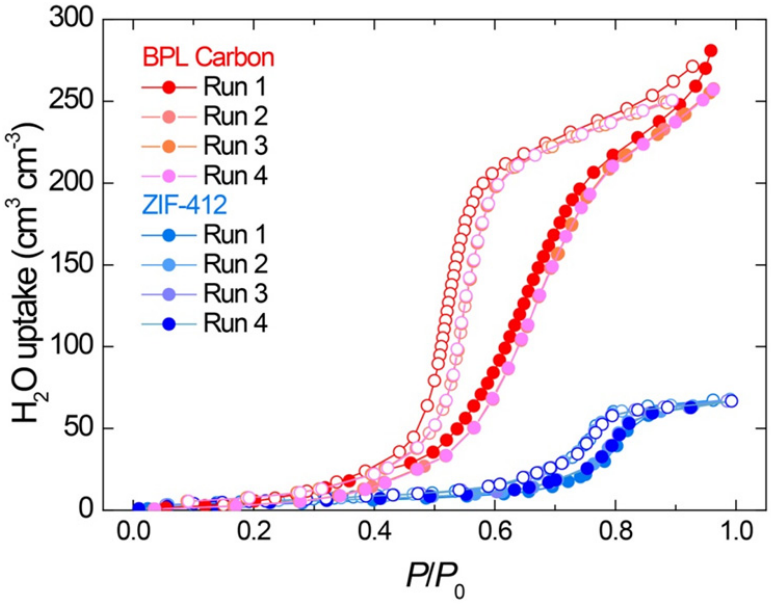

Figure 5.1 Water adsorption isotherm of **ZIF-412** and BPL carbon (ρ=0.43 g/cm^3) at 298 K. Sample was regenerated at 150 °C for 4 hours between each run.

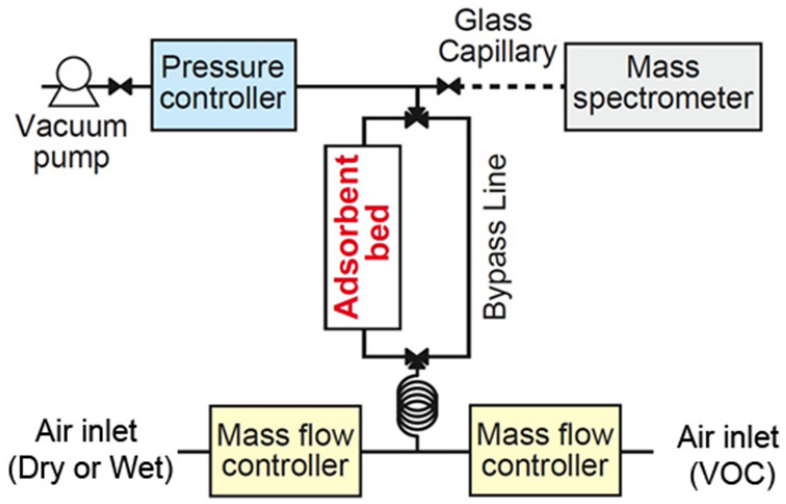

Figure 5.2 Schematic representation of the breakthrough experimental setup.

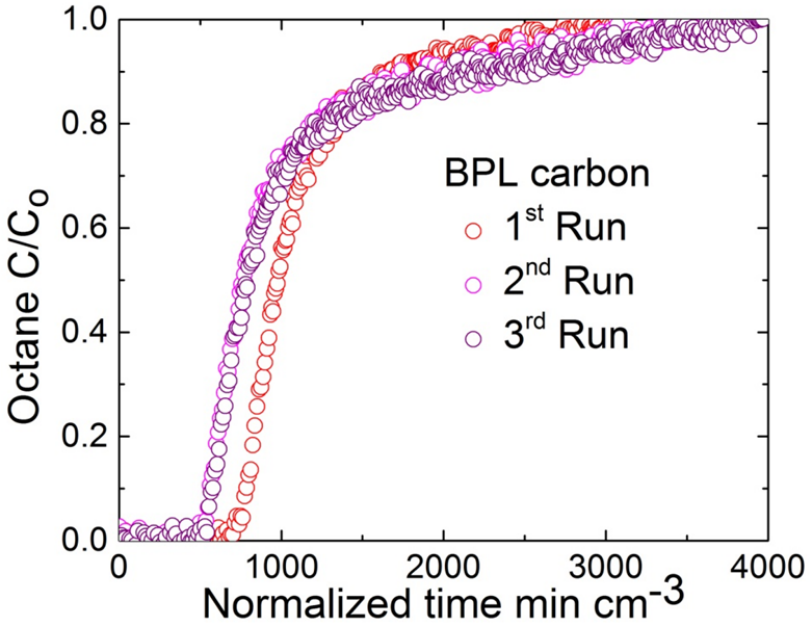

Figure 5.3 Breakthrough curves of BPL carbon for octane under wet conditions for three cycles. 28% shorten of the breakthrough time was observed after 1st cycle. Lost of performance for BPL carbon upon the 2nd and 3rd run is attributed to the very common regeneration issues with BPL carbon, which can't be fully regenerated easily.

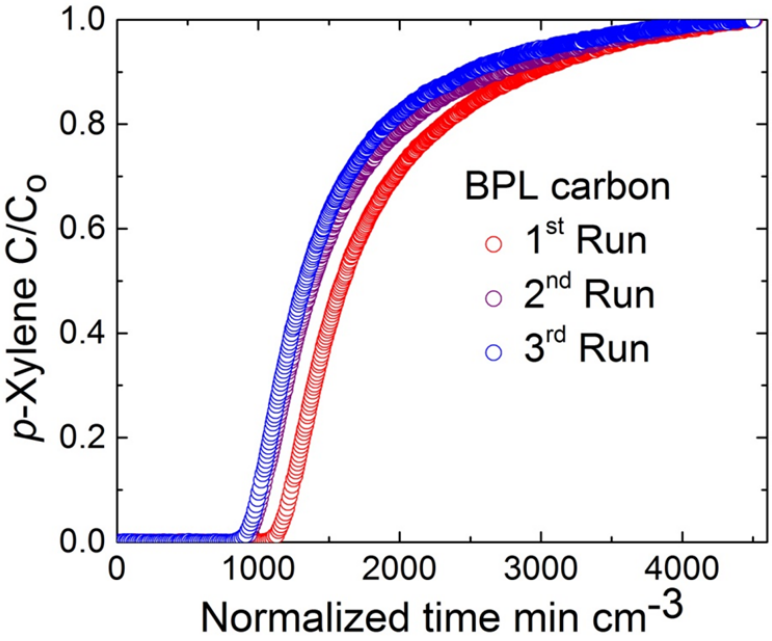

Figure 5.4 Breakthrough curves of BPL carbon for *p*-xylene under wet conditions for three cycles. 17% shorten of the breakthrough time was observed after 1st cycle. Lost of performance for BPL carbon upon the 2nd and 3rd run is attributed to the very common regeneration issues with BPL carbon, which can't be fully regenerated easily.

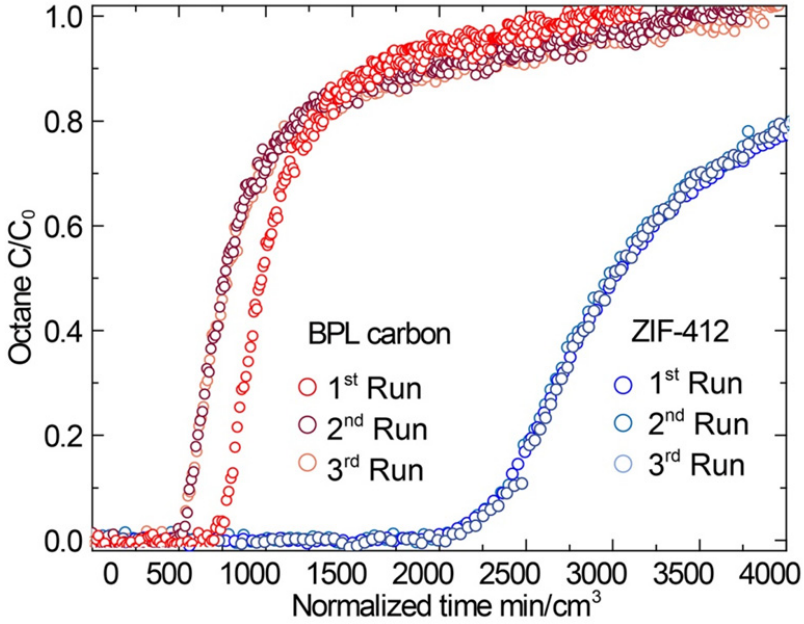

Figure 5.5 Comparison of breakthrough curves under wet conditions (R.H. 65%, 298 K) for **ZIF-412** (blue to light blue) and BPL carbon (red to light red) at 298 K for octane up to three cycles.

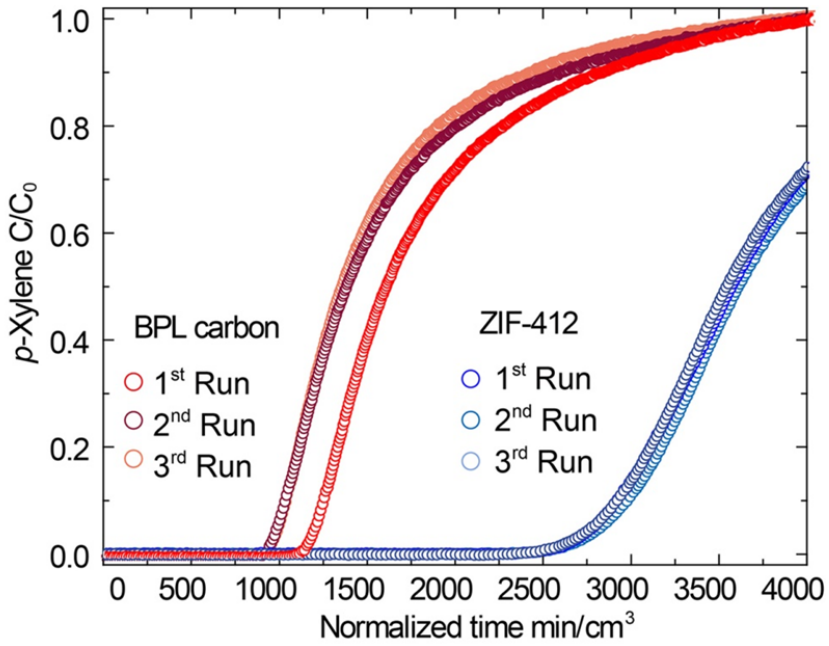

Figure 5.6 Comparison of breakthrough curves under wet conditions (R.H. 298 K) for **ZIF-412** (blue to light blue) and BPL carbon (red to light red) at 298 K for *p*-xylene up to three cycles.

Environmetally friendly calcium lactate frameworks as degradable pesticide carrier. *cis*-1,3-dichloropropene vapor sorption isotherm at 25 °C were measured in-house on a BEL Japan BELSORP-aqua3. Prior to measurements, the sample was evacuated under dynamic vacuum. The measurement temperature was controlled and monitored with a water bath held at 25 °C. Helium was used to estimate dead space for vapor adsorption measurements.

Slow release experiments were carried out using the TA Q500 thermal analysis system under constant air flow of 1 cm^3 min^{-1}. Only demonstratation experiments in lab is carried out to show the capability of slow release by MOF-1201.

5.3 Results and Discussion

Removal of VOCs from humid air by large-pore ZIF-412. The remarkably large cage of ZIF-412, its permanent porosity, and hydrophobic interior led to our experiments to test its performance in the removal of volatile organic compounds (VOCs), especially those of large molecular size. These commonly used molecules continue to be a major environmental and health concern because they are difficult to remove from sources where they are present in very low concentrations (ppm levels).[6-10] There are several requirements for a material to be employed for this purpose: (1) high capacity, (2) ability of uptake at low concentrations, (3) water stability and performance under wet conditions, and (4) cycling performance without losing capacity. Activated carbons have been extensively used; however, they suffer from the relatively low capacity and difficulty in regeneration.[7] MOFs previously tested for this use show better uptake capacity in dry conditions but not in the presence of water — a critical challenge and a prerequisite for this application.[11-13]

Here, large pore ZIF-412 is applied to address the challenges.[14] Its water adsorption

isotherms show strong hydrophobicity (Figure. 5.1). Static adsorption isotherms of octane and *p*-xylene, representatives of the aliphatic and aromatic VOCs, show that ZIF-412 can take up 3.0 mmol/cm^3 octane and 3.4 mmol/cm^3 *p*-xylene vapors at low partial pressure (P/P_0 = 0.1, 298 K), 2.6 and 2.5 times higher compared to BPL carbon, respectively (Figure 5.7a, b), these values are comparable to the best performing porous materials reported so far (3.2 mmol/cm^3 of octane in Mg-MOF-74 at P/P_0 = 0.08, 293 K; 3.7 mmol/cm^3 of *p*-xylene in Cr-MIL-101 at P/P_0 = 0.1, 298 K, both are under dry condition).[12-13]

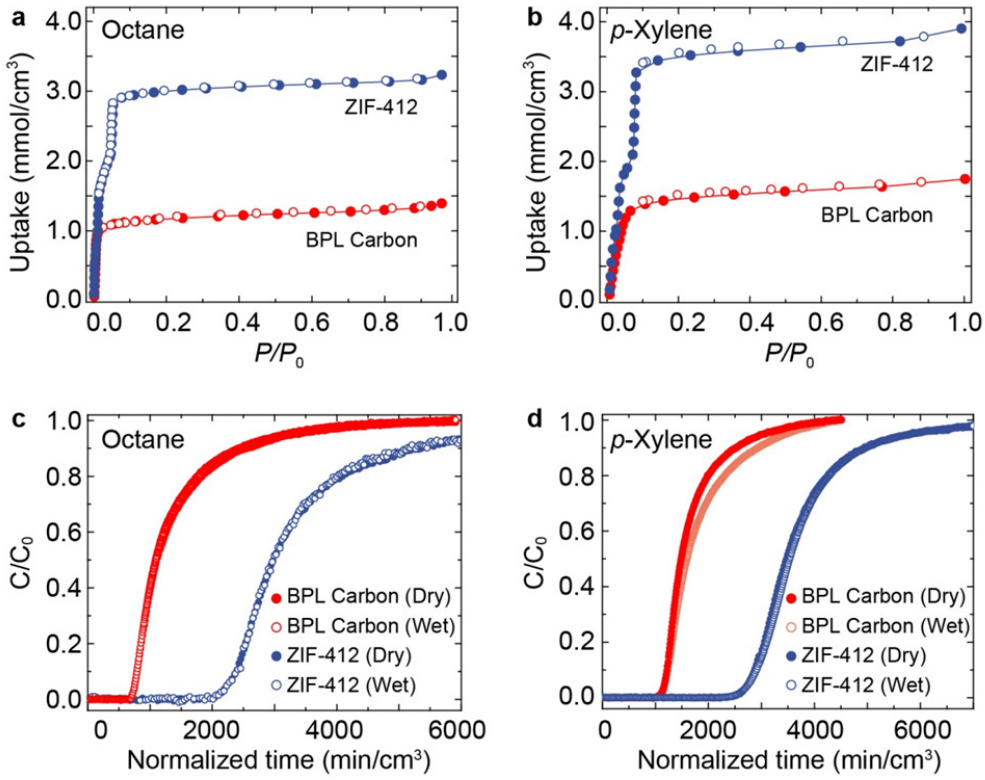

Figure 5.7 Octane and *p*-xylene removal using ZIF-412 and BPL carbon. **a**, Static vapor adsorption isotherm at 298 K for octane (left), where ZIF-412 shows 260% more uptake than BPL carbon. **b**, Static vapor adsorption isotherm for *p*-xylene (right), where ZIF-412 shows a 250% improvement in uptake. **c**, Breakthrough curves under both dry and wet conditions (R.H. 0% and 65%, respectively) using ZIF-412 and BPL carbon at 298 K for octane, and **d**, Breakthrough curves for *p*-xylene. Solid circles represent breakthrough curves under dry conditions; empty circles represent breakthrough curves under wet conditions. ZIF-412 shows much longer breakthrough time in comparison to BPL with and without the interference of water. Reprinted with permission from ref 14. Copyright 2017 American Chemical Society

Dynamic breakthrough experiments confirmed the VOC separation capability of ZIF-412: At a low concentration of octane (910 ppm) in dry air stream, ZIF-412 showed a breakthrough time up to 2280 min/cm^3 (the time when outlet concentration reach 5% of the feed concentration) — 3.0 times longer than BPL carbon under the same conditions (Figure

5.7). This performance was unaltered for ZIF-412 under wet conditions (Relative Humidity, R.H. 65%, 298 K) and over three continuous cycles (Figure 5.5). In contrast, when BPL carbon was used, although the capacity remains the same in the presence of water, after the regeneration, in the subsequent 2nd and 3rd run, BPL carbon lost 28% of its original capacity indicated by the shortened breakthrough time after the first run (Figure 5.4-5.5). With respect to the best performing porous material tested so far, Mg-MOF-74, which has a high uptake of 3.2 mmol/cm^3 under dry condition (293 K), its uptake diminished to 0.2 mmol/cm^3 in the presence of water (R.H. 80%, 293 K).[12] Similar to the results found for octane, the breakthrough tests for *p*-xylene (850 ppm) using ZIF-412 also show exceptional cycling performance in the presence of water. Specifically, the *p*-xylene breakthrough time for ZIF-412 is 2780 min/cm^3, with no loss of performance in the presence of water over three cycles (Figure 5.7). The exceptional performance and stability of ZIF-412 material is attributed to its permanent porosity and hydrophobicity.

Environmetally friendly calcium lactate frameworks as degradable pesticide carrier. The porosity of MOF-1201 along with its environmentally friendly compositions: Ca^{2+}, lactate, and acetate, allowed us to explore the potential application of these MOFs in agriculture industry, where the non-toxicity and human and environmental benignity are the most important requirements for a material to be used Here the use of MOF-1201 as a solid formulation for volatile liquid fumigants is demonstrated.

Fumigants are an important family of pesticides that are widely used to prevent plants, especially those of high-value (*e.g.* strawberries and tomatoes), from soil-borne diseases to improve the quality and yield.[15-16] Two volatile liquid compounds, 1,3-dichloropropene (*cis*- and *trans*- mixtures) and chloropicrin, have been the most widely used fumigants with large quantities (5.99×10^6 kg and 4.08×10^6 kg, respectively in California in 2014).[15-18] Commercial formulations for the 1,3-dichloropropene or chloropicrin rely on the liquid forms (Telone®) applied by shank injection or by drip irrigation.[19] However, the direct use of liquids requires high dosage, which causes substantial air and groundwater pollution due to the high volatility and mobility of the liquid chemicals, as well as significant safety hazards to workers during handling and transporting.[15-16, 20-21]

Sorption based formulations using porous solids to adsorb fumigants and then slow release them have emerged as an alternative to suppress the volatility of the chemicals as well as to reduce pollutions. Porous matrices such as activated carbon, activated clay, adsorption resin, and activated alumina have been proposed and shown prolonged effective lifetime of fumigants,[22-25] however, none of these carrier materials are naturally degradable, which greatly increases their environmental impact due to the accumulation after implementation.

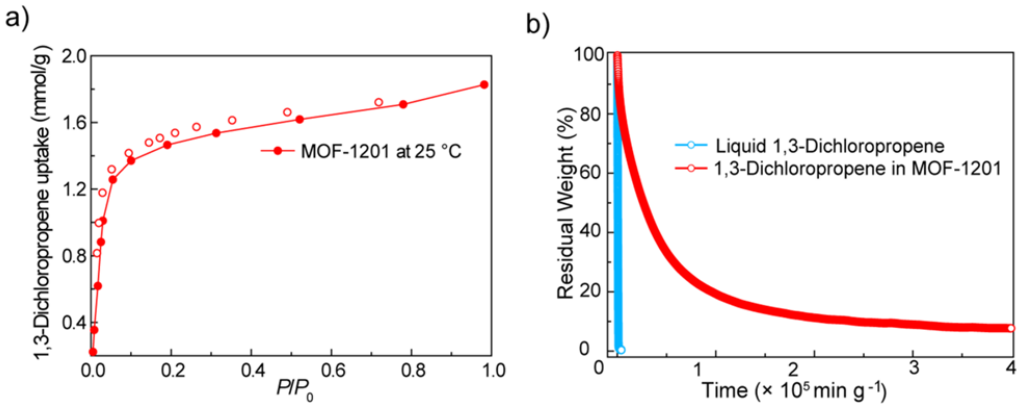

Figure 5.8 Sorption and slow release of fumigant by MOF-1201. (a) *cis*-1,3-dichloropropene vapor adsorption isotherm in MOF-1201 at 25 °C, solid and open circles represent the adsorption and desorption branches, respectively. (b) Slow release traces of pure liquid (blue) and MOF-1201 encapsulated *cis*-1,3-dichloropropene (red) at 25 °C. Reprinted with permission from ref 26. Copyright 2017 American Chemical Society

Sorption of the fumigant *cis*-1,3-dichloropropene by MOF-1201 was carried out here.[26] The adsorption isotherm was measured at 25 °C and is shown in Figure 3c, displaying a sharp uptake of 1.4 mmol g^{-1} (13 wt%) in the low partial pressure range (P/P_0 = 0.1), attributed to adsorption within the pores. This uptake was in the range of the values achieved in other porous materials (5–40 wt%) reported in patents.[24] Preliminary slow release performance was demonstrated by purging the sample of MOF-1201 loaded with *cis*-1,3-dichloropropene or liquid *cis*-1,3-dichloropropene in an air flow of 1.0 cm^3 min^{-1}. The sample weight was monitored by a thermogravimetric instrument. As shown in Figure 3d, liquid *cis*-1,3-dichloropropene released quickly, with 80% of the total weight evaporated within 1,000 min g^{-1}. In contrast, the *cis*-1,3-dichloropropene encapsulated in MOF-1201 released in a much slower manner, with 80% of the total (10.5 wt%) released in 100,000 min g^{-1}, corresponding to 100 times slower compared with liquid *cis*-1,3-dichloropropene under the same conditions.

The degradability of MOF-1201 was then tested. MOF-1201 can be disassembled in water to give its components: Ca^{2+} ions, lactate, and acetate. It is found that 1L water can dissolve 120 ±10 g of MOF-1201, and the saturated solution has a nearly neutral pH value (7.6). This property points to MOF-1201 as having the potential to overcome the accumulation issues, thus minimize adverse effects to the environment but leaving calcium as nutrient in the soil.[27]

5.4 Conclusions

The structural design of MOFs is not only synthetically interesting, but also allows for realization of the desire to create materials with enhanced or previously unattainable properties and fucntions. In this Chapter, It is demonstrated that the unique structural and functional character of a MOF can be useful for important environmental applications. Specifically, the use of large-pore, hydrophobic ZIF-412 for purifying air represents an important step toward the removal of large-sized VOCs. Additionally, the use of envrionmentallhy friendly porous Ca^{2+} lactate frameworks as degradable pesticide carriers

signifies an important step towards the use of MOFs in the agriculture and food industries. The applicability of these MOFs stemmed from their structures and compositions. Such work highlights the importance of structural design.

5.5 Acknowledgments

The work presented herein was funded by U.S. Department of Defense, Defense Threat Reduction Agency (DTRA) and BASF SE (Ludwigshafen, Germany).

5.6 References

[1] World Health Organisation (WHO), *7 million premature deaths annually linked to air pollution*, http://www.who.int/mediacentre/news/releases/2014/air-pollution/en/; accessed: March 2018.
[2] Barea, E.; Montoro, C.; Navarro, J. A. R. *Chem. Soc. Rev.* **2014**, *43*, 5419.
[3] Fracaroli, A. M.; Furukawa, H.; Suzuki, M.; Dodd, M.; Okajima, S.; Gándara, F.; Reimer, J. A.; Yaghi, O. M. *J. Am. Chem. Soc.* **2014**, *136*, 8863.
[4] Li, D.; Furukawa, H.; Deng, H.; Liu, C.; Yaghi, O. M. *Proc. Natl. Acad. Sci. U.S.A.* **2014**, *111*, 191.
[5] Datta, S. J.; Khumnoon, C.; Lee, Z. H.; Moon, W. K.; Docao, S.; Nguyen, T. H.; Hwang, I. C.; Moon, D.; Oleynikov, P.; Terasaki, O.; Yoon, K. B. *Science* **2015**, *350*, 302.
[6] Khan, F. I.; Ghoshal, A. K. *J. Loss Prev. Process Ind.* **2000**, *13*, 527–545.
[7] Britt, D.; Tranchemontagne, D.; Yaghi, O. M. *Proc. Natl. Acad. Sci. U.S.A.* **2008**, *105*, 11623–11627 (2008).
[8] Vellingiri, K.; Szulejko, J. E.; Kumar, P.; Kwon, E. E.; Kim, K.-H.; Deep, A.; Boukhvalov, D. W.; Brown, R. J. C. *Sci. Rep.* **2016**, *6*: 27813.
[9] DeCoste, J. B.; Peterson, G. W. *Chem. Rev.* **2014**, *114*, 5695–5727.
[10] Barea, E.; Montoro, C.; Navarro, J. A. R. *Chem. Soc. Rev.* **2014**, *43*, 5419–5430.
[11] Glover, T. G.; Peterson, G. W.; Schindler, B. J.; Britt, D.; Yaghi, O. M., *Chem. Eng. Sci.* **2011**, *66*, 163–170.
[12] Zhao, Z.; Li, X.; Li, Z. *Chem. Eng. J.* **2011**, *173*, 150–157.
[13] Moghadam, P. Z.; Fairen-Jimenez, D.; Snurr, R. Q. *J. Mater. Chem. A* **2016**, *4*, 529.
[14] Yang, J.; Zhang, Y.; Liu, Q.; Trickett, C. A.; Gutierrez-Puebla, E.; Monge, M. Á.; Cong, H.; Aldossary, A.; Deng, H.; Yaghi, O. M. *J. Am. Chem. Soc.* 2017, *139*, 6448.
[15] Shorter, J. H.; Kolb, C. E.; Crill, P. M.; Kerwin, R. A. *Nature* **2002**, *377*, 717.
[16] Martin, F. N. *Annu. Rev. Phytopathol.* **2003**, *41*, 325.
[17] Ashworth, D. J.; Yates, S. R.; Wesenbeeck, I. J. V.; Stanghellini, M. *J. Agric. Food Chem.* **2015**, *63*, 415.
[18] Pesticide Use reporting–2014 Summary Data, Sacramento, CA, USA, 2014; available at http://www.cdpr.ca.gov/docs/pur/pur14rep/14_pur.htm.
[19] Kim, J.-H.; Papiernik, S. K.; Farmer, W. J.; Gan, J.; Yates, S. R. *J. Environ. Qual.* **2003**, *32*, 2223.
[20] Yates, S. R.; Ashworth, D. J.; Zheng, W.; Zhang, Q.; Knuteson, J.; Wessenbeeck, I. J. V. *J. Agric. Food Chem.* **2015**, *63*, 5354.
[21] Desaeger, J. A. Eger, J. E. J.; Csinos, A. S.; Gilreath, J. P.; Olson, S. M.; Webster, T. M. *Pest Manag. Sci.* 2004, 60, 1220.
[22] Akira, S.; Mizuyoshi, F.; Hiroshi, A.; Shiyunnosuke, W.; Nobuji, T. Granular chloropicrin

preparation for soil disinfection and production thereof. Japan. Patent JPH01172302 (A), July 7, 1989.
[23] Solar, J. M.; Wilson, C. L.; Ghaouth, A. E. Controlled release fumigation of harvested agricultural commodities. US Patent US 5958490 A, Sep 28, 1999.
[24] Han, J. L. Mixed solid preparation of chloropicrin and 1.3-dichloropropylene and manufacturing technology thereof. China Patent CN 101627754 B, Nov 13, 2013.
[25] Han, J. L.; Yi, C. J. Preparation method and application of 1,3-dichloropropene solid slow-release preparation. China Pat. Appl. CN 201310062631, May 22, 2013.
[26] Yang, J.; Trickett, C. A.; Alahmadi, S. B.; Alshammari, A. S.; Yaghi, O. M. *J. Am. Chem. Soc.* **2017**, *139*, 8118.
[27] Engelstad, O.P. *Fertilizer Technology and Use*; Soil Science Society of America: Madison, 1985.

Chapter 6: Concluding Remarks and Future Outlook

6.1 Challenges and Opportunities

Reticular synthesis[1] addressed the long-standing challenge in designing and constructing new crystalline porous materials from molecular building blocks, yielding materials that have predetermined structures, chemical compostions, and properties. This concept has paved the way for a large family of MOF materials with great structural diversity and tunability.[2]

Although reticular synthesis is a powerful, robust principle, it is not easily applied to several special classes of MOFs that consist of single metal ions or flexible organic linkers. These include zeolitic imidazolate frameworks (ZIFs) and related tetrahedral MOFs, environmentally friendly MOFs made from alkali and alkaline earth metal ions, and naturally existing flexible linkers due to the lack of directional and rigid information. During my graduate studies, I focused on seeking new synthetic paths and general guiding principles for fabrication of these MOFs.

Such a task is highly worthy of investigation because these materials have unique structural and compositional characteristics. The development of precise structural design principles would allow for guided synthesis as a means of expansion of the family of materials, as well as application to previously unexplored fields.

With respect to tetrahedral structures, many realms await exploration. For example, we seek to understand what would happen if four or more distinct types of imidazolates are mixed and assembled into a ZIF simultaneously? Such assembly processes are quite complex, reminiscent of the self assembly processes of biomolecules.[3] The mechanism of ZIF self-assembly reactions remains largely unexplored. I feel that they will follow the general principle, but there could be new chemistry involved, for example, pertaining to the spatial arrangements of the imidazolate building blocks.

Considering the environmentally friendly MOFs constructed from naturally exisiting flexible linkers, the journey has also just begun. I only applied the mixed-linker approach in one simple system, but the potential for future exploration remains. For instance, how would the application of mixed peptides[4], proteins[5], or even DNA[6] affect the synthetic conditions and resultant structure(s)? The investigation of these materials could conclude with the ability to create large-pore, environmentally-friendly materials. I expect such research will deeply impact biological applications and reveal unique material properties such as adaptability.

The current design principles for ZIFs and environmentally-friendly MOFs are derived from experiments detailed in earlier chapters which are admittedly qualitative despite the introduction of the steric index (δ) in an attempt to ascribe quantitative evidence to them. As new and improved computational techniques for these systems are developed, it is highly likely the principles can be detailed in a quantitative way. If so, it will be possible to screen systems *in silico* by chosing suitable rings and their constituient imidazolate componenets to further improve the efficiency of the synthesis and designablity of the structures. The *in silico* screening can also be used to precisely adjust the composition of ZIFs for applications.[7]

6.2 Conclusions

This Chapter provides my humble thoughts regarding continuation of the field uncovered by my work. I believe there is much left to discover in order to understand the chemistry behind the synthesis of these materials. Only by digging deeper can we understand what governs the synthesis and properties of such materials. I envision a new regime in

which the scientific community has achieved its dream by rationally synthesizing materials.

6.3 References

[1] Yaghi, O. M.; O'Keeffe, M.; Ockwig, N. W.; Chae, H. K.; Eddaoudi, M.; Kim, J. *Nature* **2003**, *423*, 705.
[2] Furukawa, H.; Cordova, K. E.; O'Keeffe, M.; Yaghi, O. M. *Science* **2013**, *341*, 1230444.
3 King, N. P.; Bale, J. B.; Sheffler, W.; McNamara, D. E.; Gonen, S.; Gonen, T.; Yeates, T. O.; Baker, D. *Nature* **2014**, *510*, 103.
[4] Raone, J.; Yue, Y. –F.; Chong, S. Y.; Stylianou, K. C.; Bacsa, J.; Bradshaw, D.; Darling, G. R.; Berry, N. G.; Khimyak Y. Z.; Ganin, A. Y.; Wiper, P.; Claridge, J. B.; Rosseinsky, M. J. *Science* **2010**, *329*, 1053.
[5] Sontz, P. A.; Bailey, J. B.; Ahn, S.; Tezcan, F. A. *J. Am. Chem. Soc.* **2015**, *137*, 11598.
[6]. Rothemund, P. W. K. *Nature* **2006**, *440*, 297.
[7] Jiang, J. *Metal-Organic Frameworks Materials Modeling towards Engineering Applications*; Pan Stanford Publishing Pte Ltd., **2015**.